UNIVERSITY OF CALIFORNIA, SAN DIEGO

Antihydrogen Formation from Antiprotons in a Pure-Positron Plasma via Three-Body Recombination and Collisional and Radiative De-Excitation

A Dissertation submitted in partial satisfaction of the
Requirements for the degree of Doctor of Philosophy

in

Physics

by

Eric Matthew Bass

Committee in charge:

Professor Daniel H. E. Dubin, Chair
Professor Robert E. Continetti
Professor Thomas M. O'Neil
Professor Clifford M. Surko
Professor John C. Wheeler

2008

This Dissertation of Eric Matthew Bass is approved, and it is acceptable in quality and form for publication on microfilm:

_____

_____

_____

_____

_____

Chair

University of California, San Diego

2008

Dedication

For her unfailing support and love, this thesis is dedicated to Emily. Her smile is my joy and my inspiration.

Contents

List of Figures

List of Tables

Acknowledgements

Above all, I would like to acknowledge my committee chair and advisor, Professor Daniel H. E. Dubin, for his patience and support. This work benefits from his many insights and valuable input. Thanks to his measured guidance, I am a better scientist than I would otherwise be.

My gratitude also to Professors C. Fred Driscoll and Thomas M. O'Neil. Our discussions have helped expand my thinking on many matters, scientific and otherwise. Each has also demonstrated a high standard of scientific excellence to which I aspire.

I would also like to acknowledge Dr. François Anderegg, Dr. Andrey Kabantsev, Dr. Jonathan Yu, Dr. Terrance Hilsabeck, Dr. Nobu Shiga and my graduate student colleagues Michael Anderson, Daniel Creveling, Robert Lynch, and Jack Quinn for discussions and input. To the non-neutral plasma physics group secretary, Jo Ann Christina, goes my sincere thanks for helping to keep all the wheels turning.

To the rest of my thesis comittee — Clifford M. Surko, Robert E. Continetti, and John C. Wheeler — I extend my sincere appreciation for their time, forbearance, and valuable feedback.

Thanks also to my family and friends for their continuing support. My sincere appreciation goes to all of them. My gratitude goes especially to my wife, Emily, without whom I could never have come so far. Her support means more to me than anything.

Some material in Chapters 2–4 is in preparation for publication. The dissertation author is the primary investigator and author of this material.

This work was supported by National Science Foundation grants PHY-9876999 and PHY-0354979, and NSF/DOE grant PHY-0613740.

Vita, Publications, and Fields of Study

VITA

1997–1999	Teaching Assistant, Department of Mathematics University of Houston
2000	Bachelor of Science in Physics, University of Houston Bachelor of Science in Mathematics, University of Houston
2001–2004	Teaching Assistant, Department of Physics University of California, San Diego
2001	Master of Science in Physics, University of California, San Diego
2001–2007	Research Assistant, University of California, San Diego
2008	Doctor of Philosophy in Physics, University of California, San Diego

PUBLICATIONS

E.M. Bass and D.H.E. Dubin. "Simulation and theory for antihydrogen formation in pure-positron plasmas." (*in preparation*)

E.M. Bass and D.H.E. Dubin. "Relaxation of antihydrogen from Rydberg to ground state." *AIP Conference Proceedings* 862, 147152 (2006).

E.M. Bass and D.H.E. Dubin. "Energy loss rate for guiding-center antihydrogen atoms." *Physics of Plasmas* 11, 12401243 (2004).

E.M. Bass. A Computer Analysis of Cut and Conjugate Loci Using Numerical Approximations of Jacobi's Equation Executed in Maple V. *Honors thesis, University of Houston* (2000)

FIELDS OF STUDY

Major Field: Physics

Studies in Plasma Physics
Professors Vitali D. Shapiro, Patrick H. Diamond, and Ronald E. Waltz

Studies in Statistical Mechanics
Professor Daniel P. Arovas and Herbert Levine

Studies in Quantum Field Theory
Professor Elizabeth Jenkins

Studies in Quantum Mechanics
Professor Lu J. Sham

Studies in Electromagnetism
Professor Kenneth A. Intriligator

Studies in Classical Mechanics
Professor Aneesh V. Manohar

Studies in Applied Mathematics
Professor Raj K. Pathria

ABSTRACT OF THE DISSERTATION

Antihydrogen Formation from Antiprotons in a Pure-Positron Plasma via Three-Body Recombination and Collisional and Radiative De-Excitation

by

Eric Matthew Bass

Doctor of Philosophy in Physics

University of California, San Diego, 2008

Professor Daniel H. E. Dubin, Chair

Recombination of antiprotons with positrons (into neutral antihydrogen) in a strong magnetic field is investigated with classical models. A single antiproton in a pure-positron plasma is considered, given the very-low antiproton density in antihydrogen experiments. In these cryogenic experiments, three-body recombination dominates charge capture and produces highly-excited atoms with binding energy near the thermal level. Such atoms exist in a "guiding-center" state, characterized by $\vec{E} \times \vec{B}$ drift motion and adiabatically invariant cyclotron action in the positron orbit. De-excitation occurs by collisional and radiative relaxation. Radiation is small in guiding-center atoms. At deeper binding or low angular momentum, the orbit is chaotic and radiation becomes significant.

Collisional de-excitation is investigated with a classical Monte-Carlo code

and analytic theory. The code gives the probability $w(\epsilon, \epsilon')$ of an atom making a collisional transition from energy ϵ to energy ϵ'. The component from collisions with large impact parameters is confirmed with analytic theory using integrals over unperturbed trajectories. A direct calculation of the drag exerted by the plasma on the bound positron orbit confirms the energy-loss rate from such collisions. It peaks when the drift velocity equals the thermal velocity.

The transition rates from the Monte-Carlo simulation are used in a numerical solution of the master equation to calculate the rate of antihydrogen formation from a thermal plasma. Deep binding energies become populated as states trickle in from an invariant reservoir of thermal equilibrium atoms at shallow binding. A steady-state distribution forms at shallow binding, then propagates to deep binding over thousands of collision times. We estimate the number of atoms that collisionally de-excite to the chaotic regime for typical experimental parameters.

A classical estimate of the radiation rate is made by averaging the Larmour power over phase-space surfaces defined by fixing the two conserved atomic variables: azimuthal angular momentum p_ϕ and energy U. A small fraction of low-angular-momentum atoms will radiate rapidly to the ground state. We estimate the number of such atoms from the distributions calculated before.

Introduction

A sample of neutral antihydrogens atoms, each consisting of an antiproton nucleus surrounded by a positron, preferably in the ground state, would provide an opportunity to explore the nature of antimatter, particularly CPT invariance [1]. Spectroscopic diagnosis of atomic energy levels allows high-precision measurements of antiproton and positron charge and magnetic moment.

Unfortunately, matter-antimatter annihilation prevents conventional storage of antimatter, greatly complicating any attempt to accumulate it in any form. Positrons obtained from a radioactive sodium source are routinely stored in Penning-Malmberg traps [2]. However, to generate antihydrogen, antiprotons created in a particle accelerator must be exposed to positrons for long enough to recombine. This thesis outlines the recombination process, from the formation of highly-excited atoms by three-body recombination to the relaxation of these atoms to deep binding, using theory and simulation in the classical approximation. The analysis focuses on the experimentally relevant case where a strong magnetic field is present.

Current antihydrogen formation experiments use nested Penning traps to contain a strongly-magnetized, cryogenic positron plasma through which antipro-

tons can transit [3, 4] . Bound antiproton-positron pairs formed in these traps are typically far from the ground state, with binding energies near the thermal level [5, 6]. For a 15K plasma, this implies quantum numbers $n > 50$. These high-Rydberg atoms are characterized by slow $\vec{E} \times \vec{B}$ drift time scales, precluding radiation as an energy-loss mechanism until comparatively deep binding is achieved. Before this point, classical, atom-positron collisions dominate the equilibration process.

In the nested Penning traps of ATRAP and ATHENA [3, 4], a positron plasma is accumulated in an electrostatic well. Flanking the positron plasma on either side, along the magnetic field, inverted electrostatic wells hold antiprotons injected from CERN's Antiproton Decelerator. If these antiprotons have sufficient kinetic energy, they can transit through the well holding the positron cloud (a potential barrier for antiprotons) and possibly recombine to form antihydrogen. Once recombined, neutral antihydrogen is no longer confined axially or radially and can escape the trap. ATHENA detects antihydrogen formation by way of the annihilation signal as the atom collides with the trap wall.

Weakly bound atoms formed in this way may be re-ionized by the trapping fields. ATRAP detects antihydrogen formation by catching liberated antiprotons in another electrostatic well. By changing the ionizing electric field, ATRAP can diagnose the binding energy of formed antihydrogen [1]. When ionization by trapping fields occurs near the positron plasma, or if no recombination occurs, the free antiproton remains in the original electrostatic well. Thus, the same antiproton

can make multiple transits through the positron cloud. Each such transit gives another chance for the antiproton to bind tightly enough to a positron to form a stable antihydrogen atom. Throughout the analysis, we consider each antiproton transit individually.

Three-body collisions continuously form bound charge pairs and re-ionize them. Mansbach and Keck [7] identified a "kinetic bottleneck" at a few thermal energies kT. At binding energies more shallow than this level, atoms are more likely to be re-ionized than to cascade to deep binding through collisions with free particles. In the case of antihydrogen recombination, simulations predict a flux of atoms R_3 to energies deeper than the bottleneck [8, 9] given by:

$$R_3 \approx 0.07 n^2 \bar{v} b^5 \propto T^{-9/2}. \tag{1}$$

Above n is the positron plasma density, $\bar{v}$ is the thermal velocity, and $b = e^2/kT$ is the classical distance of closest approach in a positron-positron collision. The scaling of Eq. (1) with positron temperature T motivates the use of cryogenic temperatures for recombination experiments. Note that when the plasma is strongly correlated ($nb^3 > 1$), the predicted bottleneck flux is proportional to T^{-1} instead of $T^{-9/2}$ [10]. Antihydrogen experiments, however, are in the weakly-correlated regime and so are expected to obey the three-body scaling of Eq. (1). Because the atoms formed are charge neutral, they are no longer confined by Penning trap fields. Preliminary calculations suggested that almost all charge pairs exit the trap before collisional processes cause them to become deeply bound [11]. Here we af-

firm this result, but also find that a small part of the distribution does reach deep binding, even after a short time.

In Chapter 1, we describe the classical orbits of strongly-magentized, highly-excited antihydrogen atoms. The magnetic field means kinematic angular momentum $\vec{L}$ is no longer conserved in the atom. The canonical momentum p_ϕ conjugate to azimuthal coordinate ϕ is still conserved, however. Throughout the paper "angular momentum" refers to the conserved variable p_ϕ, not $\vec{L}$. We assume a stationary antiproton for simplicity. Orbits fall into one of three categories: guiding-center drift, chaotic, and Kepler [12]. Highly-excited atoms have primarily guiding-center drift orbits. These atoms are characterized by three well-separated orbital frequencies. In increasing order they are: $\vec{E} \times \vec{B}$ drift, parallel bounce, and cyclotron. At a threshold binding energy U_{chaotic} given by

$$U_{\text{chaotic}} = e^2 \left(\frac{B^2}{m_e c^2} \right)^{1/3},$$

the three characteristic frequencies converge. Above, e is the elementary charge, m_e is the positron (or electron) mass, B is the magnetic field strength, and c is the speed of light. Above and throughout the paper, Gaussian (cgs) units are used unless otherwise noted. At binding energies near U_{chaotic}, all degrees of freedom are coupled and orbits are non-integrable (chaotic). At much deeper binding the magnetic force is a weak perturbation on the intra-atomic electric force and orbits are approximately Keplerian [13]. In this simplified model, drifting-pair (a.k.a. giant-dipole) states do not exist.

We develop phase-space distributions for atoms of the first two types. Since cyclotron action is adiabatically invariant in guiding-center atoms, its phase space has effectively only four dimensions. In chaotic atoms, the phase space is six-dimensional. The reduced dimensionality of guiding-center phase space means that an ergodic distribution of guiding-center atoms fills real space in a qualitatively different way than its chaotic or Kepler counterpart. The transition to chaotic orbits has implications for collisional recombination, field ionization [14], and magnetic moment. We calculate the magnetic moment from the two distributions, and show that, as suggested in previous work [15], chaotic atoms are much more likely to be confined in a magnetic mirror than guiding-center atoms. A multipole mirror scheme has been proposed to confine neutral antihydrogen atoms [16].

The average collisional energy-loss (de-excitation) rate is calculated in Chapter 2 with two theories and a Monte-Carlo simulation. In the Monte-Carlo simulation, each shot simulates a collision between a free positron and an atom. The energy loss from large-impact-parameter collisions is determined with a diffusive model and a direct calculation of the drag induced by the wake in a collisionless plasma. The Monte-Carlo simulation shows results that agree well with both theories. In addition, the simulation gives the average energy-loss rate due to close collisions, which is theoretically intractable. The total energy-loss rate shows that, on average, most atoms are not exposed to the positron plasma for enough time to de-excite to the chaotic threshold energy U_{chaotic}, where radiation (explored in detail in Chapter 4) is significant for typical atoms.

The Monte-Carlo simulation described herein differs from the one performed by Mansbach and Keck [7]. We begin each shot with a fixed atomic binding energy ϵ. In Ref. [7], the initial atomic energy is chosen from a thermal distribution. Our method enables determination of the transition probability rate density $w(\epsilon, \epsilon')$ for transitions from atomic binding energy ϵ to energy ϵ'. The method of Mansbach and Keck is well suited for determining the one-way flux of atoms to deeper binding (given a thermal distribution). The relatively simple scaling derived in Ref. [7] applies only to this value. By contrast, the rates derived from the present simulation can be used to determine the evolution of an arbitrary distribution of atomic energies.

A numerical solution of the master equation using the transition probability rate density derived via simulation in Chapter 2 is used in Chapter 3 to calculate the distribution of antihydrogen binding energies produced from an antiproton transiting through a thermal, positron plasma as a function of transit time for three values of the plasma magnetization parameter

$$\chi \equiv \frac{r_c}{b},$$

where r_c is the cyclotron radius of a thermal positron. The fraction of antiproton transits yielding deeply bound antihydrogen is determined from these distributions. We compare the observed distributions to energy spectra and absolute antihydrogen production rates in the experiments in Chapter 3.

For estimated experimental parameters, including an optimistic transit time

of 10 μs, approximately one in 10^6—10^5 antiproton transits will yield an antihydrogen atom at or beyond the chaotic cutoff energy U_{chaotic} considering collisional de-excitation only. When radiation is considered, as in Chapter 4, the fraction is 10 to 100 times greater.

As previously predicted [17], the number of antihydrogen atoms below a fixed threshold binding energy is found to scale positively with temperature for short antiproton transit times and temperatures above a few Kelvin. The $T^{-9/2}$ scaling of Eq. (1) only appears for very long transit times, when a steady-state antihydrogen distribution is established. While a steady-state distribution, and thus flux dependent on $T^{-9/2}$, is established almost instantly above the kinetic bottleneck, at deeper binding finite time is required for downward flux to reach the steady-state value. This process has implications for experiments using the recombination rate to diagnose plasma temperature [18] or identify whether three-body recombination is the dominant recombination mechanism [19].

In the final chapter, we make a crude estimate of the radiation rate based on ergodic orbits. The full, three-dimensional ergodic distribution is used in anticipation of the fact that cyclotron action is not adiabatically invariant in those atoms where radiation is significant. While a quantum-mechanical three-body-recombination done by Hu [20] indicates that high-angular-momentum states may be preferentially populated, the ergodic distribution provides the simplest estimate of radiative relaxation. The estimate obtains the energy-loss rate due to radiation as a function of energy U and angular momentum p_ϕ by averaging the classical

Larmour power over ergodic surfaces of fixed U and p_ϕ. We find that radiation is suppressed below the chaotic energy U_{chaotic}, as seen in a previous quantum-mechanical calculation [21]. Even at energies smaller than U_{chaotic}, a small fraction of low-angular-momentum atoms will rapidly radiate to the ground state even in the guiding-center atom energy range, assuming an ergodic distribution of atomic states.

We lastly combine the collisional and radiative results to estimate what fraction of atoms will radiate to the ground state from the collisionally evolved distributions of Chapter 3. Inititally, when the distribution is composed only of guiding-center atoms, only atoms at very low angular momentum p_ϕ radiate to the ground state. Radiation to the ground state increases as collisions push atoms to deeper binding and repopulate low-angular-momentum states (Stark mixing). The combined estimate predicts one antiproton transit in 10^4 will yield a ground-state atom for a magnetic field of 6 T, a temperature of 4 K, a density of 10^8 cm^{-3}, and an antiproton transit time of 10 μs.

The present work all assumes that the distribution of atoms remains ergodic throughout the collisional evolution. Future work should consider the concurrent evolution of both energy and conserved angular momentum p_ϕ. This involves determining the transition probability rate density in these two dimensions instead of just in energy U. To obtain similar statistics, this would require simulating around $10,000$ times as many collisions as we did. Once the rates are determined, a solution of the master equation in two dimensions can track the continuous

evolution from the guiding-center to the chaotic distribution.

We have also neglected center-of-mass motion of the atom and antiproton mobility in this analysis. Atom motion can significantly affect the recombination rate [9] and internal atom dynamics [12]. If parallel motion is faster than the thermal velocity, the effective collision frequency changes and the energy-loss rate must similarly change.

Chapter 1

Guiding-Center and Chaotic Atoms

In this chapter, we describe the classical orbital trajectory of strongly-magnetized antihydrogen atoms. To simplify the analysis, the antiproton is assumed stationary and the atom is chosen to be at rest in the laboratory frame. The internal energy U thus contains only the positron component:

$$U = \frac{e^2}{r} - \frac{1}{2} m_e v^2. \tag{1.1}$$

Here we have introduced a minus sign so that a positive U indicates a bound state. The positron mass is m_e, r is the distance from the nucleus, and e is the elementary charge. Choosing the magnetic field to lie along the z direction and expressing the Hamiltonian for this system in cylindrical coordinates, we get

$$H = \frac{1}{2m_e}\left(p_z^2 + p_\rho^2 + \left(\frac{p_\phi}{\rho} - \frac{1}{2}\rho\Omega_c\right)^2\right) - \frac{e^2}{(\rho^2 + z^2)^{1/2}}.$$

The cylindrical radius ρ is the perpendicular distance from the positron to the field line on which the nucleus rests. Symmetry in ϕ implies that, in addition to the total energy U, the canonical angular momentum p_ϕ conjugate to the azimuthal

coordinate ϕ is conserved:

$$p_\phi \equiv m_e \rho^2 \left(\dot{\phi} + \frac{1}{2}\Omega_c \right). \tag{1.2}$$

The system lacks spherical symmetry, however, so the full angular momentum vector $\vec{L}$ is not conserved as it is in the unmagnetized system. While n remains a good quantum number, quantum number l is no longer well defined.

In the classical limit, orbits separate into three categories. They are, in order of increasing binding energy: guiding-center drift, chaotic, and Kepler. In a guiding-center atom, the positron $\vec{E} \times \vec{B}$ drifts around the stationary antiproton while undergoing cyclotron motion. Parallel to the magnetic field, the positron bounces back and forth, confined in the electrostatic well of the antiproton. Actions associated with each oscillation are adiabatically conserved. The cyclotron action I_c, proportional to the cyclotron magnetic moment, supplies an extra constant of the motion, making orbits integrable. If any characteristic oscillation approaches the cyclotron frequency Ω_c, cyclotron motion becomes coupled to the other degrees of freedom and integrability is lost. In such chaotic atoms, the only constants of motion are the internal energy and the canonical angular momentum p_ϕ. At sufficiently deep binding, the magnetic field may be treated as a weak perturbation on the inter-particle forces. Classically, this indicates a convergence on Kepler orbits. In the Kepler regime, the magnetic field causes the kinematic angular momentum vector $\vec{L}$ to precess about the magnetic field.

The classical approximation is justified for the highly-excited states common

in antihydrogen formation experiments. In a cryogenic, positron plasma like those typical of such experiments, atoms form by three-body recombination with binding energy near the thermal level. For a 15 K plasma, this corresponds to a binding energy of 1.3 meV, equivalent to a quantum n number of about 102. For a 1 T magnetic field, chaotic orbits are typical around a binding energy of 7.14 meV, an n number of 44. At such shallow binding, the classical picture offers a good approximation to quantum atom dynamics. At smaller n, where quantum effects become significant, classical orbits still offer a useful point of comparison.

The slow drift motion of guiding-center atoms precludes radiation as an important mechanism for relaxation to deep binding. Chaotic atoms, however, are more likely to exhibit close passes between the nucleus and the bound positron. In this orbit regime, radiation can be important. We will see also that chaotic atoms are also more likely to be confined by multipole traps — in development in antihydrogen experiments [16] — than are moderately bound guiding-center atoms.

1.1 Guiding-center drift atoms

Guiding-center drift atoms are characterized by three orbital time scales: cyclotron orbits at frequency Ω_c, bouncing parallel to the magnetic field at frequency ω_z, and $\vec{E} \times \vec{B}$ drift around the nucleus at frequency ω_ϕ. Fig. 1.1 shows a typical guiding-center drift atom trajectory. For small bounce amplitude motion,

the frequencies order as follows:

$$\Omega_c >> \omega_z >> \omega_\phi. \tag{1.3}$$

Each of the well separated frequencies accompanies an adiabatically conserved action I. Taking the cyclotron action I_c as conserved and the magnetic field strong enough that

$$v_{\vec{E}\times\vec{B}} << v_z,$$

we can omit perpendicular velocity from the internal energy. The drift motion is small enough to be neglected, and the cyclotron motion is bound up inside an adiabatic invariant. The internal energy and azimuthal angular momentum simplify to

$$U \approx \frac{e^2}{(\rho^2 + z^2)^{1/2}} - \frac{1}{2} m_e v_z^2 \tag{1.4}$$

and

$$p_\phi \approx \frac{1}{2} m_e \rho^2 \Omega_c. \tag{1.5}$$

The approximate expression Eqn. (1.5) indicates a one-to-one correspondence between cylindrical separation ρ and conserved angular momentum p_ϕ. For physical clarity, we shall use ρ as the defining parameter in this section with this understanding. The frequencies ω_z and ω_ϕ are functions of ρ as well as energy U. Note that, for fixed U, the parallel bounce motion grows in amplitude as ρ decreases. We obtain the bounce amplitude $z_{\max}$ by setting $v_z = 0$ in Eqn. (1.4).

$$z_{\max} = \sqrt{\left(\frac{e^2}{U}\right)^2 - \rho^2} \tag{1.6}$$

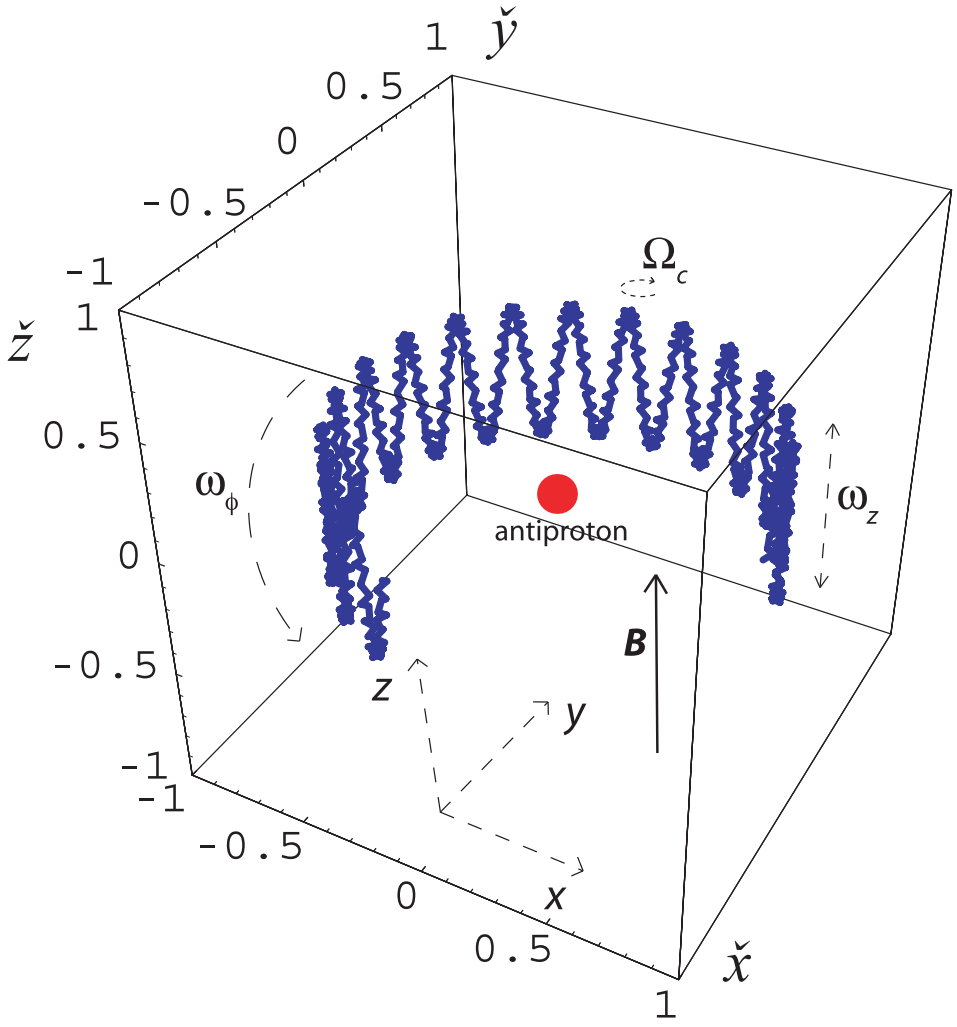

Figure 1.1: The orbital trajectory of a guiding-center atom. The positron $\vec{E} \times \vec{B}$ drifts about the antiproton and bounces along the z-axis. The antiproton is assumed stationary for simplicity. Also, perpendicular kinetic energy is neglected ($\vec{E} \times \vec{B}$ drift approximation). The axes shown are rescaled to make the atom radius one.

The cyclotron frequency $\Omega_c = (eB)/(m_e c)$ depends only on the magnetic field strength.

1.1.1 Orbit frequencies

Let us deduce expressions for ω_z and ω_ϕ as functions of U and ρ. From the theory of action angle variables [22]

$$\omega_\alpha = 2\pi \left| \frac{\partial U}{\partial I_\alpha} \right|.$$

The derivation proceeds more smoothly in rescaled units. We will avoid rescaling to atomic orbital parameters as they depend on the energy U. Instead, let us use collisional parameters in anticipation of the importance of collisions in atomic equilibration with the positron plasma at temperature T. Accordingly, we rescale by

$$\begin{aligned} b &= \tfrac{e^2}{kT} && \text{for length,} \\ \bar{v} &= \sqrt{\tfrac{kT}{m_e}} && \text{for velocity,} \\ \text{and} \quad & \tfrac{b}{\bar{v}} && \text{for time.} \end{aligned} \tag{1.7}$$

Above, b is the classical distance of closest approach and $\bar{v}$ is the thermal velcocity of the positron plasma. We will denote the dimensionless form of all variables rescaled as above with a hat ($\hat{}$). Let us also define a rescaled energy.

$$\epsilon \equiv \frac{U}{kT} \approx \frac{1}{(\hat{\rho}^2 + \hat{z}^2)^{1/2}} - \frac{1}{2}\hat{v}_z^2 \tag{1.8}$$

We characterize the degree of plasma magnetization in terms of the rescaled cyclotron frequency $\hat{\Omega}_c$ and define a small parameter χ as its inverse.

$$\chi \equiv \hat{\Omega}_c^{-1} = \frac{r_c}{b} \tag{1.9}$$

Now consider the bounce action.

$$\begin{aligned} I_z &= m_e \oint v_z dz \\ &= 4m_e \bar{v} b \int_0^{\hat{z}_{\max}} \sqrt{2\left(\frac{1}{(\hat{\rho}^2+\hat{z}^2)^{1/2}} - \epsilon\right)} d\hat{z}, \end{aligned} \tag{1.10}$$

The z-bounce frequency is given by

$$\omega_z = 2\pi \left| \frac{\partial U}{\partial I_z} \right|. \tag{1.11}$$

Taking the derivative of Eq. (1.10) with respect to I_z gives

$$\begin{aligned} 1 &= 4\sqrt{2} m_e \bar{v} b \Bigg(\frac{\partial \hat{z}_{\max}}{\partial I_z} \sqrt{\frac{1}{(\hat{\rho}^2 + \hat{z}_{\max}^2)^{1/2}} - \epsilon} \\ &\quad + \int_0^{\hat{z}_{\max}} \frac{1}{2} \left(\frac{1}{(\hat{\rho}^2 + \hat{z}^2)^{1/2}} - \epsilon \right)^{-1/2} \left(-\frac{\partial \epsilon}{\partial I_z} \right) d\hat{z} \Bigg). \end{aligned} \tag{1.12}$$

The turning point $\hat{z}_{\max}$, from Eqn. (1.4), is given in normalized variables by

$$\hat{z}_{\max} = \sqrt{\frac{1}{\epsilon^2} - \hat{\rho}^2}.$$

Substituting in, we see that the first term vanishes. Solving for $\partial\epsilon/\partial I_z$ and using Eq. (1.11) gives

$$\hat{\omega}_z = \frac{\pi}{\sqrt{2}} \epsilon^{3/2} \left[\int_0^{\sqrt{1-\check{\rho}^2}} \left(\frac{1}{(\check{\rho}^2 + \check{z}^2)^{1/2}} - 1 \right)^{-1/2} d\check{z} \right]^{-1}. \tag{1.13}$$

Here we made the substitutions $\check{z} = \epsilon \hat{z}$ and $\check{\rho} = \epsilon \hat{\rho}$. For small bounce amplitude ($\check{\rho} \approx 1$), the parallel oscillations are harmonic and Eq. (1.13) simplifies to:

$$\hat{\omega}_z \approx \epsilon^{3/2} \quad \text{for} \quad \check{\rho} \approx 1. \tag{1.14}$$

We follow a similar procedure to obtain the drift frequency ω_ϕ:

$$\omega_\phi = 2\pi \left| \frac{\partial U}{\partial I_\phi} \right| = \left| \frac{\partial U}{\partial p_\phi} \right|.$$

Then

$$\hat{\omega}_\phi = \chi \frac{1}{\hat{\rho}} \left| \frac{\partial \epsilon}{\partial \hat{\rho}} \right|_{I_z}. \tag{1.15}$$

To find $\partial\epsilon/\partial\hat{\rho}|_{I_z}$, we take the derivative of Eq. (1.10) with respect to $\hat{\rho}$, considering I_z as fixed.

$$\begin{aligned} 0 \;=\; 2\sqrt{2} m_e \bar{v} b \Bigg(& \frac{\partial \hat{z}_{\max}}{\partial \hat{\rho}} \sqrt{\frac{1}{(\hat{\rho}^2 + \hat{z}_{\max}^2)^{1/2}} - \epsilon} + \int_0^{\hat{z}_{\max}} \frac{1}{2} \left(\frac{1}{(\hat{\rho}^2 + \hat{z}^2)^{1/2}} - \epsilon \right)^{-1/2} \\ & \times \quad \left[-(\hat{\rho}^2 + \hat{z}^2)^{-3/2} \hat{\rho} - \frac{\partial \epsilon}{\partial \hat{\rho}} \right] d\hat{z} \quad \Bigg). \end{aligned}$$

Once again the first term vanishes. Isolating $\partial\epsilon/\partial\hat{\rho}$ from the remaining terms and substituting into Eq. (1.15) leads to

$$\hat{\omega}_\phi = \chi \epsilon^3 \frac{\int_0^{\sqrt{1-\check{\rho}^2}} (\check{\rho}^2 + \check{z}^2)^{-5/4} \left[1 - (\check{\rho}^2 + \check{z}^2)^{1/2} \right]^{-1/2} d\check{z}}{\int_0^{\sqrt{1-\check{\rho}^2}} (\check{\rho}^2 + \check{z}^2)^{1/4} \left[1 - (\check{\rho}^2 + \check{z}^2)^{1/2} \right]^{-1/2} d\check{z}}. \tag{1.16}$$

When bounce motion is small, the drift frequency reduces to

$$\hat{\omega}_\phi \approx \chi \epsilon^3 \quad \text{for} \quad \check{\rho} \approx 1. \tag{1.17}$$

Fig. 1.2 shows the rescaled drift, bounce, and cyclotron frequencies as a function of $\check{\rho}$ for atoms at two different binding energies. As binding energy increases, the range of ρ over which the frequency scaling of Eq. (1.3) holds true diminishes. The small-bounce, large-ρ forms of $\hat{\omega}_z$ and $\hat{\omega}_\phi$ in Eq. (1.14) and Eq. (1.17) converge at energy ϵ_c given by

$$\epsilon_c = \chi^{-2/3}. \tag{1.18}$$

At this energy, both the drift frequency and bounce frequency also converge on the cyclotron frequency.

$$\hat{\omega}_\phi = \hat{\omega}_z = \hat{\Omega}_c = \chi^{-1} \quad \text{at} \quad \epsilon = \epsilon_c$$

We call ϵ_c the chaotic cutoff energy. At binding energies deeper than ϵ_c, no atoms exhibit frequency separation and the bounce and cyclotron actions are no longer adiabatically invariant. The angular momentum p_ϕ and energy U become the only constants of the motion. These atoms exhibit chaotic orbits and are discussed in detail in the next section.

1.1.2 Guiding-center phase space distributions

Recall that the frequency ordering of Eq. (1.3) allows us to neglect perpendicular kinetic energy. Most of this energy is bound up in the cyclotron action, which is adiabatically invariant. In systems of interest, this action contains kinetic energy equal approximately to the thermal energy. As the atom cascades to deeper binding, the cyclotron action remains unmodified. We therefore anticipate a physical distribution of guiding-center atoms at binding energy U that is ergodically distributed in all degrees of freedom except those associated with perpendicular kinetic energy, and confine our phase space to the surface defined by $\vec{v}_\perp = 0$. This constraint is built into Eq. (1.4), so the appropriate distribution in phase space is given by

$$P(\check{r}, \check{v}_z) = \frac{\check{r}^2 \delta\Big(1 - \frac{1}{\check{r}} + \frac{1}{2}\check{v}_z^2\Big)}{\int \delta\Big(1 - \frac{1}{\check{r}} + \frac{1}{2}\check{v}_z^2\Big)\, \check{r}^2 d\check{r} d\check{v}_z}. \tag{1.19}$$

Above we have adopted dimensionless variables $\check{\alpha}$ rescaled by orbital, not collisional, parameters. The dimensionless form is denoted by a check ($\check{}$) and rescaled

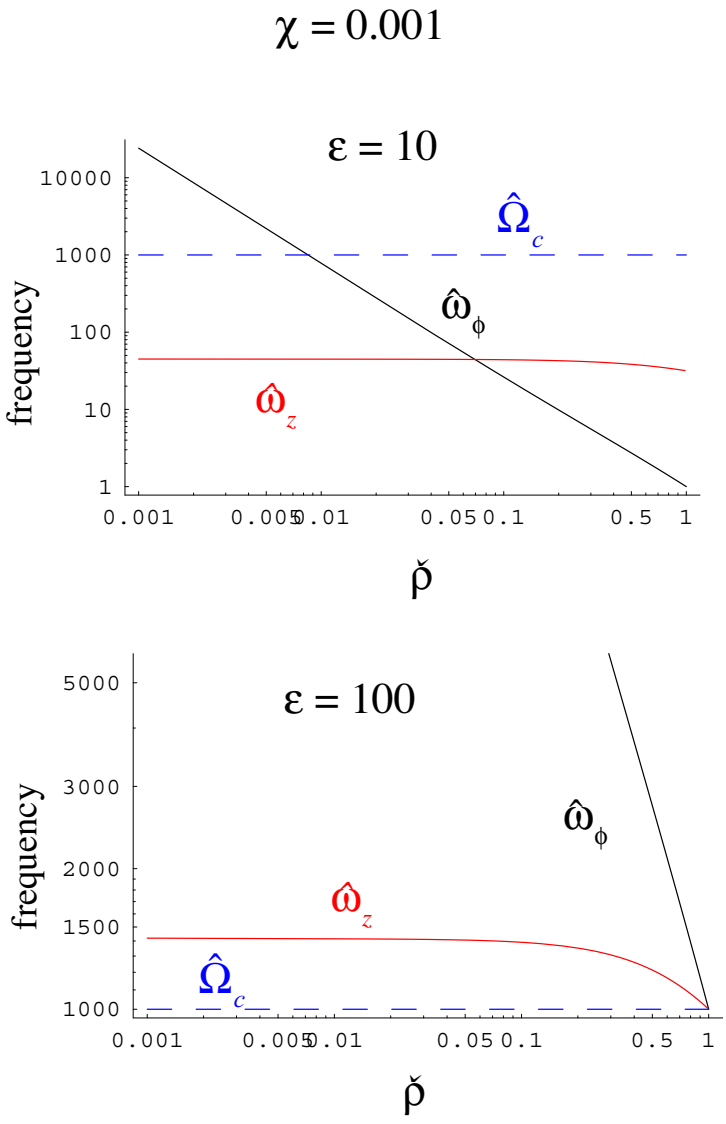

Figure 1.2: The three orbital frequencies in a guiding-center atom as a function of $\check{\rho} = \epsilon\hat{\rho}$, which always ranges between 0 and 1. The magnetization parameter $\chi = 0.001$. The energies are (a) $\epsilon = 10$ and (b) the chaotic cutoff energy $\epsilon_c = 100$. In (b), the guiding-center atom frequency ordering of Eq. (1.3) is broken at all $\check{\rho}$. Only a small fraction of possible atoms break the frequency ordering in (a).

by:

$$\begin{array}{rcll} r_{\rm atm} & = & \frac{e^2}{U} & \text{for length,} \\ v_{\rm atm} & = & \sqrt{\frac{U}{m_e}} & \text{for velocity,} \\ & & \frac{e^2 m_e^{1/2}}{U^{3/2}} & \text{for time,} \\ \text{and} & & m_e r_{\rm atm} v_{\rm atm} & \text{for angular momentum.} \end{array} \tag{1.20}$$

Spherical coordinates in Eq. (1.19) are utilized to take advantage of spherical symmetry in the electrostatic potential. The probabilities $P_r(\check{r})$ and $P_{v_z}(\check{v}_z)$ of finding the positron with radius $\check{r}$ and parallel velocity $\check{v}_z$ in the guiding-center limit are obtained by integrating Eq. (1.19).

$$P_r(\check{r}) = \int P(\check{r}, \check{v}_z)\, d\check{v}_z = \frac{16}{5\pi} \frac{\check{r}^{5/2}}{\sqrt{1-\check{r}}} \tag{1.21}$$

$$P_{v_z}(\check{v}_z) = \int P(\check{r}, \check{v}_z)\, d\check{r} = \frac{128\sqrt{2}}{5\pi} \left(2 + \check{v}_z^2\right)^{-4} \tag{1.22}$$

Note that $\check{r}$ ranges between 0 and 1, while $\check{v}_z$ can take any value. Fig. 1.3 compares the distributions $P_r(\check{r})$ and $P_{v_z}(\check{v}_z)$ for guiding-center atoms with the same distributions for chaotic atoms (derived in the next section). Exclusion of the perpendicular degrees of freedom from the ergodic distribution qualitatively affects the time-averged atom shape as reflected in these probabilities.

The ergodic probability distribution $P_{p_\phi}(\check{p}_\phi)$ in p_ϕ is given by a similar procedure. We again revert to cylindrical coordinates. First, we see from Eq. (1.5) that

$$P_{p_\phi}(\check{p}_\phi) = \frac{1}{\check{\Omega}_c \check{\rho}} P_\rho(\check{\rho}) \Big|_{\check{\rho}=\sqrt{\frac{2\check{p}_\phi}{\check{\Omega}_c}}}. \tag{1.23}$$

Then the ergodic distribution of angular momenta p_ϕ predicted for the guiding-

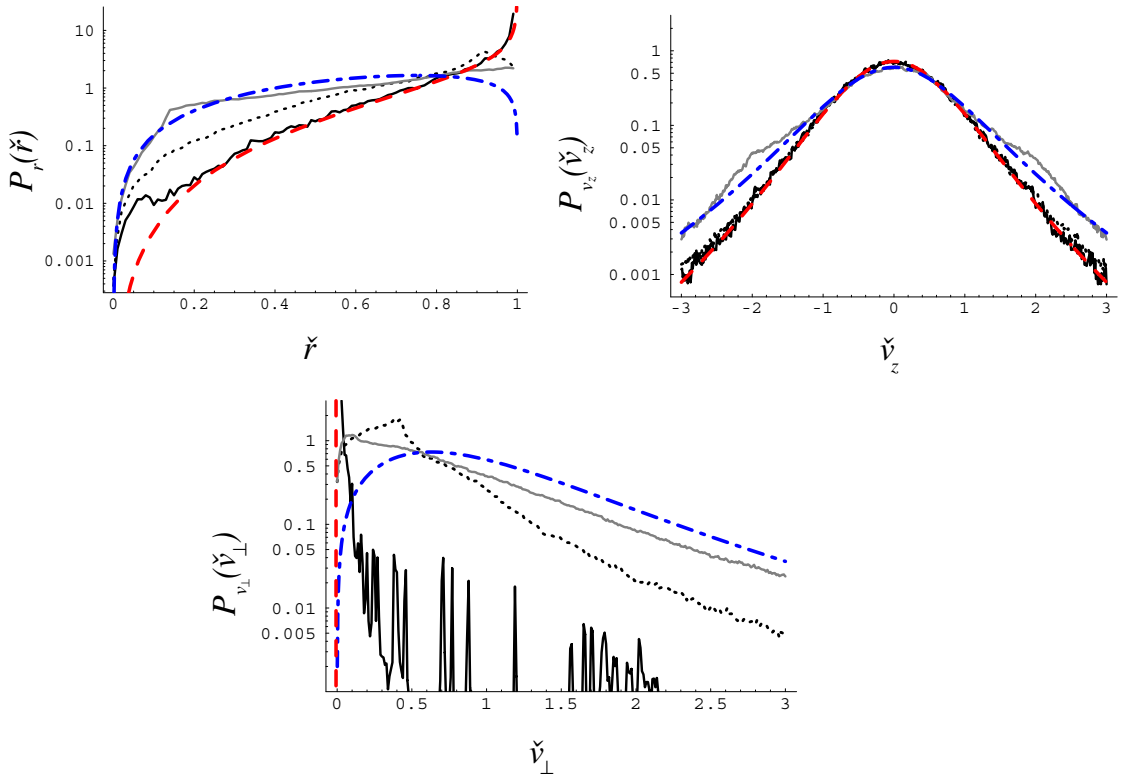

Figure 1.3: The time-averaged probability density (a) P_r in the spherical radius r, (b) P_{v_z} in the velocity parallel to the magnetic field, and (c) $P_{v_\perp}$ in the magnitude of the perpendicular velocity. The plots all have $\chi = 0.001$, making the chaotic cutoff $\epsilon_c = 100$. The binding energies $\epsilon = 4, 35$, and 100 are the solid-black, dotted-black, and solid-gray curves respectively. The probability density is averaged over two Kepler periods and an ensemble of 500 atoms whose initial conditions are chosen from the guiding-center ($\vec{v}_\perp = 0$) phase-space distribution (red, dashed curves). Full dynamics (including cyclotron motion) are used. As binding energy ϵ increases, the atom orbits naturally tend toward the fully-stochastic distribution (blue, dot-dashed curves).

center Hamiltonian ($\vec{v}_\perp = 0$) is

$$\begin{aligned} P_{p_\phi}(\check{p}_\phi) &= \frac{1}{\check{\rho}} \frac{\int \delta\left(1 - \frac{1}{(\check{\rho}^2+\check{z}^2)^{1/2}} + \frac{1}{2}\check{v}_z^2\right) \check{\rho} d\check{v}_z d\check{z}}{\int \delta\left(1 - \frac{1}{(\check{\rho}^2+\check{z}^2)^{1/2}} + \frac{1}{2}\check{v}_z^2\right) \check{\rho} d\check{\rho} d\check{v}_z d\check{z}}\Bigg|_{\check{\rho}=\sqrt{\frac{2\check{p}_\phi}{\check{\Omega}_c}}} \\ &= \frac{16}{5\pi\check{\Omega}_c} \int_0^{\check{z}_{\max}} \frac{(2\check{p}_\phi/\check{\Omega}_c + \check{z}^2)^{1/4}}{\sqrt{1-(2\check{p}_\phi/\check{\Omega}_c + \check{z}^2)^{1/2}}} d\check{z}. \end{aligned} \tag{1.24}$$

In the guiding-center approximation, angular momentum $\check{p}_\phi$ runs between 0 and $\check{\Omega}_c/2$. In the next section we will see that, when perpendicular kinetics are included, the range of possible angular momenta shifts to include negative values. Fig. 1.4 shows the ergodic distributions in $\check{p}_\phi$ appropriate for both the guiding-center and full Hamiltonians.

1.1.3 Guiding-center magnetic moment

The ergodic distributions of Eqs. (1.21), (1.22), and (1.24) will be used in the next chapter to choose initial conditions in a Monte-Carlo simulation. Another use is in predicting the distribution of magnetic moments μ in guiding-center atoms. In particular, atoms with moments oriented parallel to the background magnetic field ($\mu > 0$) are high-field seekers and are not confined in multipole trap configurations. Using the ergodic distributions above, we can predict what fraction of atoms have negative magnetic moments and are thus confined by the multipole.

The cyclotron component of the magnetic moment is oriented anti-parallel to the background magnetic field, favoring confinement. We assume this motion contains roughly the thermal energy.

$$\mu_c \approx -\pi \left(\frac{\bar{v}}{\Omega_c}\right)^2 e\Omega_c = -\pi \frac{\bar{v}^2}{\Omega_c} e$$

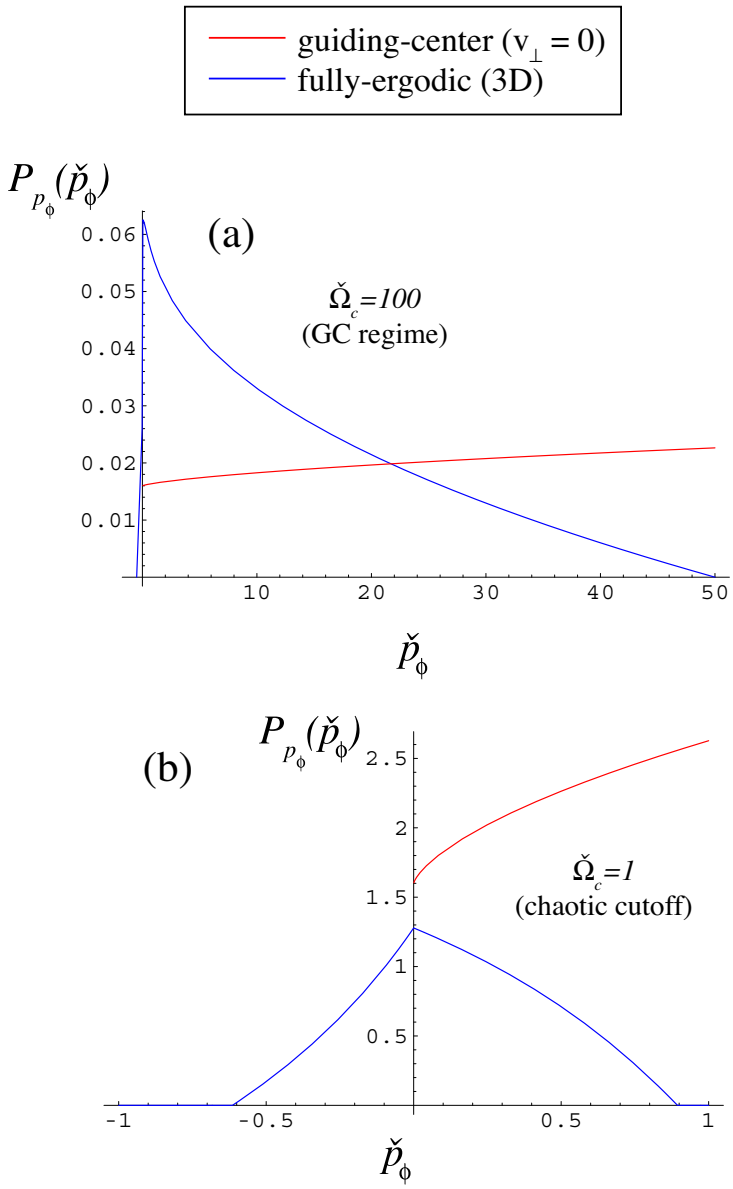

Figure 1.4: Ergodic distributions in angular momentum p_ϕ for the guiding-center ($\vec{v}_\perp = 0$) Hamiltonian (red curves) and the full Hamiltonian (blue curves). In (a), binding energy is in the guiding-center atom regime ($\check{\Omega}_c = 100$ or $\epsilon = 0.046\epsilon_c$). In (b) it is at the chaotic cutoff energy ($\check{\Omega}_c = 1$, $\epsilon = \epsilon_c$). The guiding-center distribution is most physical in (a), while the fully ergodic one is most physical in (b).

The atomic magnetron magnetic moment produced by the bound positron's $\vec{E}\times\vec{B}$ drift orbit is oriented parallel to the magnetic field and thus opposes confinement. Its magnitude varies with binding energy and perpendicular separation ρ (or angular momentum p_ϕ).

$$\mu_{\vec{E}\times\vec{B}} \approx \pi b^2 \hat{\rho}^2 e \frac{\bar{v}}{b}\hat{\omega}_\phi$$

Recall that the rescaled drift frequency took the form

$$\hat{\omega}_\phi = \chi\epsilon^3\mathcal{Q}(\check{\rho}) = \frac{\bar{v}}{b\Omega_c}\epsilon^3\mathcal{Q}(\check{\rho})\,,$$

with $\mathcal{Q}(\check{\rho})$ depending only on the internal parameter $\check{\rho}$, which always ranges between 0 and 1, regardless of binding energy. In terms of this parameter, the confinement condition

$$\mu = \mu_c + \mu_{\vec{E}\times\vec{B}} < 0$$

reduces to

$$\epsilon\check{\rho}^2\mathcal{Q}(\check{\rho}) - 1 < 0. \tag{1.25}$$

Note that the condition is independent of magnetic field, but depends on temperature through the rescaled energy ϵ. The fraction of confined guiding-center atoms is the integral of $P_{\check{\rho}}(\check{\rho})$ up to the maximum confined cylindrical radius $\check{\rho}_{\max}$ given by Eq. (1.25). Fig. 1.5 shows this predicted fraction for a range of ϵ. At moderate binding the confined fraction is quite small. We will see in the next section that the prospects for confinement are less bleak once cyclotron motion becomes coupled to the other orbital degrees of freedom and the atomic distribution becomes fully ergodic.

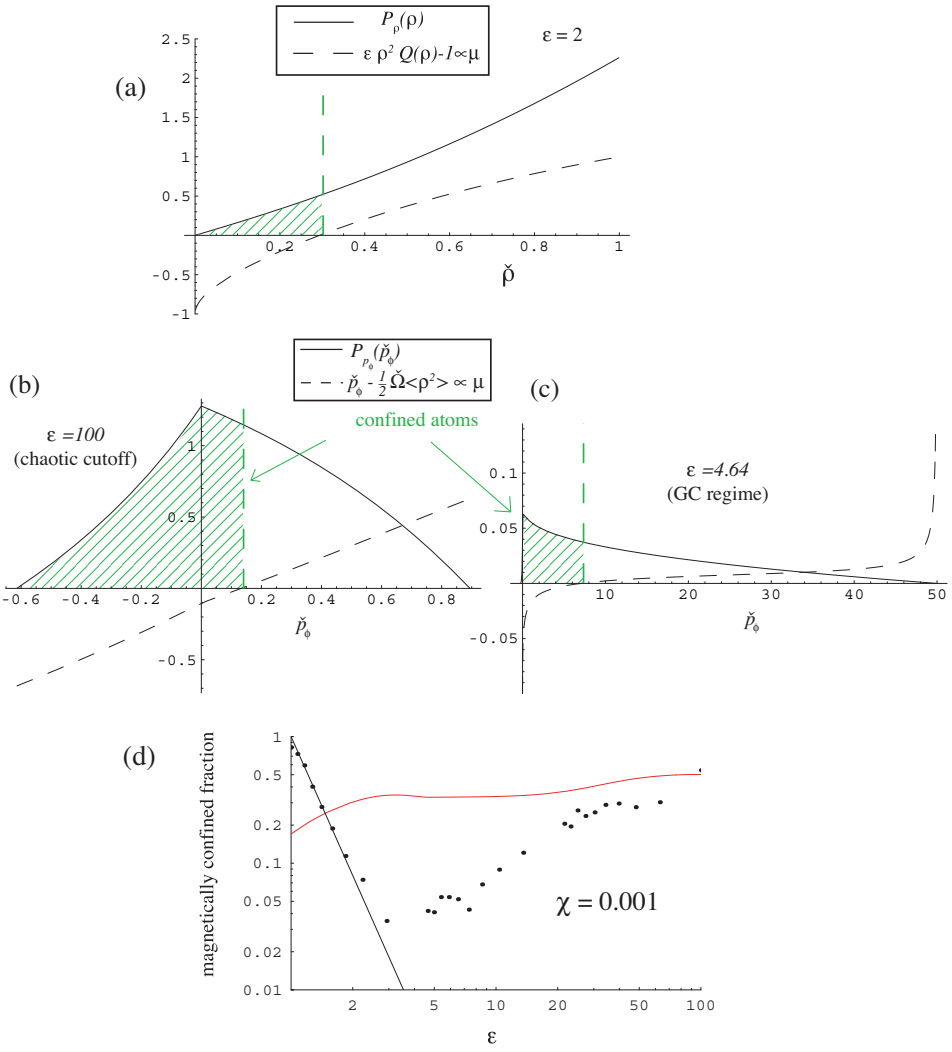

Figure 1.5: The predicted fraction of atoms with a magnetic moment favoring confinement by a multipole trap ($\mu < 0$) for $\chi = 0.001$. In guiding-center atoms, the fraction is the integral of the probability $P_\rho(\check{\rho})$ up to the maximum radius at which the confinement condition Eq. (1.25) holds true, illustrated in (a) for $\epsilon = 2$. The confined fraction is also determined directly from the fully-ergodic distribution, illustrated in (b) ($\epsilon = 100$, the chaotic cutoff) and (c) ($\epsilon = 4.64$, the guiding-center regime). It is shown as a function of ϵ (on a log-log scale) in (d) for guiding-center (black) and chaotic (red) atoms. The dots show the confined fraction of 1000 simulated atoms distributed ergodically in guiding-center phase space with cyclotron action at the thermal level. As binding energy increases, atoms switch to the chaotic distribution and confinement improves.

1.2 Chaotic Atoms

The frequency ordering of Eq. (1.3) fails for atomic states with sufficiently low angular momentum p_ϕ. As discussed in the previous section, at binding energies ϵ greater than the chaotic cutoff energy $\epsilon_c = \chi^{-2/3}$, the ordering is broken for all possible angular momenta. In orbital units, the chaotic cutoff condition takes the simple form

$$\check{\Omega}_c = 1.$$

When $\check{\Omega}_c >> 1$ ($\epsilon << \epsilon_c$), the cyclotron frequency far exceeds the orbit frequency and the atom is in the guiding-center drift regime. When $\check{\Omega}_c << 1$ ($\epsilon >> \epsilon_c$), the inverse is true and the atom is in the perturbed Kepler regime. Near the chaotic cutoff energy, the cyclotron frequency Ω_c, bounce frequency ω_z, and $\vec{E} \times \vec{B}$ drift frequency ω_ϕ are not well separated. Actions associated with cyclotron and bounce motion thus no longer exhibit adiabatic invariance. Then only two constants of the motion exist: energy U and azimuthal angular momentum p_ϕ. Atom orbits in the range of binding energy and angular momentum where these three frequencies are near each other are chaotic, and we call them chaotic atoms.

Two examples of chaotic atoms are shown in Fig. 1.6. One shows an atom with $\epsilon \gtrsim \epsilon_c$; the other shows a low-angular momentum state with $\epsilon < \epsilon_c$. As seen in Fig. 1.2, small-$\check{\rho}$ (i.e. small-angular-momentum) atoms can break guiding-center atom frequency ordering even at energies lower than the chaotic cutoff. Indeed, the cyclotron adiabatic invariant can even be broken when the other two frequencies

ω_z and ω_ϕ are well below the cyclotron frequency in the average sense.

When bounce amplitude is small (i.e. $\breve{\rho} \approx 1$), the electrostatic well parallel to the magnetic field is approximately parabolic and oscillations in this direction are harmonic. However, for small-$\breve{\rho}$ atoms the parallel oscillations have large amplitude, on the order of the atom size. While the bounce period T_z is given by

$$T_z = \frac{2\pi}{\omega_z},$$

the characteristic frequency appears much larger than ω_z when the positron passes close to the atomic nucleus. The positron velocity as it passes the origin $v_{z\max}$ is given by Eq. (1.8). In the limit of small ρ, and in collisional units:

$$\hat{v}_{z\max} = \sqrt{\frac{2}{\hat{\rho}}}.$$

The effective collision frequency $\hat{\omega}_{\text{eff}}$ for this close pass to the origin is:

$$\hat{\omega}_{\text{eff}} = \frac{\hat{v}_{z\max}}{\sqrt{2}\hat{\rho}} = \frac{1}{\hat{\rho}^{3/2}}.$$

The factor of $\sqrt{2}$ is introduced so that $\hat{\omega}_{\text{eff}}$ matches onto the small bounce form of $\hat{\omega}_z$ from Eq. (1.14). If the effective frequency exceeds the cyclotron frequency $\hat{\Omega}_c$, the adiabatic invariant I_c is broken and the atom becomes chaotic. The condition for chaotic orbits is:

$$\hat{\omega}_{\text{eff}} \gtrsim \hat{\Omega}_c = \chi^{-1}. \tag{1.26}$$

Regardless of binding energy, an atom will exhibit chaotic orbits if the perpendicular separation $\hat{\rho}$ is below a fixed value $\hat{\rho}_{\text{chaotic}}$ given by:

$$\hat{\rho}_{\text{chaotic}} \equiv \chi^{2/3}. \tag{1.27}$$

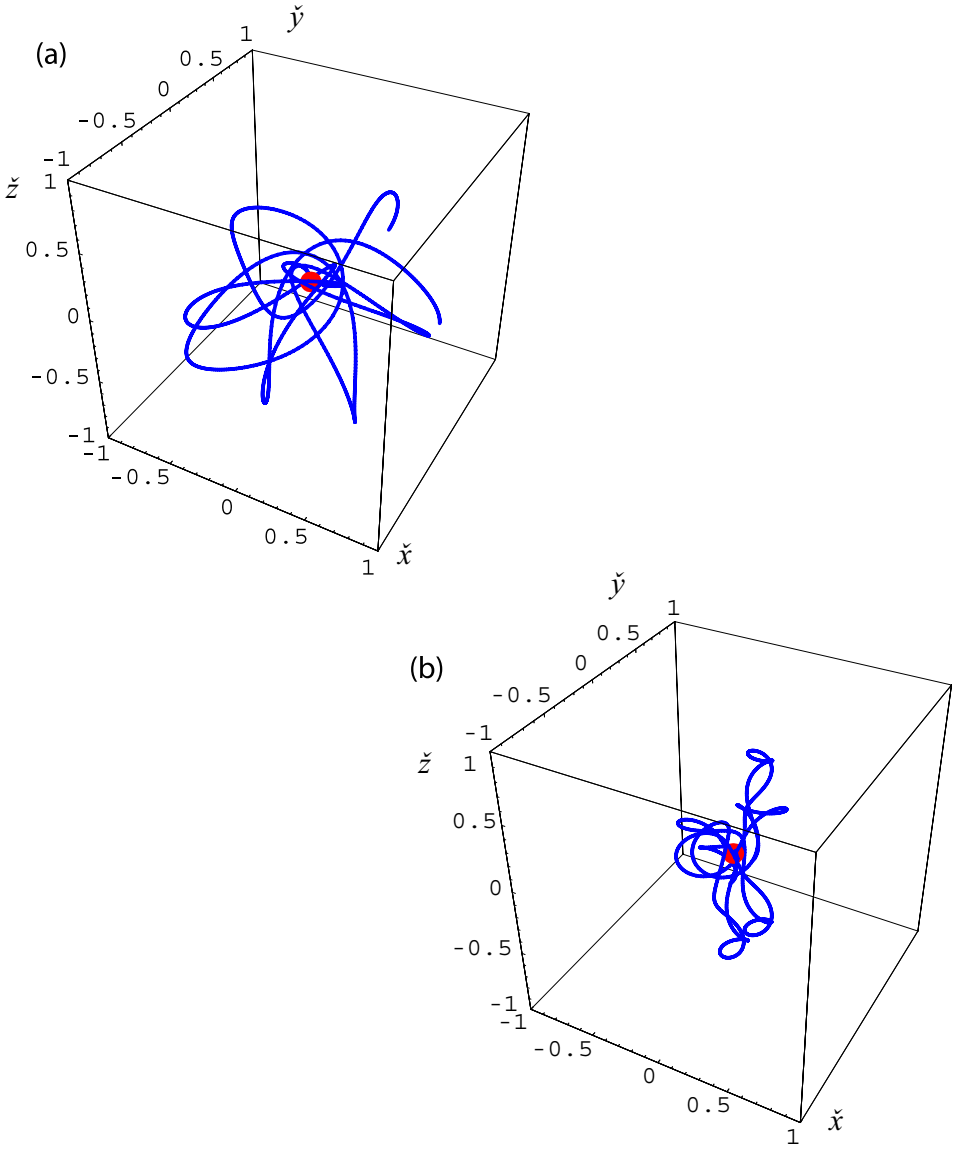

Figure 1.6: Two chaotic atoms. The atom in (a) is typical of one near the chaotic cutoff binding energy $\epsilon_c = \chi^{-2/3}$. In (b), the atom is at more shallow binding, but has a low value of angular momentum p_ϕ, equivalent to a small cylindrical separation ρ. The maximum ρ at which atoms become chaotic, and thus the fraction of such atoms in an ergodic distribution, increases with binding energy. At $\epsilon = \epsilon_c$, all atoms are chaotic.

In atomic (check) variables:

$$\check{\rho}_{\text{chaotic}} = \epsilon \hat{\rho}_{\text{chaotic}}.$$

We obtain the fraction of atoms exhibiting chaotic behavior at energy ϵ by integrating the guiding-center distribution in $\check{\rho}$ (related to P_{p_ϕ} by Eq. (1.23)) up to this point.

$$\text{chaotic fraction} = \int_0^{\check{\rho}_{\text{chaotic}}} P_\rho(\check{\rho})\, d\check{\rho} \tag{1.28}$$

Fig. 1.7 shows this fraction as a function of binding energy.

Below the chaotic binding energy $\epsilon_c = \chi^{-2/3}$, chaotic atoms look like the one in Fig. 1.6(b). These chaotic, Rydberg atoms are sometimes known as helical atoms due to the roughly helical orbit shape. Such high-n, low-angular-mometum states are common in laser excitation experiments [23, 24].

At binding energies deeper than the chaotic cutoff energy ϵ_c, all atoms are chaotic until binding becomes deep enough that the magnetic field force is weak compared to the inter-particle electric force. At successively deeper binding, chaotic orbits like the one in Fig. 1.6(a) gradually give way to perturbed Kepler orbits.

The breaking of the cyclotron adiabatic invariant is demonstrated by the dots in Fig. 1.7. At each energy ϵ, 1000 atoms were prepared with initial conditions chosen from the guiding-center distribution. The orbits, using the full, three-dimensional equations of motion, were followed for a few bounce periods. The cyclotron action, proportional to the positron's perpendicular kinetic energy in

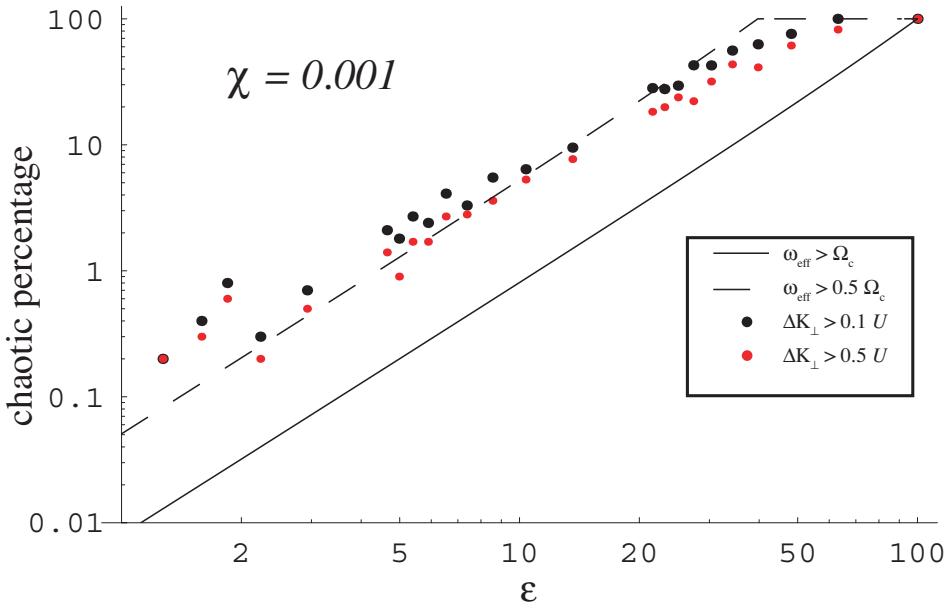

Figure 1.7: The fraction of atoms exhibiting chaotic behavior. When the effective bounce frequency $\hat{\omega}_{\text{eff}}$ exceeds the cyclotron frequency $\hat{\Omega}_c$, cyclotron action I_c is no longer adiabatically invariant and all degrees of freedom become coupled. The solid curve shows the fraction of an ergodic distribution (distributed in guiding-center phase space) of atoms that meet this criterion as a function of ϵ for $\chi = 0.001$. The dashed curve shows the fraction where $\hat{\omega}_{\text{eff}} > (1/2)\hat{\Omega}_c$. The dots show the percentage of 1000 simulated atoms where cyclotron action grew to one-tenth (black) or one-half (red) the binding energy U, indicating a breaking of the adiabatic invariant and chaos.

the instantaneous $\vec{E} \times \vec{B}$ drift frame, was tracked.

$$I_c \propto K_\perp|_{\text{drift frame}} = m_e \left(\left(v_x - \frac{c}{B} \frac{e^2 y}{(x^2 + y2 + z^2)^{3/2}} \right)^2 + \left(v_y - \frac{c}{B} \frac{e^2 x}{(x^2 + y2 + z^2)^{3/2}} \right)^2 \right)$$

If the fluctuations in $\Delta K_\perp$ in the drift-frame, perpendicular kinetic energy exceeded some fraction of the binding energy U, the atom was considered chaotic. The dots show the fraction of atoms meeting this criterion. The frequency condition

$$\omega_{\text{eff}} > \frac{1}{2}\Omega_c$$

more accurately predicts the chaotic fraction based on this criterion than the more stringent requirement of Eq. (1.26).

1.2.1 Chaotic phase space distributions

Since the cyclotron action is eliminated as an adiabatic invariant in chaotic atoms, we can no longer neglect perpendicular kinetic energy in the Hamiltonian. The internal energy definition of Eq. (1.1), in orbital (check) units and spherical coordinates is

$$1 = \frac{1}{\check{r}} - \frac{1}{2}\check{v}^2, \tag{1.29}$$

where the magnitude $\check{v}$ now includes the full, three-dimensional velocity. Inclusion of the perpendicular degrees of freedom changes the dimensionality of phase space, with a corresponding change in the probability $P(\check{r}, \check{v}_z, \check{v}_\perp)$. In particular, the fully ergodic phase space distribution varies with the magnitude $\check{v}_\perp$ of the perpendicualr

velocity. Strictly speaking, this distribution, like the internal energy, is a function of the total magnitude

$$\check{v} = \sqrt{\check{v}_z^2 + \check{v}_\perp^2}.$$

However, we have chosen to separate the $\check{v}_z$ and $\check{v}_\perp$ dependence to connect with the guiding-center atom case. In analogy with Eq. (1.19), the phase-space distribution is given by

$$P(\check{r}, \check{v}_z, \check{v}_\perp) = \frac{\check{r}^2 \check{v}_\perp \delta\Big(1 - \frac{1}{\check{r}} + \frac{1}{2}(\check{v}_z^2 + \check{v}_z^2)\Big)}{\int \delta\Big(1 - \frac{1}{\check{r}} + \frac{1}{2}(\check{v}_z^2 + \check{v}_z^2)\Big)\, \check{r}^2 \check{v}_\perp d\check{r} d\check{v}_z d\check{v}_\perp}. \tag{1.30}$$

The individual ergodic distributions are accordingly given by integrals of Eq. (1.30).

$$P_r(\check{r}) = \int P(\check{r}, \check{v}_z, \check{v}_\perp)\, d\check{v}_z d\check{v}_\perp = \frac{16}{\pi} \check{r}^{3/2} \sqrt{1 - \check{r}} \tag{1.31}$$

$$P_{v_z}(\check{v}_z) = \int P(\check{r}, \check{v}_z, \check{v}_\perp)\, d\check{r} d\check{v}_\perp = \frac{32\sqrt{2}}{3\pi} \left(2 + \check{v}_z^2\right)^{-3} \tag{1.32}$$

$$P_{v_\perp}(\check{v}_\perp) = \int P(\check{r}, \check{v}_z, \check{v}_\perp)\, d\check{r} d\check{v}_z = 16 \check{v}_\perp (2 + \check{v}_\perp^2)^{-3} \tag{1.33}$$

The blue curves in Fig. 1.3 show these probability distributions.

To test the validity of the distinct guiding-center and chaotic probability distributions in phase space, we followed the motion of three stochastic ensembles of 500 atoms. We populated each ensemble according to the guiding-center distribution in Eq. (1.19), then followed the orbits using the full, three-dimensional equations of motion. A time average of the particle positions was then used to generate a new distribution in phase space. We find that atoms begun at low binding energies, well below the chaotic cutoff energy, primarily adhere to the guiding-center distribution. One notable exception to this rule is in $P_r(\check{r})$, where

even weakly bound atoms show deviation from the $\vec{v}_\perp = 0$ distribution near the nucleus (small $\check{r}$). These are atoms like the one in Fig. 1.6(b).

As binding energy increases, however, the distribution shifts toward the fully-ergodic one predicted for chaotic atoms. Atoms populate the appropriate phase-space distribution to the extent allowed by angular momentum conservation. Because angular momentum p_ϕ is conserved, the distribution in this variable must remain fixed. Thus, the atoms are restrained from assuming the true, fully-ergodic distribution. A close approximation to this distribution is nevertheless reached in the observable phase space variables r, v_z, and $v_\perp$.

The distribution of angular momenta in the fully-ergodic case differs from the guiding-center case. To calculate it, we must, as before, switch to cylindrical coordinates. Now we use the full form of the Hamiltonian, expressed in orbital units.

$$-H = 1 = \frac{1}{(\check{\rho}^2 + \check{z}^2)^{1/2}} - \frac{1}{2}\left(\check{p}_z^2 + \check{p}_\rho^2 + \left(\frac{\check{p}_\phi}{\check{\rho}} - \frac{1}{2}\check{\rho}\check{\Omega}_c\right)^2\right)$$

The probability $P_{p_\phi}(\check{p}_\phi)$ of finding an atom at angular momentum $\check{p}_\phi$ is

$$\begin{aligned} P_{p_\phi}(\check{p}_\phi) &= \frac{\int \delta\left(1 - \frac{1}{(\check{\rho}^2+\check{z}^2)^{1/2}} + \frac{1}{2}\left(\check{p}_z^2 + \check{p}_\rho^2 + \left(\frac{\check{p}_\phi}{\check{\rho}} - \frac{1}{2}\check{\rho}\check{\Omega}_c\right)^2\right)\right) d\check{\rho}d\check{z}d\check{p}_\rho d\check{p}_z}{\int \delta\left(1 - \frac{1}{(\check{\rho}^2+\check{z}^2)^{1/2}} + \frac{1}{2}\left(\check{p}_z^2 + \check{p}_\rho^2 + \left(\frac{\check{p}_\phi}{\check{\rho}} - \frac{1}{2}\check{\rho}\check{\Omega}_c\right)^2\right)\right) d\check{\rho}d\check{z}d\check{p}_\rho d\check{p}_z d\check{p}_\phi} \\ &= \frac{4\sqrt{2}}{\pi}\int_{\check{\rho}_{\min}}^{\check{\rho}_{\max}} \sqrt{4\left(2 + \left(\frac{\check{p}_\phi}{\check{\rho}} - \frac{\check{\rho}\check{\Omega}_c}{2}\right)^2\right)^{-2} - \check{\rho}^2}. \end{aligned} \tag{1.34}$$

The limits $\check{\rho}_{\min}$ and $\check{\rho}_{\max}$ are the values of $\check{\rho}$ for which the integrand in Eq. (1.34) vanishes. At $\check{\Omega}_c = \check{p}_\phi = 0$, they go to 0 and 1, respectively. This probability is shown alongside the prediction for the guiding-center ($\vec{v}_\perp = 0$) case in Fig. 1.4. For

chaotic atoms, the fully ergodic distribution of Eq. (1.34) is more physical than its guiding-center approximation counterpart from Eq. (1.24). The minimum $\check{p}_{\phi\min}$ and maximum $\check{p}_{\phi\max}$ accessible values of $\check{p}_\phi$ for a given $\check{\Omega}_c$ occur at the angular momentum values where $\check{\rho}_{\min} = \check{\rho}_{\max}$. These correspond to circular orbits in the $z = 0$ plane with opposite sense.

1.2.2 Chaotic magnetic moment

Let us again consider the magnetic moment, this time assuming the fully ergodic distribution of Eq. (1.30). Now that the distribution includes perpendicular kinetics, we can obtain the magnetic moment directly. Confinement occurs when the moment $\vec{\mu}$ is oriented antiparallel to the background magnetic field $\vec{B}$. The instantaneous magnetic moment is proportional to the kinematic angular momentum $\vec{L}$ [25]. Only the z component μ_z is important for confinement. We consider the time average because $\vec{L}$ is not conserved in the magnetic field.

$$\left\langle \vec{\mu} \cdot \vec{B} \right\rangle \propto \left\langle \check{L}_z \right\rangle = \left\langle \check{p}_\phi - \frac{1}{2}\check{\rho}^2 \check{\Omega}_c \right\rangle$$

Of course the canonical momentum p_ϕ is still conserved, and the confinement condition becomes

$$\langle \mu_z \rangle \propto \check{p}_\phi - \frac{1}{2}\check{\Omega}_c \left\langle \check{\rho}^2 \right\rangle < 0. \tag{1.35}$$

If the orbit is metrically transitive, an ergodic, phase-space average is equivalent to a long-time average. While each chaotic orbit may not transit all available phase space given a fixed internal energy U (or equivalently $\check{\Omega}_c$) and azimuthal momentum p_ϕ, the ergodic average provides an accessible estimate of the time

average. Interpreting the average in Eq. (1.35) as a phase-space average at fixed p_ϕ gives

$$\left\langle \check{\rho}^2 \right\rangle = \frac{\sqrt{2}}{\pi^2 P_{p_\phi}(\check{p}_\phi)} \times \int \check{\rho}^2 \delta\left(1 - \frac{1}{(\check{\rho}^2+\check{z}^2)^{1/2}} + \frac{1}{2}\left(\check{p}_z^2 + \check{p}_\rho^2 + \left(\frac{\check{p}_\phi}{\check{\rho}} - \frac{1}{2}\check{\rho}\check{\Omega}_c\right)^2\right)\right) d\check{\rho}d\check{z}d\check{p}_\rho d\check{p}_z.$$

All but one of the integrals can be done analytically and the expression for $\langle\check{\rho}^2\rangle$ reduces to

$$\left\langle \check{\rho}^2 \right\rangle = \frac{4\sqrt{2}}{\pi P_{p_\phi}(\check{p}_\phi)} \int_{\check{\rho}_{\min}}^{\check{\rho}_{\max}} \check{\rho}^2 \sqrt{4\left(2 + \left(\frac{\check{p}_\phi}{\check{\rho}} - \frac{1}{2}\check{\rho}\check{\Omega}_c\right)^2\right)^{-2} - \check{\rho}^2} d\check{\rho}.$$

The fraction of confined atoms in the chaotic distribution, shown in Fig. 1.5 (red curve) as a function of binding energy ϵ at $\chi = 0.001$, approaches 0.5 as the atom enters the unmagnetized regime. The predicted confined fraction increases with ϵ. At low binding energy ϵ, atoms are expected to be distributed according to guiding-center phase space (i.e. Eq. (1.24)), not the fully-ergodic distribution of Eq. (1.34) used in this section to derive the magnetic moment μ. In this range, the magnetic moment estimate of the previous section, where cyclotron action was assumed fixed at the thermal energy, provides a more physical picture. In actual atoms, the confined fraction decreases with binding energy until cyclotron energy couples to atomic orbits, creating a chaotic atom. Then confinement increases with binding energy. For $\chi = 0.001$, half the atoms are chaotic at about $\epsilon = 35$, well beyond the cross point of the two curves in Fig. 1.5.

As a point of comparison, we simulated 1000 atoms at a number of different binding energies ϵ. The initial conditions were chosen from guiding-center phase

space except that each atom was given cyclotron action at the thermal level with random phase ψ:

$$\vec{v}_{\perp} = \vec{v}_{\vec{E}\times\vec{B}} + \bar{v}\left(\cos\psi\vec{a}_x + \sin\psi\vec{a}_y\right).$$

Full three-dimensional dynamics were kept. The average magnetic moment was calculated for each atom after a few parallel bounce times. Those atoms with an average moment less than zero are considered confined. The fraction of such confined atoms in this simulation are the black dots in Fig. 1.5. Even though the distribution of initial conditions does not obey the fully ergodic form appropriate for chaotic atoms (Eq. (1.30)), magnetic moments at deep binding are distributed as predicted for chaotic atoms. The distribution naturally switches over to the chaotic form, within the constraints of angular momentum conservation, as the chaotic cutoff energy is approached.

While atoms remain in the guiding-center regime the fraction of combined atoms monotonically decreases with binding energy. However, as atoms cascade into the chaotic orbit regime, the magnetically confined fraction increases to approximately the unmagnetized value of 0.5. Thus the transition from guiding-center to chaotic orbits represents an important threshold not only for radiative relaxation (as will be seen in Chapter 4), but also for magnetic confinement.

Chapter 2

Collisional Average Energy-Loss Rate

For antihydrogen to be useful for spectroscopy measurements, it must be at or near the ground state. The highly-excited states discussed in the previous chapter must relax to deep binding before they can used for this purpose. However, the slow $\vec{E} \times \vec{B}$ motion that dominates in guiding-center atoms precludes radiative energy loss above the cyclotron rate. In most plasmas, collisions remove energy from the atom much more quickly than radiation, allowing relaxation into the chaotic regime. There radiation takes over as the dominant form of energy loss.

Collisional energy loss is treated in this chapter. The process by which a guiding-center or chaotic atom loses energy to the surrounding plasma can be divided into two components: close collisions and distant collisions. Infrequent, close collisions that cause large steps in binding energy are analytically intractable and are treated herein by a Monte-Carlo code. The code gives a transition probability rate density, the moments of which give average energy loss. The rate will also be used in the next chapter to determine the time evolution of a physical ensemble of

atoms. Large-impact-parameter collisions, where the perturbations to atomic and free particle orbits are small, can be treated analytically.

We examine the large-impact-parameter case from two perspectives. First, we develop a Fokker-Planck theory for the energy loss. Transport coefficients are calculated by integrating over unperturbed orbits, then an Einstein relation gives the atom's mobility to deeper binding. Second, we consider an atom immersed in a thermal positron plasma and calculate the work exerted on the bound positron orbit by the wake it excites in the plasma. In both analysis we focus on guiding-center atoms because they have integrable orbits and are more tractable. The two theories are found to agree well with each other and with output from the Monte-Carlo simulation, which treats both small and large impact parameters in both guiding-center and chaotic regimes.

2.1 Monte-Carlo Simulation Procedure

The simulation consists of many independent shots of a free positron impacting an atom, as in Ref. [8]. Initial conditions in each shot are taken from the same distribution. The atomic binding energy is fixed from shot to shot, but all other atomic variables are populated on an ergodic surface. The free particle is picked from a uniform, thermal distribution.

Guiding-center equations of motion are used at the outset, but the simulation switches to three-dimensional (i.e., cyclotron-inclusive) dynamics if the distance between any two of the three charges (bound positron, free positron, and

antiproton nucleus) becomes less than $r_{\text{switch}} = 2r_{\text{chaotic}} = 2\chi^{-2/3}$. When charges are separated by the chaotic cutoff radius r_{chaotic}, the $\vec{E} \times \vec{B}$ drift orbit frequency is equal to the cyclotron frequency Ω_c and cyclotron action is no longer a good adiabatic invariant. If a switch to full dynamics occurs, the simulation replaces each guiding-center with a point particle in the same position, initially at rest. This prescription conserves total energy and angular momentum.

Let us define a dimensionless form for angular momentum.

$$\hat{p}_\phi = \frac{p_\phi}{m_e \bar{v} b}$$

Recall that in the guiding-center-drift approximation,

$$\epsilon = \frac{1}{\hat{r}} - \frac{1}{2}\hat{v}_z^2. \tag{2.1}$$

At a specified atomic binding energy ϵ_0, we choose initial conditions for the atom from the guiding-center ergodic distribution in phase space. The distribution is dictated by the guiding-center drift Hamiltonian Eq. (2.1), so the initial perpendicular velocity is always zero. As observed in Chapter 1, the ergodic distribution dictated by a three-dimesional Hamiltonian, where perpendicular momenta are also uniformly populated, differs qualitatively from the guiding-center distribution used. When the cyclotron action is well conserved, however, phase space variables associated with perpendicular kinetic energy are not expected to be ergodically populated. Instead, the perpendicular kinetic energy is expected to remain at the thermal level. Only as cyclotron motion begins to participate in the dynamics, and

the adiabatic invariance is broken, do these degrees of freedom become ergodic as well.

We saw in Chapter 1 that, in practice, the positron orbit ergodically covers the available energy surface, naturally establishing the appropriate distribution $P(x, y, z, p_x, p_y, p_z)$. Fig. 1.3 shows the distributions of three atomic ensembles in r, v_z, and $v_\perp$, — each begun with the guiding-center distribution ($\vec{v}_\perp = 0$), as in the simulation — averaged over time. At each binding energy, atom orbits establish the appropriate distribution, evolving from the guiding-center form to the three-dimensional form continuously to the extent allowed by conservation of p_ϕ. Atom orbits thus ensure the appropriate distribution before the collision occurs.

For the free positron, the initial parallel velocity in every shot is chosen from a Maxwellian distribution at temperature T. If the simulation switches over to full dynamics, the perpendicular velocities of both the free and bound positron begin at zero, conserving total energy and canonical angular momentum p_ϕ. Setting the free particle's initial perpendicular kinetic energy to zero is equivalent to setting the positron plasma perpendicular temperature to zero. The probable effect of this last choice is a slight enhancement of the cascade to deep binding. However, in some high-B-field and low temperature trap configurations, a two-temperature distribution ($T_\perp << T_\parallel$) may actually be physical, since cyclotron cooling affects only the perpendicular temperature while heating due to field errors mainly acts on the parallel temperature. Furthermore, perpendicular to parallel temperature equilibration is exponentially suppressed in the strongly-magnetized regime $\chi << 1$

[26]. Simulations for $T_\perp = T_\parallel$ will be presented in a future paper.

The free positron's initial position relative to the guiding-center atom orbit is chosen with equal probability for equal area, with radius restricted to $0 < \hat{\rho}_p < 10/\epsilon_0$.

We must initially place the impacting positron far enough away in z to approximate a collision from infinity. The distance is largest for large impact parameter collisions. As the free positron approaches the atom, the bound positron's drift orbit becomes distorted, resulting in fluctuations in the orbit's cylindrical radius ρ with period ω_ϕ (the drift frequency) and magnitude of order

$$\delta\hat{\rho} = \frac{\hat{\rho}^3\hat{\rho}_p^3}{\hat{z}_p^3}.$$

The predicted step in cylindrical radius $\Delta\hat{\rho}$ for a large impact parameter collision comes from an integral over unperturbed orbits (Eq. (2.20) below). For appropriate accuracy, we require that $\Delta\hat{\rho} >> \delta\hat{\rho}_{\min}$, where $\delta\hat{\rho}_{\min}$ occurs at $\hat{z}_{\text{limit}}$. Choosing $\sin(\theta) = -1/2$ for simplicity, we obtain

$$\hat{z}_{\text{limit}}^3 >> \frac{\hat{\rho}_p\hat{\rho}^6\hat{v}_z}{\chi^2 K_1\left(\frac{\hat{\omega}_\phi\hat{\rho}_p}{\hat{v}_z}\right)}. \tag{2.2}$$

The free positron is initially placed at ten times the $\hat{z}$ separation dictated by Eq. (2.2) and the run is ended when either positron reaches the same $\hat{z}$-separation again.

2.2 Collisional Transition Probability Rate Density

In this section, we evaluate $w(\epsilon, \epsilon')$, the mean rate of transition of an atom from energy ϵ to energy ϵ' averaged over all other variables. Since atom orbits appear to fill phase space in a qualitatively ergodic manner (Fig. 1.3), we consider only the evolution of the distribution $f(\epsilon)$, with the assumption that all other variables are populated ergodically. We will use the collisional transition rate $w(\epsilon, \epsilon')$ constructed here in the next chapter to determine the evolution of a distribution of weakly-bound atoms to deeper binding, considering only transitions due to collisions with free positrons. Radiative transitions will be considered in the last chapter. The master equation gives the time evolution of $f(\epsilon)$ due to collisions.

$$\frac{\partial f}{\partial t} = \int \left[f(\epsilon')\, w(\epsilon', \epsilon) - f(\epsilon)\, w(\epsilon, \epsilon') \right] d\epsilon' \tag{2.3}$$

For any transition probability rate density $w(\epsilon, \epsilon')$,

$$\int w(\epsilon, \epsilon')\, d\epsilon' \equiv \nu_{\text{eff}} = \frac{\text{total number of events}}{\text{time}}.$$

The rate extracted from the simulation includes collisions within a disk of radius

$$\hat{\rho}_{\max} = \frac{10}{\epsilon},$$

or ten times the atom radius, for each initial binding energy considered. The effective collision frequency ν_{eff} is then

$$\begin{aligned} \nu_{\text{eff}} &= n\bar{v}b^2\pi\hat{\rho}_{\max}^2 \frac{\int_{-\infty}^{\infty} |\hat{v}_z| e^{-\hat{v}_z^2/2} d\hat{v}_z}{\int_{-\infty}^{\infty} e^{-\hat{v}_z^2/2} d\hat{v}_z} \\ &= n\bar{v}b^2\sqrt{2\pi}\frac{100}{\epsilon^2}. \end{aligned} \tag{2.4}$$

The function $w(\epsilon, \epsilon')$ should also obey detailed balance. This requires the integrand in Eq. (2.3) to vanish when the distribution function takes the thermal equilibrium form $f_{\rm th}(\epsilon)$.

$$f_{\rm th}(\epsilon)\, w(\epsilon, \epsilon') = f_{\rm th}(\epsilon')\, w(\epsilon', \epsilon) \tag{2.5}$$

For $v_\perp = 0$ (and $T_\perp$=0), the thermal equilibrium density of particles in phase space is

$$P_{\rm th}(\epsilon) = \frac{n}{(2\pi\bar{v}^2)^{1/2}} e^{\epsilon}.$$

This form neglects positron-positron interactions, equivalent to assuming $nb^3 << 1$. In this limit, the number density $f_{\rm th}(\epsilon)$ is given by

$$f_{\rm th}(\epsilon) = \zeta(\epsilon)\, P_{\rm th}(\epsilon)\,,$$

where $\zeta(\epsilon)$ is the density of states at energy ϵ. The value of $\zeta(\epsilon_0)$ is equivalent to the area of the phase space surface defined by energy $\epsilon = \epsilon_0$.

$$\zeta(\epsilon) = 4\pi \int \delta(\epsilon_{GC}(r, v_z) - \epsilon_0)\, r^2 dr dv_z$$

Above, we use the guiding-center ($v_\perp$=0) expression for the energy appropriate for our simulation.

$$\epsilon_{GC}(\hat{r}, \hat{v}_z) = \frac{1}{\hat{r}} - \frac{1}{2}\hat{v}_z^2$$

The integral can be performed analytically.

$$f_{\rm th}(\epsilon) = \frac{5\pi^{3/2}}{8} nb^3 \frac{e^{\epsilon}}{\epsilon^{7/2}} \tag{2.6}$$

The $w(\epsilon, \epsilon')$ derived from our simulation should obey the detailed balance condition of Eq. (2.5) provided perpendicular energy can be neglected in collisional dynamics. We will see that the condition is met for weak to moderate binding, but is broken before the chaotic cutoff.

To extract $w(\epsilon, \epsilon')$, consider the evolution of a delta function $f(\epsilon)|_{t=0} = \delta(\epsilon - \epsilon_0)$ after a short time Δt.

$$f(\epsilon)|_{t=\Delta t} = \delta(\epsilon - \epsilon_0) + \left.\frac{\partial f}{\partial t}\right|_{t=0} \Delta t$$

Substituting in Eq. (2.3) gives

$$f(\epsilon)|_{t=\Delta t} = \delta(\epsilon - \epsilon_0) + \Delta t w(\epsilon_0, \epsilon) - \nu_{\text{eff}} \Delta t \delta(\epsilon - \epsilon_0)\,.$$

Recall that ν_{eff} (Eq. (2.4)) is the effective collision frequency for all considered collisions. If we let $\Delta t = \nu_{\text{eff}}^{-1}$, as is appropriate for one collision event, then

$$w(\epsilon_0, \epsilon) = \nu_{\text{eff}}\ f(\epsilon)|_{t=\nu_{\text{eff}}^{-1}}\,. \tag{2.7}$$

The distribution $f(\epsilon)$ on the right side of the equal sign is the distribution after one collision event, which is the distribution of final states from our Monte-Carlo simulation.

Fig. 2.1 shows $w(\epsilon, \epsilon')$ for $\epsilon = 4$ and $\epsilon = 20$. It shows that replacement collisions, where the free positron replaces the bound one, usually at deeper binding, constitute a larger fraction of collisions with large energy steps. Only a small fraction of collisions resulting in small energy steps were of this variety. For $w(\epsilon, \epsilon')$,

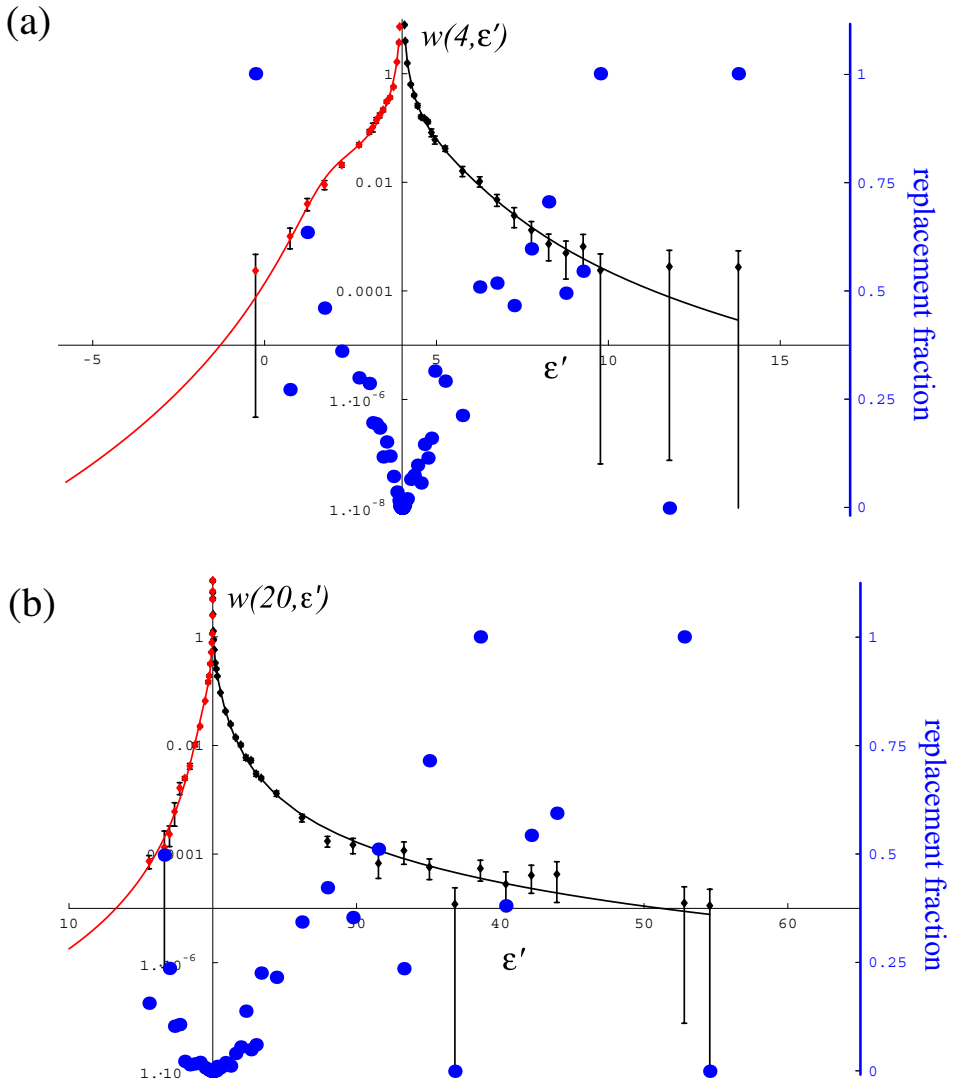

Figure 2.1: The transition probability rate densities $w(4, \epsilon')$ and $w(20, \epsilon')$ as extracted from the Monte-Carlo simulation. The lines represent fitting functions which are defined independently for the left and right sides of the distribution. A diffusive model is used to approximate the contribution to Eq. (2.3) from the region $-0.1 < (\epsilon' - \epsilon) < 0.1$, but a smoothed version of the fit is used for the rest of the integral. The blue dots (right axis) indicate the fraction of collisions in each bin where the bound positron was liberated and replaced by the initially free positron.

we have chosen a phenomenological fitting function of the form

$$w(\epsilon,\epsilon') = \begin{cases} \left(A_L\left(\epsilon-\epsilon'\right)^{\alpha_L} + B_L\left(\epsilon-\epsilon'\right)^{\beta_L}\right)^{-1} & \text{for} \quad \epsilon' < \epsilon \\ \left(A_R\left(\epsilon'-\epsilon\right)^{\alpha_R} + B_R\left(\epsilon'-\epsilon\right)^{\beta_R}\right)^{-1} & \text{for} \quad \epsilon' > \epsilon \end{cases} .$$

The fit parameters A, B, α, and β vary for different values of ϵ. They are defined at the discrete ϵ where the simulation was performed and appear in Tables 2.1— 2.3. To track the time evolution of a distribution in the next chapter, we require a smooth transition rate for all values of ϵ and ϵ' on a solution grid. To obtain this, we first calculated $w(\epsilon,\epsilon')$ on every grid point (excluding the singularity at $\epsilon = \epsilon'$) using linear interpolation between the discrete ϵ fits in one of Tables 2.1— 2.3. The solution grid runs from 0.1 to 100 in ϵ and ϵ', with a spacing of 0.1. Variation along ϵ was smoothed by replacing each point with an average of itself and the point along the line connecting the two adjacent points corresponding to the same value of $\Delta\epsilon = \epsilon' = \epsilon$, represented by the following algorithm:

$$w_{i,j} = \frac{1}{2}\left(w^{(0)}_{i,j} + w^{(0)}_{i-1,j} + \frac{w^{(0)}_{i+1,j} - w^{(0)}_{i-1,j}}{\epsilon_{i+1} - \epsilon_{i-1}}(\epsilon_i - \epsilon_{i-1})\right). \tag{2.8}$$

Above, the i and j indices represent ϵ and $\Delta\epsilon$ respectively. The values $w^{(0)}_{i,j}$ are the original, unsmoothed data with the singular point at $\epsilon = \epsilon'$ omitted. The algorithm was applied to every point but the endpoints. This procedure helps ensure a smoother, more physical time evolution of $f(\epsilon)$. Rapid, monotonic variation in $\Delta\epsilon$ precludes the need for smoothing in this parameter. Transitions near $\epsilon = \epsilon'$ were treated with a diffusive model (see below).

The fitting form is phenomenological and does not guarantee detailed balance, which would require that the integrand in Eq. (2.3) vanish when $f(\epsilon)$ takes

Table 2.1: The fitting parameters for $w(\epsilon, \epsilon')$ at $\chi = 0$ (infinite magnetic field). The left and right cutoffs are given by the functions $\Delta\epsilon_{\min} = -\frac{1}{2}\left(\frac{5.468\epsilon^{1.248}}{4.445+\epsilon^{1.248}} + \frac{6.010\epsilon^{1.321}}{4.353+\epsilon^{1.321}}\right)$ and $\Delta\epsilon_{\max} = \frac{1}{2}\left(0.777\epsilon^{1.049} + 1.160\epsilon^{1.073}\right)$

$\chi = 0$

	left fit				right fit				
ϵ	A_L	B_L	α_L	β_L	A_R	B_R	α_R	β_R	D_ϵ
0.1	0.1504	0.6056	23540.	2.502	0.1046	0.559	71590.	2.655	0.3554
1	70.88	1.415	6673.	12.29	15.25	1.131	698.7	2.395	0.04467
2	47.03	1.265	66.65	5.064	52.52	1.296	267.9	2.871	0.0109
3	76.52	1.431	0.3462	11.33	98.08	1.463	34.5	3.84	0.004253
4	65.74	1.315	10.68	4.693	87.73	1.386	14.49	4.943	0.002198
5	81.43	1.363	2.911	5.878	72.33	1.319	5.903	4.948	0.001216
7	81.34	1.274	3.138	5.673	62.91	1.176	10.53	3.426	0.0005259
10	81.15	1.207	20.94	3.862	57.61	1.041	9.884	3.076	0.0002043
13	105.3	1.247	14.43	4.214	81.01	1.196	0.002043	6.619	0.0001178
15	88.3	1.14	35.38	3.604	64.11	1.071	7.975	2.587	0.00008032
18	94.16	1.15	52.93	2.953	65.99	1.034	0.625	3.599	0.00004937
20	123.	1.218	11.27	5.029	90.76	1.136	0.0105	4.774	0.00003603
23	84.9	1.057	68.34	3.313	60.91	0.9181	3.651	2.752	0.00002359
25	146.7	1.265	26.19	3.613	69.14	0.9683	1.382	2.933	0.00002195
30	179.4	1.28	1.794	5.792	64.86	0.9684	1.915	2.719	0.00001304
40	80.43	0.9935	128.3	2.813	66.33	0.8854	5.307	2.311	7.144×10^{-6}
50	94.45	1.021	67.83	2.992	81.05	1.009	0.177	3.169	4.665×10^{-6}
60	106.3	1.026	67.06	3.665	73.96	0.9375	0.8536	2.619	2.914×10^{-6}
70	127.4	1.03	38.07	4.158	69.58	0.9128	1.504	2.436	2.027×10^{-6}
80	148.7	1.095	26.43	4.599	82.75	0.9705	0.08278	3.124	1.491×10^{-6}
90	105.4	0.9857	59.2	3.642	77.41	0.9405	0.4562	2.617	1.327×10^{-6}
100	138.	1.058	21.71	4.576	75.81	0.9044	0.271	2.825	9.751×10^{-7}

Table 2.2: The fitting parameters for $w(\epsilon, \epsilon')$ at $\chi = 0.001$. The left and right cutoffs are given by the functions $\Delta\epsilon_{\min} = -\frac{1}{2}\left(\frac{5.045\epsilon^{1.218}}{2.844+\epsilon^{1.218}} + \frac{5.307\epsilon^{1.235}}{2.949+\epsilon^{1.235}}\right)$ and $\Delta\epsilon_{\max} = \frac{1}{2}\left(1.182\epsilon^{1.083} + 2.001\epsilon^{1.115}\right)$.

$\chi = 0.001$

	left fit				right fit				
ϵ	A_L	B_L	α_L	β_L	A_R	B_R	α_R	β_R	D_ϵ
0.1	4037.	2.126	2.001×10^{10}	7.853	8853.	2.203	8.415×10^{7}	5.158	0.3819
1	68.56	1.421	3607.	10.51	54.41	1.369	717.5	2.767	0.0478
2	79.39	1.539	3.315	10.61	77.72	1.424	214.1	3.375	0.01163
3	67.69	1.45	6.606	6.499	72.71	1.446	74.48	3.359	0.007069
4	86.72	1.68	0.09073	9.453	91.26	1.707	10.42	4.351	0.007572
5	87.12	1.938	2.43	5.527	90.23	1.974	1.349	4.879	0.009146
7	92.19	2.398	0.01602	9.16	55.3	2.166	1.843	3.892	0.009197
10	0.4479	0.4127	54.47	3.078	0.4816	0.4709	24.08	2.689	0.004058
13	1.838	0.7418	29.06	3.905	0.8423	0.4916	11.07	2.781	0.001656
15	2.211	0.7622	20.41	4.053	1.56	0.6736	6.527	2.786	0.001091
18	5.459	1.09	6.583	4.85	3.665	0.9685	2.645	3.05	0.0006658
20	5.832	1.043	6.205	4.351	2.277	0.7394	5.004	2.476	0.0004979
23	13.66	1.395	0.5089	6.285	5.507	1.051	1.857	2.804	0.0003584
25	11.91	1.265	2.41	5.176	7.423	1.144	0.7153	3.098	0.0002835
30	21.64	1.477	0.6371	6.03	11.43	1.263	0.1325	3.436	0.0001755
40	42.61	1.675	2.565	4.915	15.4	1.32	0.03025	3.42	0.00009484
50	35.02	1.504	77.9	3.38	17.44	1.339	0.001338	3.944	0.00006089
60	54.03	1.515	57.2	3.668	15.62	1.28	0.0001166	4.488	0.00003253
70	37.83	1.284	86.61	3.396	12.01	1.294	1.478×10^{-10}	7.454	0.00002655
80	30.61	1.144	15.31	4.476	11.74	1.236	0.002453	3.457	0.000016
90	14.39	0.9845	10.42	4.987	13.55	1.279	0.001039	3.438	0.00001227
100	10.01	0.9653	5.311	5.08	14.31	1.32	0.0004292	3.628	0.00001096

Table 2.3: The fitting parameters for $w(\epsilon, \epsilon')$ at $\chi = 0.005$. The left and right cutoffs are given by the functions $\Delta\epsilon_{\min} = -\frac{1}{2}\left(\frac{4.208\epsilon^{1.344}}{1.885+\epsilon^{1.344}} + \frac{4.160\epsilon^{1.349}}{1.842+\epsilon^{1.349}}\right)$ and $\Delta\epsilon_{\max} = \frac{1}{2}\left(2.668\epsilon^{1.240} + 1.242\epsilon^{1.264}\right)$.

$\chi = 0.005$

	left fit				right fit				
ϵ	A_L	B_L	α_L	β_L	A_R	B_R	α_R	β_R	D_ϵ
0.1	1.06×10^{8}	5.88	2735.	2.031	5.456	1.097	71140.	2.844	0.3907
1	74.82	1.49	950.3	7.04	136.3	1.624	519.3	3.377	0.04744
3	90.44	1.953	0.06559	11.5	134.8	2.12	0.7302	6.487	0.02237
5	54.22	2.101	4.352	5.705	27.01	1.848	11.23	3.333	0.01564
7	7.026	1.266	37.06	3.569	6.965	1.29	8.924	3.039	0.006272
10	19.73	1.541	2.69	5.838	13.05	1.391	1.467	3.38	0.001981
12	21.24	1.451	4.195	5.236	17.43	1.44	0.3521	3.63	0.001106
15	55.4	1.711	0.2511	7.284	24.5	1.484	0.008166	4.339	0.0005819
20	77.61	1.636	13.29	4.819	24.34	1.258	0.06354	3.44	0.0002192
25	22.51	1.207	86.02	3.253	15.05	1.38	0.001401	4.177	0.0002044
30	13.96	1.172	32.51	4.841	17.43	1.375	0.002155	3.8	0.000163
35	8.743	1.053	16.9	5.32	16.09	1.407	0.003868	3.584	0.0001592
40	2.151	0.6582	37.17	4.065	15.19	1.57	0.00004856	4.233	0.0001379
50	1.09	0.4703	61.87	4.212	9.523	1.76	0.06523	3.611×10^{-9}	0.0000964
60	0.4087	0.1642	58.77	3.458	8.247	1.678	0.0639	5.399×10^{-11}	0.00006646
70	0.5294	0.1882	43.36	3.119	0.1172	4.028×10^{-9}	3.991	1.663	0.00005243
80	0.529	0.1931	50.44	3.368	9.45	1.464	9.435×10^{-6}	3.957	0.00004186
90	2.07	0.6824	27.06	3.557	9.227	1.41	0.00009837	3.373	0.00003473
100	3.856	0.9123	15.65	3.976	8.905	1.337	7.067×10^{-8}	4.665	0.00002848

the thermal equilibrium form. Since a two-temperature ($T_\perp = 0$) distribution is used in the simulation, thermal equilibrium is somewhat ill-defined. At shallow binding, cyclotron action is nearly conserved in both the atom and the free particle, so perpendicular temperature is irrelevant. At deep binding, however, close collisions are more likely to cause energy exchange in the perpendicular degree of freedom.

In Fig. 2.2, we compare the two terms in Eq. (2.3) for three values of the atomic binding energy ϵ to check detailed balance. The thermal equilibrium distribution function $f_{th}(\epsilon)$ used is the one appropriate for the guiding-center drift atom regime ($\vec{v}_\perp = 0$).

The fit diverges at $\epsilon = \epsilon'$, so does not describe the central peak accurately. However, the small steps in energy accounted for in this narrow region can be treated with Fokker-Planck theory. The contribution to the integral in the master equation from the region $-\delta\epsilon < (\epsilon' - \epsilon) < \delta\epsilon$ is approximated by expanding the first term in the integrand of Eq. (2.3).

To facilitate derivation of the Fokker-Planck equation, we define $\mathcal{W}(\epsilon, \Delta\epsilon) = w(\epsilon, \epsilon - \Delta\epsilon)$. Letting $\epsilon' = \epsilon + \Delta\epsilon$, we get

$$\begin{aligned}\int_{\epsilon-\delta\epsilon}^{\epsilon+\delta\epsilon} f(\epsilon')\, w(\epsilon', \epsilon)\, d\epsilon' &= \int_{-\delta\epsilon}^{\delta\epsilon} f(\epsilon + \Delta\epsilon)\, \mathcal{W}(\epsilon + \Delta\epsilon, \Delta\epsilon)\, d\Delta\epsilon \\ &\approx \int_{-\delta\epsilon}^{\delta\epsilon} \Bigg(f(\epsilon)\, \mathcal{W}(\epsilon, \Delta\epsilon) + \Delta\epsilon \frac{\partial}{\partial\epsilon} \left(f(\epsilon)\, \mathcal{W}(\epsilon, \Delta\epsilon) \right) \\ &\qquad + \frac{1}{2}\Delta\epsilon^2 \frac{\partial^2}{\partial\epsilon^2} \left(f(\epsilon)\, \mathcal{W}(\epsilon, \Delta\epsilon) \right) \Bigg) d\Delta\epsilon. \end{aligned} \tag{2.9}$$

Reverting to notation in terms of $w(\epsilon, \epsilon')$, substitution of Eq. (2.9) into Eq. (2.3)

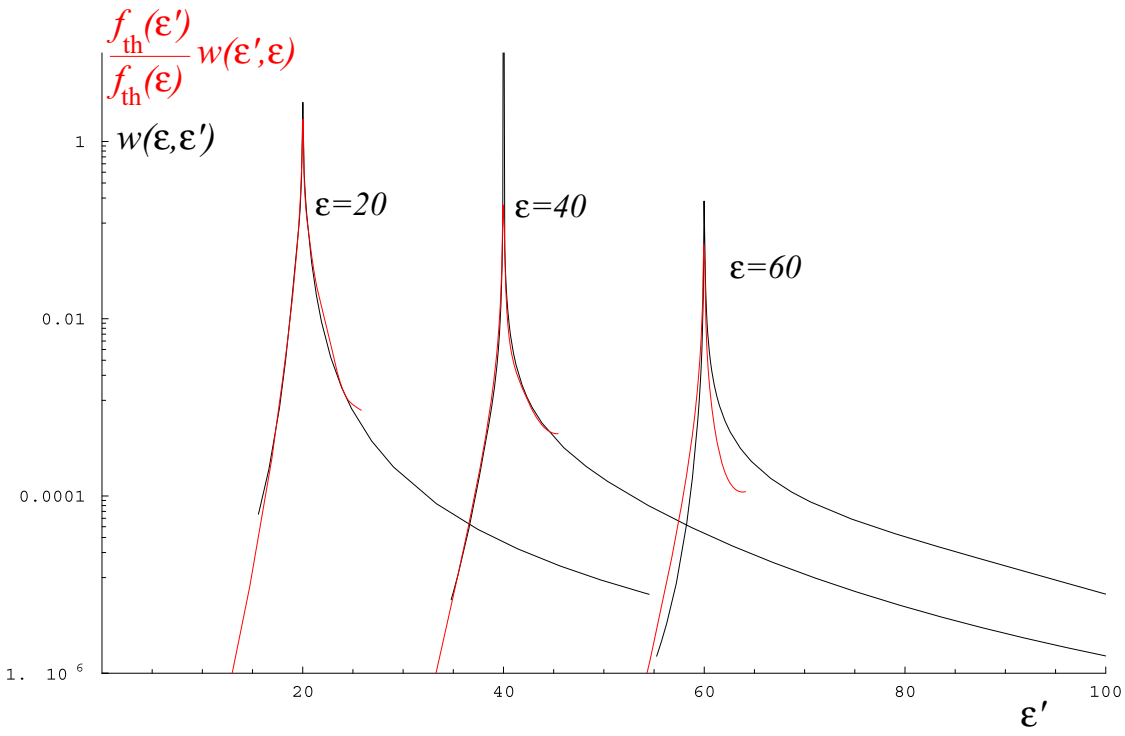

Figure 2.2: A comparison of $(f_{\rm th}(\epsilon')/f_{\rm th}(\epsilon))w(\epsilon',\epsilon)$ (red) and $w(\epsilon,\epsilon')$ (black) (rescaled forms of the first and second terms in Eq. (2.3) in thermal equilibrium) for three energies ϵ (20, 40, and 60) and plotted against ϵ'. Detailed balance requires the two terms to be equal. At large ϵ, detailed balance fails because the zero-temperature, perpendicular degrees of freedom participate in the collision.

gives

$$\frac{\partial f}{\partial t} = \int_{-\infty}^{\epsilon-\delta\epsilon} \left(f(\epsilon')\, w(\epsilon',\epsilon) - f(\epsilon)\, w(\epsilon,\epsilon')\right) d\epsilon' - \frac{\partial}{\partial \epsilon}\left(M_{\delta\epsilon}(\epsilon)\, f(\epsilon) - D_{\delta\epsilon}(\epsilon)\, \frac{\partial f}{\partial \epsilon}\right) + \int_{\epsilon+\delta\epsilon}^{\infty} \left(f(\epsilon')\, w(\epsilon',\epsilon) - f(\epsilon)\, w(\epsilon,\epsilon')\right) d\epsilon', \tag{2.10}$$

where the diffusion coefficient $D_{\delta\epsilon}(\epsilon)$ and mobility coefficient $M_{\delta\epsilon}(\epsilon)$ are defined:

$$D_{\delta\epsilon}(\epsilon) \equiv \frac{1}{2}\int_{\epsilon-\delta\epsilon}^{\epsilon+\delta\epsilon} (\epsilon'-\epsilon)^2\, w(\epsilon,\epsilon')\, d\epsilon' \tag{2.11}$$

$$M_{\delta\epsilon}(\epsilon) \equiv \int_{\epsilon-\delta\epsilon}^{\epsilon+\delta\epsilon} (\epsilon'-\epsilon) w(\epsilon,\epsilon')\, d\epsilon' + \frac{\partial}{\partial\epsilon} D_{\epsilon}(\epsilon) \tag{2.12}$$

In thermal equilibrium, the condition of detailed balance requires

$$M_{\delta\epsilon}(\epsilon)\, f_{\rm th}(\epsilon) - D_{\delta\epsilon}(\epsilon)\, \frac{\partial f}{\partial \epsilon} = 0,$$

where $f_{\rm th}(\epsilon)$ is the thermal equilibrium distribution. This implies an Einstein relation for $M_{\delta\epsilon}$ and $D_{\delta\epsilon}$:

$$M_{\delta\epsilon}(\epsilon) = D_{\delta\epsilon}(\epsilon)\, \frac{\partial f_{\rm th}/\partial\epsilon}{f_{\rm th}(\epsilon)}. \tag{2.13}$$

Either coefficient can be extracted from the discrete simulation output, with the integral in Eqs. (2.11) and (2.12) being replaced by a sum over points in the range $[\epsilon-\delta\epsilon, \epsilon+\delta\epsilon]$. However, since $M_{\delta\epsilon}$ involves a first moment of $w(\epsilon,\epsilon')$ as well as a derivative of $D_{\delta\epsilon}$ (which is itself defined only at discrete ϵ), we choose to use the Einstein relation for $M_{\delta\epsilon}$. While detailed balance doesn't hold for deeply bound atoms, it does for more weakly bound guiding-center atoms. Given the discrete simulation data, the $M_{\delta\epsilon}$ generated by Eq. (2.13) varies much more smoothly than its counterpart determined by Eq. (2.12).

We truncate the fit $w(\epsilon, \epsilon')$ near the energy of the largest observed transition from the simulation, for both $\epsilon' > \epsilon$ and $\epsilon' < \epsilon$. Outside the range $\Delta\epsilon_{\min} < \epsilon' - \epsilon < \Delta\epsilon_{\max}$, $w(\epsilon, \epsilon')$ is set to zero. If the power law tail in Fig. 2.1 is included, as many as 20 transition events are predicted to occur in the removed region for the simulated number of collisions. In fact, no transitions appear in this region, justifying the removal. The cutoff has a clear physical meaning for negative transitions. Jumps larger than $\epsilon' - \epsilon < 1$ will be exponentially unlikely because a thermal positron cannot impart more energy to the atom than it already has. For positive transitions, there is no obvious physical explanation for the cutoff. Truncation of the tail in $w(\epsilon, \epsilon')$ is further tested in the section on distribution evolution. The cutoff energies are given as functions of ϵ for different values of χ in the captions of Tables 2.1— 2.3.

2.3 Large Impact Parameters: Atom-Particle Interactions

Here we test the results of our simulation against a Fokker-Planck theory for collisions with large impact parameter. In the drift approximation, we develop a theoretical expression for the collision induced diffusion coefficient D_ϵ in the otherwise conserved energy ϵ. From an Einstein relation, we predict the first moment of $w(\epsilon, \epsilon')$ when only these large impact parameter collisions are considered. Good agreement is found at small to moderate binding energies ϵ, where guiding-center drift theory is applicable.

The development below follows [11], but includes the effect of z-axis bounce motion and preserves the diffusive term in the Fokker-Planck equation. Both effects decrease the energy-loss rate: the parallel degree of freedom picks up kinetic energy on adiabatic steps inward, reducing the net change in binding energy, and the diffusive term creates some flux away from the nucleus, resulting in a net decrease in energy-loss rate. In the analysis, collisions are assumed adiabatic in both z-axis and cyclotron dynamics. If the collision time is much greater than one parallel bounce period, guiding-center atom frequency ordering implies that it is also much longer than a cyclotron period.

$$\frac{\rho_{\min}}{\bar{v}} >> \omega_z^{-1} >> \Omega_c^{-1}. \tag{2.14}$$

Here, $\rho_{\min}$ is the minimum impact parameter considered. The assumption always holds for sufficiently large choice of $\rho_{\min}$.

Within the atom, cylindrical symmetry about the magnetic field implies conservation of momentum p_ϕ. In a collision, p_ϕ can change, but I_z and μ are still assumed static. For an ensemble of guiding-center atoms with distribution $f(I_z, p_\phi, \mu)$, the collisional adiabatic invariance of I_z and μ means that all energy change is due to changes in p_ϕ. The flux in energy space is:

$$\Gamma_\epsilon = M_\epsilon f - D_\epsilon \frac{\partial f}{\partial p_\phi}. \tag{2.15}$$

Here D_ϵ is the diffusion coefficient in coordinate ϵ and M_ϵ is the energy-space mobility. The mobility is related to the diffusion coefficient by an Einstein relation of the form of Eq. (2.13). Note that in the previous analysis, $D_{\delta\epsilon}$ and $M_{\delta\epsilon}$ were

determined for energy steps smaller than $\delta\epsilon$. Here, we are instead considering collisions with an impact parameter larger than $\rho_{\min}$.

The diffusion coefficient D_ϵ due to large-impact-parameter collisions is defined as

$$D_\epsilon = \frac{1}{2}\left\langle \nu \Delta\epsilon^2 \right\rangle . \tag{2.16}$$

Here, $\Delta\epsilon$ is the change in energy experienced in the collision. The average is over all initial conditions with large collisional impact parameters, including all atom initial conditions at fixed binding energy. The average over atomic variables is required to make D_ϵ a function of energy only, in keeping with a description of evolution in only this parameter. As before, if the distribution is a function of energy only, ergodically spread over phase space on each energy surface, then this description is self-consistent. The diffusion coefficient d_ϵ before the atom average is a function of both binding energy and atomic angular momentum. For colliding positrons streaming along the magnetic field lines at velocity v_z and intersecting the $z = 0$ plane at position $\vec{\rho}_p$,

$$d_\epsilon = \frac{1}{2}\int_{-\infty}^{\infty} |v_z|\, e^{-v_z^2/2\bar{v}} \frac{n}{\sqrt{2\pi}\bar{v}} \Delta\epsilon^2 d^2\rho_p dv_z. \tag{2.17}$$

Only energy changes due to angular momentum changes are significant, so

$$\Delta\epsilon \approx \frac{\partial\epsilon}{\partial p_\phi}\Delta p_\phi = -\hat{\omega}_\phi \Delta\hat{p}_\phi. \tag{2.18}$$

In the guiding-center drift approximation, we may discard the kinetic piece in the canonical angular momentum p_ϕ from Eq. (1.2). In this limit, a step in p_ϕ is

equivalent to a step along cylindrical radius ρ.

$$\Delta p_\phi \approx m_e \Omega_c \rho \Delta \rho \tag{2.19}$$

Consider a guiding center atom immersed in a magnetized positron plasma. The bound positron orbits the antiproton with frequency ω_ϕ. As long as the bounce frequency ω_z is much faster than the drift frequency ω_ϕ, the drift orbit can be considered of uniform speed. To first order, plasma positrons are confined to move along magnetic field lines at a constant velocity v_z. As each plasma positron travels by the atom, its electric field perturbs the drift velocity of the bound positron by

$$\vec{v}_1(t) = \frac{ce}{B} \frac{(\vec{r}(t) - \vec{r}_p(t)) \times \hat{\vec{z}}}{|\vec{r}(t) - \vec{r}_p(t)|^3}.$$

Here $\vec{r}(t)$ is the position of the bound positron, and $\vec{r}_p(t)$ is the position of the passing plasma positron. Without loss of generality, we can let the passing positron pass through the $z = 0$ plane at $t = 0$ when the bound positron is at $\phi = 0$ in its orbital cycle. We can therefore write

$$\begin{aligned} \vec{r}(t) &= r\left(\cos\omega_\phi t\, \vec{a}_x + \sin\omega_\phi t\, \vec{a}_y\right) \\ \vec{r}_p(t) &= x_p \vec{a}_x + y_p \vec{a}_y + v_z t \vec{a}_z. \end{aligned}$$

Above, $\vec{a}_\alpha$ is the unit vector along α. If the impact parameter ρ_p is much larger than the atom radius, the component of the bound positron's velocity perturbation in the direction of cylindrical radius ρ is

$$\vec{v}_\rho = \vec{v}_1 \cdot \vec{a}_\rho = \frac{ce}{B} \frac{(x_p \sin\omega_\phi t - y_p \cos\omega_\phi t)}{(x_p^2 + y_p^2 + v_z^2 t^2)^{3/2}}.$$

Integrating over all time gives the radial displacement from one collision,

$$\Delta\rho = -2\chi b^2 \bar{v}\sin(\phi)\left|\frac{\omega_\phi}{v_z^2}\right| K_1\left(\left|\frac{\omega_\phi \rho_p}{v_z}\right|\right). \tag{2.20}$$

where K_1 is the first modified Bessel function of the second kind.

This is the radial step taken in one collision where ϕ is the relative angle between the bound and passing positrons' position vectors at the moment when when the passing positron crosses the $z = 0$ plane. Combining Eqs. (2.17) through (2.20) gives the diffusion coefficient d_ϵ in the $\vec{E} \times \vec{B}$ drift approximation:

$$d_\epsilon = 2\sqrt{2\pi}(n\bar{v}b^2)\chi\hat{p}_\phi\hat{\omega}_\phi^2\mathcal{F}\left(\frac{\omega_\phi\rho_{\min}}{\bar{v}}\right), \tag{2.21}$$

with

$$\mathcal{F}(\xi) \equiv \int_\xi^\infty\int_{-\infty}^\infty s\, K_1^2\left(\frac{s}{|x|}\right)\frac{e^{-x^2/2}}{|x|^3}dxds. \tag{2.22}$$

This expression is valid in the guiding-center atom regime, defined as $\epsilon < \epsilon_c = \chi^{-2/3}$, for collisions with large impact parameter, and thus small individual steps in energy, only.

Lastly, we average d_ϵ from Eq. (2.21) over all available atom states at energy ϵ_0 to obtain the the diffusion coefficient D_ϵ as a function of energy only. For simplicity of notation, let us introduce re-scaled forms of the diffusion coefficient $D(\epsilon)$ and time t.

$$\mathcal{D}_\epsilon = \tfrac{D_\epsilon}{(n\bar{v}b^2)} \quad , \quad \tau = t(n\bar{v}b^2)$$

τ is the number of collision times in time t. Finally,

$$\mathcal{D}_\epsilon = 2\sqrt{2\pi}\chi\frac{\int \hat{p}_\phi\hat{\omega}_\phi^2\mathcal{F}\left(\frac{\omega_\phi\rho_{\min}}{\bar{v}}\right)\delta(\epsilon-\epsilon_0)\,d\!p_\phi dI_z}{\int\delta(\epsilon-\epsilon_0)\,d\!p_\phi dI_z}. \tag{2.23}$$

We may extract the diffusion coefficient $\mathcal{D}_\epsilon$ from the simulation results as well. Recalling that the final distribution in the simulation is proportional to $w(\epsilon, \epsilon')$, we can use Eq. (2.11), letting $w(\epsilon, \epsilon')$ be the appropriately weighted distribution from only those collisions with impact parameter above $\rho_{\min}$ and extending $\delta\epsilon$ to ∞. The integral becomes the following discrete sum:

$$\mathcal{D}_\epsilon = \sqrt{2\pi}\left[\left(\frac{10}{\epsilon}\right)^2 - \hat{\rho}_{\min}^2\right]\frac{1}{N}\sum_{i=1}^{N}\Delta\hat{p}_\phi^2. \tag{2.24}$$

The impact area considered for purposes of calculating $\mathcal{D}_\epsilon$ lies outside the cutoff radius but within a disk of radius $10/\epsilon$. Since the simulation samples all possible atom initial conditions at a fixed binding energy, the average over all accessible atomic states (for a given ϵ) is included in the sum above.

In Fig. 2.3, simulation and theory for $\mathcal{D}_\epsilon$ agree over a range of binding energies before the chaotic cutoff. As binding energy increases, ω_ϕ increases and eventually exceeds the inverse collision time $\bar{v}/\rho_{\min}$. An exponential decrease in $\mathcal{D}_\epsilon$ is observed as p_ϕ becomes adiabatically invariant on the collision timescale. At deep binding, cyclotron motion becomes relevant and the theory expression Eq. (2.23), derived using the $\vec{E} \times \vec{B}$ drift approximation, no longer applies. The adiabatic invariance of I_z is confirmed a posteriori by agreement between theory and simulation at mid-range energies.

2.4 Mean Rate of Energy Loss

We now calculate the mean rate at which energy is lost by an ensemble of guiding-center atoms at an initial binding energy ϵ. We first consider the effect

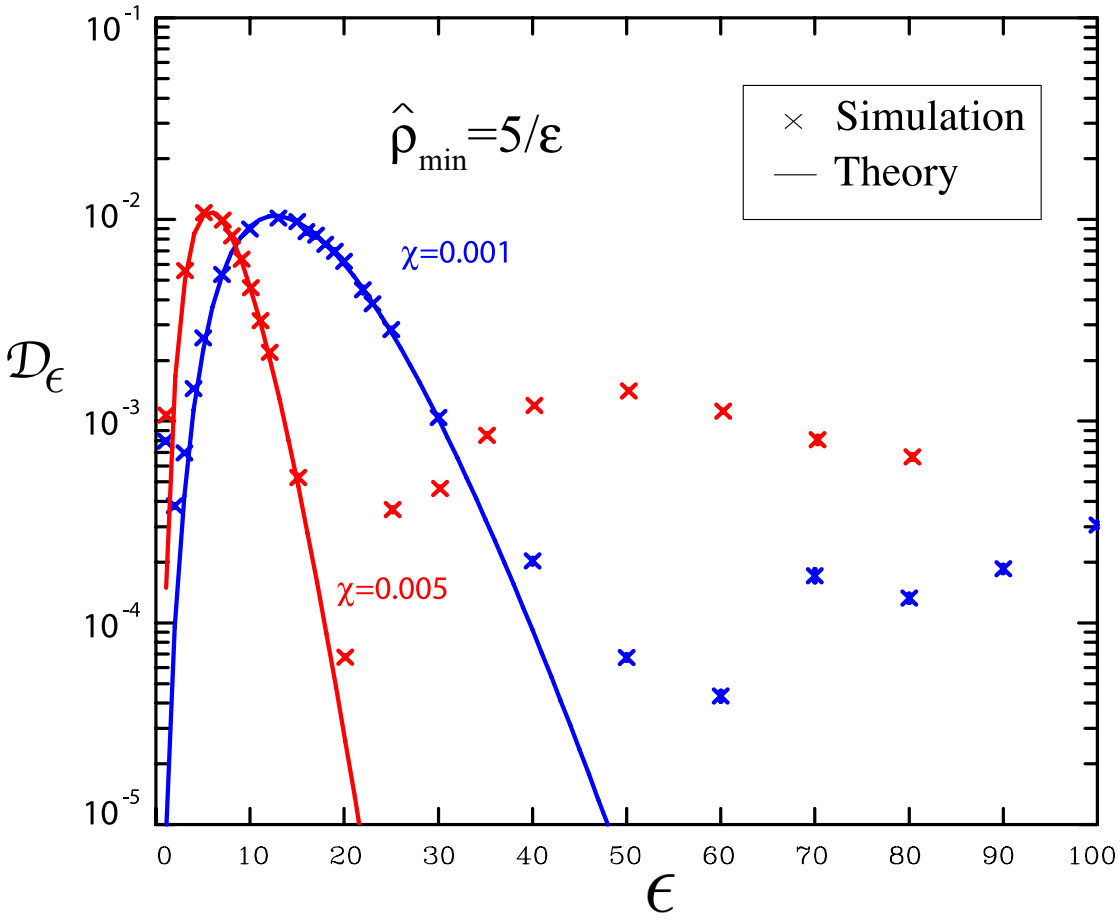

Figure 2.3: Theory and simulation for the diffusion coefficient $\mathcal{D}_\epsilon$ from collisions with impact parameter greater than $\hat{\rho}_{\min} = 5/\epsilon$ at $\chi = 0.001$ and $\chi = 0.005$. The theory assumes guiding-center drift motion with adiabatic invariance of I_z. At deep binding energies ϵ, the $\vec{E} \times \vec{B}$ drift approximation becomes invalid as the atom passes into the chaotic regime and the theory fails.

due to diffusion and mobility caused by large impact parameter collisions using the Fokker-Planck flux in ϵ of Eq. (2.15) and the theoretical expression for $\mathcal{D}_\epsilon$ in Eq. (2.23). We then include collisions with all impact parameters. As no adequate theory exists for small impact parameters, this contribution comes from the simulation only. The large-impact-paramter energy-loss rate is then confirmed with a direct calculation of the drag exerted by a collisionless positron plasma on a guiding-center atom's internal drift motion.

2.4.1 Collisional energy loss

Consider an ensemble $f(\epsilon)$ of atoms distributed in energy ϵ. The average binding energy ϵ is

$$\bar{\epsilon} = \frac{\int \epsilon' f(\epsilon')\, d\epsilon'}{\int f(\epsilon')\, d\epsilon'}. \tag{2.25}$$

The energy-loss rate follows.

$$\frac{\partial \bar{\epsilon}}{\partial t} = \frac{\int \epsilon' \frac{\partial f}{\partial t} d\epsilon'}{\int f(\epsilon')\, d\epsilon'} \tag{2.26}$$

The continuity equation,

$$\frac{\partial f}{\partial t} = -\frac{\partial \Gamma_{\epsilon'}}{\partial \epsilon'}, \tag{2.27}$$

combined with Eq. (2.15), closes the system. Choosing $f(\epsilon') = \delta(\epsilon' - \epsilon)$ gives the energy-loss rate $\partial\bar{\epsilon}/\partial t|_{\text{drag}}$ due to large impact parameter collisions at energy ϵ. Integrating by parts twice:

$$\left.\frac{\partial \bar{\epsilon}}{\partial t}\right|_{\text{drag}} = \int \left(M_\epsilon + \frac{\partial D_\epsilon}{\partial \epsilon'} \right) \delta(\epsilon' - \epsilon)\, d\epsilon'.$$

The Einstein relation Eq. (2.13) gives the mobility coefficient M_ϵ. In our dimensionless variables, the energy-loss rate due to drag is

$$\left.\frac{\partial\bar{\epsilon}}{\partial\tau}\right|_{\rm drag} = \mathcal{D}_\epsilon \frac{\partial f_{\rm th}/\partial\epsilon}{f_{\rm th}(\epsilon)} + \frac{\partial\mathcal{D}_\epsilon}{\partial\epsilon}. \tag{2.28}$$

The first term in the numerator of Eq. (2.28) arose from the first term in Eq. (2.15), and thus represents energy loss due to mobility flux. This term is positive definite as one would expect. The second term arises from the second term in Eq. (2.15), representing change in binding energy due to diffusive spreading. The second, diffusive term can be positive or negative, as seen in Fig. 2.3.

A procedure similar to that leading to Eq. (2.24) gives $\partial\bar{\epsilon}/\partial\tau|_{\rm drag}$ from the simulation. This time we calculate the first moment of $w(\epsilon,\epsilon')$.

$$\frac{\partial\epsilon}{\partial\tau} = \sqrt{2\pi}\left[\left(\frac{10}{\epsilon}\right)^2 - \hat{\rho}_{\rm min}^2\right]\frac{1}{N}\sum_{i=1}^{N}\Delta\epsilon_i. \tag{2.29}$$

Again, only collisions beyond a disc of radius $\hat{\rho}_{\rm min}$ and within a radius of $10/\epsilon$, the maximum considered in the simulation, are considered in the sum.

Eq. (2.28) and Eq. (2.29) give the mean energy-loss rate due to collisions outside the cutoff radius $\rho_{\rm min}$ as a function of the binding energy ϵ. The minimum impact parameter $\rho_{\rm min}$ can be chosen arbitrarily, as long as it satisfies $\hat{r}_{\rm min} >> \epsilon^{-1}$. Figure 2.4 shows the energy-loss rate from Eq. (2.28) compared with the same rate obtained from the Monte-Carlo simulation. The loss rate from large-impact-parameter collisions peaks when the atomic drift velocity equals the thermal velocity. Using the small-bounce form of $\hat{\omega}_\phi$ from Eq. (1.17), the energy $\epsilon_{\rm peak}$ where

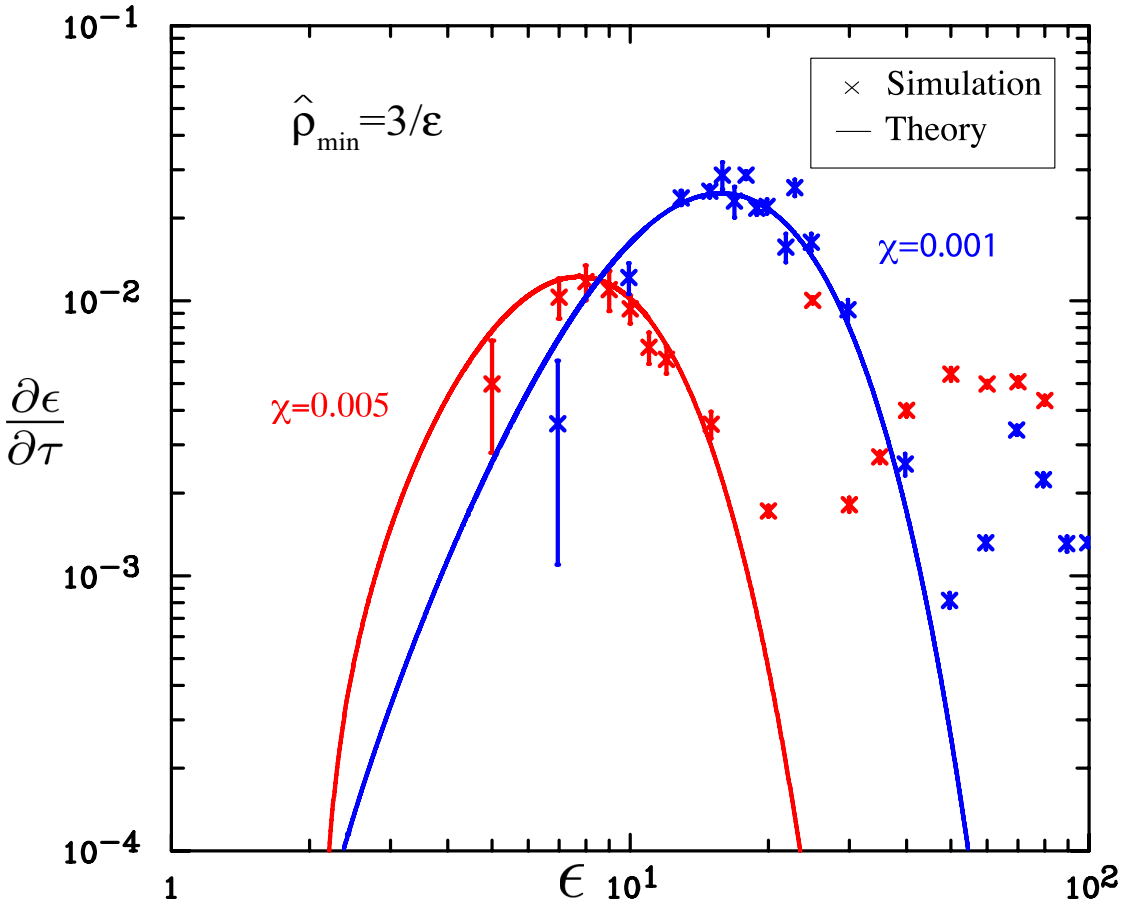

Figure 2.4: The energy-loss rate due to large impact parameter collisions ($\rho_p > \rho_{\min} = 3/\epsilon$) for $\chi = 0.001$ and $\chi = 0.005$. The theory lines come from Eq. (2.28). The exponential cutoff is observed in the simulation results until we near the chaotic cutoff energy ($\epsilon_c = 100$ and $\epsilon_c = 34.2$ for $\chi = 0.001$ and $\chi = 0.005$ respectively). Here, the drift approximation used in deriving the transport coefficient D_ϵ is invalid.

collisional drag peaks is given by:

$$\epsilon_{\text{peak}} = \chi^{-1/2}. \tag{2.30}$$

After this point, the drift motion becomes adiabatically decoupled from the plasma, causing an order of magnitude reduction in the rate, as expected from guiding-center theory. However, at larger energies where $\epsilon \gtrsim \chi^{-2/3}$, the atom enters the chaotic regime where guiding-center theory no longer applies. Here, the energy-loss rate no longer follows the theoretical rate. This is because, for $\epsilon \approx \chi^{-2/3}$, the timescale of rotational motion of the positron about the antiproton is set by the cyclotron frequency and is roughly independent of ϵ. At still larger values of ϵ, $\epsilon >> \chi^{-2/3}$, the atom becomes effectively unmagnetized and we would again expect a reduction in the loss rate with increasing ϵ. However, we have not studied this unmagnetized regime in detail. For $\chi = 0.001$, it would require $\epsilon >> 100$.

Fig. 2.5 shows the energy-loss rate due to all collisions. The simulation gives the contribution from impact parameters $\hat{\rho}$ below $10/\epsilon$ (through Eq. (2.29) with $\rho_{\text{min}} = 0$). The theory gives the (small) contribution for all larger impact parameters. For the infinite-magnetic-field ($\chi = 0$) case, there is no $\vec{E} \times \vec{B}$ drift motion on which large-impact-parameter collisions can drag, so energy loss occurs primarily from close collisions. The energy-loss rate from this process scales as follows:

$$\left\langle \frac{\partial \epsilon}{\partial \tau} \right\rangle \approx \overline{\Delta\epsilon} \frac{\nu_{\text{close}}}{n\overline{v}b^2},$$

where ν_{close} is the effective frequency of close collisions and $\overline{\Delta\epsilon}$ is the average size

of the energy step taken. In a collision with a deeply bound atom, the initial thermal velocity of the free positron is negligible. The average energy step is then proportional to the binding energy.

$$\overline{\Delta\epsilon} \propto \epsilon$$

The frequency of close collisions scales with the atom size:

$$\nu_{\text{close}} \propto \frac{n\bar{v}b^2}{\epsilon^2}.$$

The average energy-loss rate from such collisions is thus proportional to the inverse of binding energy.

$$\left\langle \frac{\partial\epsilon}{\partial\tau} \right\rangle \propto \frac{1}{\epsilon}$$

The dashed line in Fig. 2.5 shows this scaling, which is followed well in the $\chi = 0$ case. When the magnetic field is finite, energy loss from collisions with impact parameter larger than the atom remains relevant even at deep binding (as seen in Fig. 2.4). In this case, the total collisional energy-loss rate does not drop as rapidly as the binding energy increases.

For small values of χ, the infinite-magnetic-field scaling is followed until collisional drag on $\vec{E} \times \vec{B}$ drift motion begins to become important. The location ϵ_{peak} of the peak in collisional drag is proportional to $\chi^{-1/2}$ (from Eq. (2.30)), so the energy at which this effect becomes evident in Fig. 2.5 scales the same way.

At binding energies ϵ below 4, the average energy-loss rate $\langle\partial\epsilon/\partial\tau\rangle$ is negative. At such shallow binding, an atom is more likely to become re-ionized by

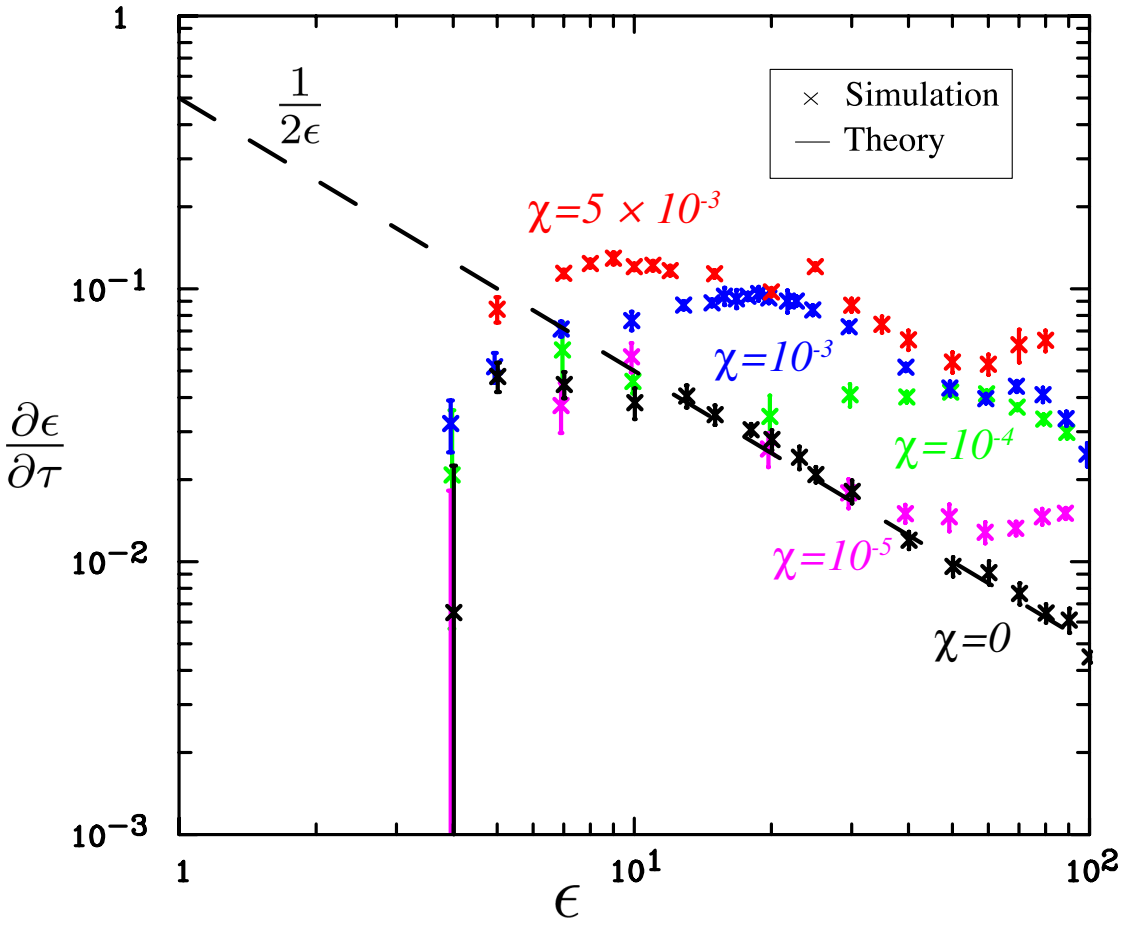

Figure 2.5: The total collisional energy-loss rate for $\chi = 0$, 10^{-5}, 10^{-4}, 10^{-3}, and 5×10^{-3}. The rate is obtained by adding the simulation contribution for impact parameters below $10/\epsilon$ (from Eq. (2.29) with $\rho_{\rm min} = 0$) to the theory for larger impact parameters (Eq. (2.28) with $\rho_{\rm min} = 10$). Long-range collisions are irrelevant in the $\chi = 0$ case, where the only drag is on rapid, adiabatically decoupled parallel bounce motion. In this case, dimensional arguments suggest $1/\epsilon$ scaling in $\partial\epsilon/\partial\tau$ (see text).

collisions than to cascade to deeper binding energy. For this reason $\epsilon = 4$ is referred to as the kinetic bottleneck [7]. At $\epsilon < 4$, the bound positron's average velocity along the magnetic field is less than the thermal velocity $\bar{v}$. A free streaming positron is more likely to impart energy to the atom orbit (decrease ϵ) than to carry it away (increase ϵ). At deeper binding, the reverse is true and most collisions cause a step to deeper binding. If an atom makes it to $\epsilon > 4$, it is more likely to cascade to deep binding than to become re-ionized.

We use the total energy-loss rate, linearly interpolated between the points shown in Fig. 2.5, to estimate the number of collision times τ required for an average atom to cascade from $\epsilon = 5$ to $\epsilon = 100$ at different values of the magnetic parameter χ. The results in Table 2.4 show higher cascade times at higher magnetic fields (lower χ). All cascades exceed 1000 collision times, much longer than a typical atomic trapping time. However, the cascade of an ensemble of atoms, considered in the next chapter, reveals a tail of atoms that reach deep binding at early times despite the low average energy-loss rate.

2.4.2 Direct plasma drag energy loss

The energy-loss rate from long-range collisions can also be calculated directly from plasma drag. The bound positron's orbital motion excites a wake in the plasma, which in turn exerts an electric force back on the atom. We calculate the drag force here by way of the collisionless Vlasov equation, then evaluate the work done on the atom. The resulting energy-loss rate is equal to the Fokker-

Planck rate calculated above. By remodeling binary atom-positron interactions with collective plasma oscillations, we offer a confirmation of the theory of energy loss from large-impact-parameter collisions. In the analysis we will use plasma (breve $\breve{}$) units rescaled by

$$\begin{aligned} \omega_p &= \sqrt{\tfrac{4\pi e^2 n}{m_e}} \qquad \text{for frequency} \\ \text{and} \quad \lambda_D &= \tfrac{\bar{v}}{\omega_p} \qquad\quad \text{for length.} \end{aligned} \tag{2.31}$$

Any time-varying charge distribution, including a guiding-center atom, will excite a plasma response. The work done on the charge by the plasma response is given by

$$\frac{\partial \epsilon}{\partial t} = -\frac{1}{k_B T} \int d^3x \vec{J}_{\text{atm}}(\vec{x}, t) \cdot \vec{E}_p(\vec{x}, t) \tag{2.32}$$

where $\vec{J}_{\text{atm}}$ is the current density associated with the charge distribution (the guiding-center atom in this case), and $\vec{E}_p$ is the electric field due to the plasma response. Let us introduce time and space Fourier transforms for periodic motion of angular frequency ω defined by

$$f(t) = \sum_{m=-\infty}^{\infty} \tilde{f}^{(m)} e^{-im\omega t} \tag{2.33}$$

$$\tilde{f}^{(m)} = \frac{\omega}{2\pi} \int_0^{\frac{2\pi}{\omega}} f(t) e^{im\omega t} dt \tag{2.34}$$

and

$$f(\vec{x}) = \frac{1}{(2\pi)^3} \int \tilde{f}(\vec{k}) e^{i\vec{k}\cdot\vec{x}} d^3k \tag{2.35}$$

$$\tilde{f}(\vec{k}) = \int f(\vec{x}) e^{-i\vec{k}\cdot\vec{x}} d^3x. \tag{2.36}$$

In a guiding-center atom, the oscillation frequency ω is identified with the drift frequency ω_ϕ, the slowest characteristic frequency of the atom.

Now Eq. (2.32) can be recast in Fourier space using Parceval's relation [27]:

$$\frac{\partial \epsilon}{\partial t}(t) = -\frac{1}{(2\pi)^3 k_B T} \Re \left(\int \tilde{\vec{J}}_{\rm atm}(-\vec{k}, t) \cdot \tilde{\vec{E}}_p(\vec{k}, t) d^3k \right). \tag{2.37}$$

Taking the real part in the expression above is not strictly necessary since it is already assured to be real. However, since imaginary factors must go to zero upon integration, we may as well discard them before we integrate. Note that Eq. (2.37) is only transformed in space, not time.

If $\tilde{\phi}^{(m)}_{\rm atm}(\vec{k}, \omega)$ is the Fourier transformed electrostatic potential due to the atom (or other generalized charge distribution), then we can write the transformed potential $\tilde{\phi}^{(m)}_p$ due to plasma excitations as

$$\tilde{\phi}^{(m)}_p(\vec{k}) = \eta^{(m)} \tilde{\phi}^{(m)}_{\rm atm}(\vec{k}).$$

The plasma response coefficient $\eta^{(m)}(\vec{k}, \omega)$ will be determined with kinetic theory. Let $\tilde{\psi}^{(m)}$ be the Fourier transform of the atom's charge distribution $\psi(\vec{x}, t)$. In Fourier space we have

$$\tilde{\vec{E}}^{(m)}_p = -i\vec{k}\tilde{\phi}^{(m)}_p(\vec{k}) \tag{2.38}$$

$$k^2 \tilde{\phi}^{(m)}_{\rm atm}(\vec{k}) = 4\pi \tilde{\psi}^{(m)}(\vec{k}) \tag{2.39}$$

$$\vec{k} \cdot \tilde{\vec{J}}^{(m)}_{\rm atm}(\vec{k}) = m\omega \tilde{\psi}^{(m)}(\vec{k}). \tag{2.40}$$

Equation (2.39) is Poisson's equation and (2.40) is the equation of charge conservation. Expressing $\tilde{\vec{E}}_p(\vec{k}, t)$ and $\tilde{\vec{J}}_{\rm atm}(\vec{k}, t)$ in terms of the inverse Fourier transform Eq. (2.33) and using Eqs. (2.38) and (2.39), Eq. (2.37) can be rewritten

$$\frac{\partial \epsilon}{\partial t} = \frac{2}{(2\pi)^2 k_B T} \Re \left[\int \frac{i\eta^{(m)}}{k^2} \sum_{m=-\infty}^{\infty} \left(\tilde{\psi}^{(m)}(\vec{k}) e^{-im\omega t} \right) \right.$$

$$\vec{k} \cdot \sum_{l=-\infty}^{\infty} \left(\tilde{\vec{J}}^{(l)}_{\rm atm}(-\vec{k}) e^{-il\omega t} \right) d^3k \Bigg] .$$

Substituting with Eq. (2.40) we get

$$\frac{\partial \epsilon}{\partial t} = -\frac{2\omega}{(2\pi)^2 k_B T} \sum_{l,m} \Re \int \frac{i\eta^{(m)}}{k^2} l e^{-i(l+m)\omega t} \tilde{\psi}^{(l)}(\vec{k}) \tilde{\psi}^{(m)}(-\vec{k}) d^3k.$$

A time average defined by $\langle f \rangle = \frac{\omega}{2\pi} \int_0^{2\pi/\omega} f(t) dt$ converts the exponential factor into $\delta_{l,-m}$, leaving

$$\left\langle \frac{\partial \epsilon}{\partial t} \right\rangle = \frac{2\omega}{(2\pi)^2 k_B T} \sum_m m \Re \int \frac{i\eta^{(m)}}{k^2} \tilde{\psi}^{(m)}(\vec{k}) \tilde{\psi}^{(-m)}(-\vec{k}) d^3k. \tag{2.41}$$

Since $\tilde{\psi}^{(m)}(\vec{k}) \tilde{\psi}^{(-m)}(-\vec{k}) = \tilde{\psi}^{(m)*} \tilde{\psi}^{(m)}$ is real, Eq. (2.41) simplifies to

$$\left\langle \frac{\partial \epsilon}{\partial t} \right\rangle = -\frac{2\omega}{(2\pi)^2 k_B T} \sum_{m=-\infty}^{\infty} m \int \frac{\Im \eta^{(m)}}{k^2} \tilde{\psi}^{(m)*} \tilde{\psi}^{(m)} d^3k. \tag{2.42}$$

Here and henceforth explicit dependence on $\vec{k}$ is omitted.

The coefficient $\eta^{(m)}$ in Eq. (2.42) determines how strongly the plasma responds to driving at frequency ω and wave vector $\vec{k}$. Langmuir waves appear as a resonance in $\eta^{(m)}$ along the solution to the dispersion relation

$$\omega^2 \approx \omega_p^2 \cos^2\theta \left[1 + 3 \left(\frac{k\bar{v}}{\omega_p} \right)^2 \right]. \tag{2.43}$$

In the wave regime where $k\lambda_D << 1$, the response is lightly damped and the resonance is nearly a δ-function. At higher values of k, the wavelength is shorter than the Debeye shielding length $\lambda_D = \bar{v}/\omega_p$ and the heavily damped response will be non-wavelike. Eq. (2.42) indicates that only $\Im \eta^{(m)}$ contributes to de-excitation of the atom. After $\eta^{(m)}$ is calculated, the integrand in Eq. (2.42) will be evaluated

to determine the relative importance of contributions at different wave vectors $\vec{k}$. In particular, we will find that the heavily damped, non-wavelike regime contributes far more than the Langmuir wave regime. Thus, most energy is radiated into the plasma through a broad spectrum of short wavelength oscillations. Physically, these oscillations amount to a Fourier space description of the two-body interactions that give rise to collisional drag.

To find $\eta^{(m)}$, we consider oscillations excited by a time dependent charge distribution $\psi(\vec{x},t)$. In the strong-magnetic-field limit, we can neglect perturbations in the transverse velocity. To further simplify the calculation, we discard any effect due to collisions between plasma positrons. Additionally, the plasma is assumed to extend infinitely in all directions and standing waves are thus precluded. With these approximations, the linearized Vlasov equation for the positron plasma takes the form

$$\frac{\partial \delta f}{\partial t} + v_z \frac{\partial \delta f}{\partial z} + \frac{eE_z}{m_e}\frac{\partial f}{\partial v_z} = 0.$$

Above, E_z refers to the total electric field including contributions from both the plasma oscillation and the atom. The perturbed distribution function is δf and $f = \frac{n}{\sqrt{2\pi}\bar{v}} e^{-v_z^2/2\bar{v}^2}$ is the unperturbed, thermal-equilibrium distribution function. In Fourier space, using Eq. (2.38), we have

$$m\omega \tilde{\delta f}^{(m)} + k_z v_z \tilde{\delta f}^{(m)} + \frac{ek_z \tilde{\phi}^{(m)}}{m_e}\frac{\partial f}{\partial v_z} = 0,$$

giving

$$\tilde{\delta f}^{(m)} = \frac{ek_z \tilde{\phi}^{(m)}}{m_e}\frac{\partial f/\partial v_z}{k_z v_z - m\omega}.$$

Here $\tilde{\phi}^{(m)} = \tilde{\phi}^{(m)}_{\rm atm} + \tilde{\phi}^{(m)}_p$ is the *total* electrostatic potential. Poisson's equation for the potential field $\tilde{\phi}^{(m)}_p$ due only to the plasma is

$$k^2 \tilde{\phi}^{(m)}_p = 4\pi e \int dv_z \tilde{\delta f}^{(m)}.$$

Thus

$$\tilde{\phi}^{(m)}_p = \alpha^{(m)} \tilde{\phi}^{(m)}, \tag{2.44}$$

where $\alpha^{(m)}$ is given by,

$$\alpha^{(m)} \equiv \frac{\omega_p^2}{nk^2} \int dv_z \frac{\partial \hat{f}/\partial v_z}{v_z - m\omega/k_z} \tag{2.45}$$

Finally,

$$\begin{aligned} \tilde{\phi}^{(m)}_p &= \alpha^{(m)} \tilde{\phi}^{(m)} = \alpha^{(m)} \left(\tilde{\phi}^{(m)}_p + \tilde{\phi}^{(m)}_{\rm atm} \right) \\ \Longrightarrow \tilde{\phi}^{(m)}_p &= \frac{\alpha^{(m)}}{1 - \alpha^{(m)}} \tilde{\phi}^{(m)}_{\rm atm} \end{aligned}$$

and

$$\eta^{(m)} = \frac{\alpha^{(m)}}{1 - \alpha^{(m)}}. \tag{2.46}$$

A careful contour integral in Eq. (2.45) gives $\alpha^{(m)}$. Let us introduce scaled variables $\breve{k} = k\lambda_D$ and $\breve{\omega} = \omega/\omega_p$. In these variables

$$\alpha^{(m)} = -\frac{1}{\breve{k}^2} \left[1 + \frac{m\breve{\omega}}{\sqrt{2}\left|\breve{k}_z\right|} e^{-m^2\breve{\omega}^2/2\breve{k}_z^2} \left(i\pi^{1/2} - 2\int_0^{\frac{m\breve{\omega}}{\sqrt{2}|\breve{k}_z|}} e^{t^2} dt \right) \right]. \tag{2.47}$$

In general, we can only evaluate Eq. (2.47) numerically. Fig. 2.6 shows a numerical evaluation of $\Im\eta^{(1)}$ versus θ (the angle of $\vec{k}$ with the magnetic field), at two values of $\breve{k}$. Note how a clean resonance at small $\breve{k}$ broadens to a non-wavelike response

Table 2.4: The number of collision times τ required for an average atom to cascade from $\epsilon = 5$ (just past the kinetic bottleneck) to $\epsilon = 100$. The magnetic parameter $\chi = r_c/b$; a smaller value indicates a stronger magnetic field. As field strength decreases, so does cascade time. An average atom takes well over 1000 collision times, much longer than typical atom trapping times, to reach $\epsilon = 100$.

χ	0	10^{-5}	10^{-4}	10^{-3}	5×10^{-3}
τ	9660.	5065.	2575.	2070.	1349.

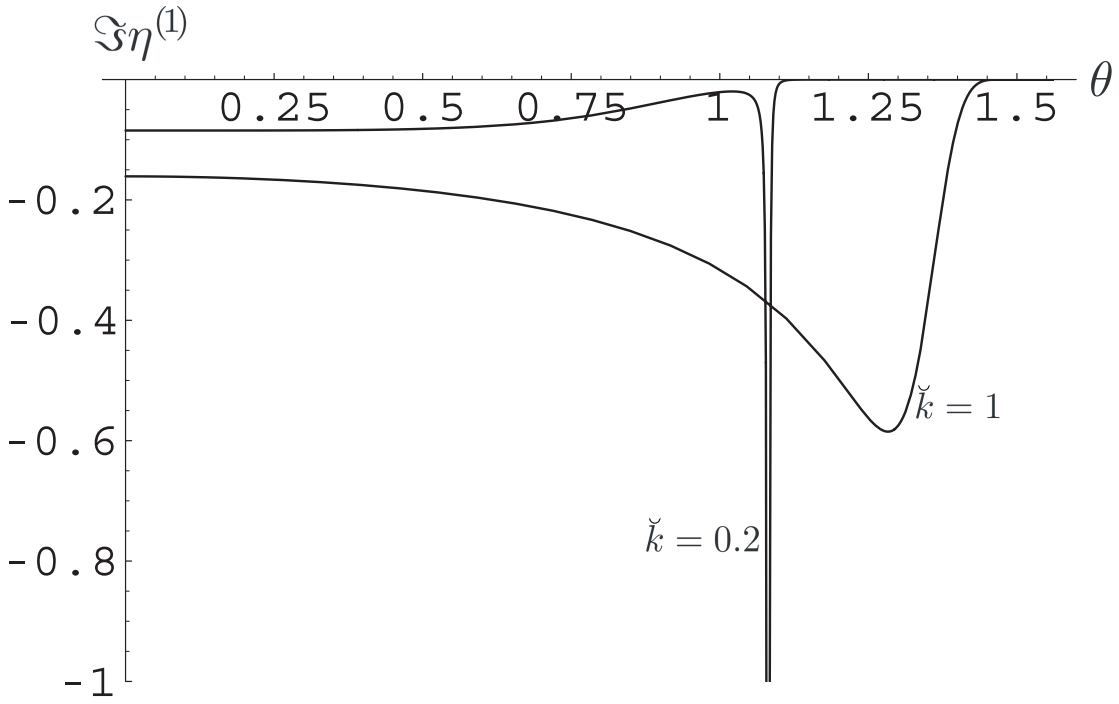

Figure 2.6: $\Im\eta^{(1)}$ (Eqs. (2.46) and (2.47)), the first time harmonic coefficient of the plasma response function, plotted against θ for two values of the normalized wave number $\breve{k} = k\lambda_D$ with the normalized drift frequency $\breve{\omega} = \omega/\omega_p = 0.5$. As $\breve{k}$ increases, the response coefficient drops off like $\breve{k}^{-3}$ and the resonance broadens. The $\breve{k} = 0.2$ resonant peak has a height of -70 (off graph range) and is located as predicted by the fluid Langmuir wave dispersion relation Eq. (2.43).

as $\breve{k}$ increases. A $\breve{k}^{-3}$ drop off governs $\Im\alpha^{(m)}$ and $\Im\eta^{(m)}$:

$$\Im\eta^{(m)} = \Im\frac{\alpha^{(m)}}{1-\alpha^{(m)}} \overset{\breve{k}>>1}{\approx} \Im\alpha^{(m)} \propto \frac{1}{\breve{k}^3}.$$

Thus the plasma tends to respond more strongly at small wave numbers, where damping is small. At small $\breve{k}$, $\eta^{(1)}$ is resonant when $\Re\alpha^{(1)} = 1$ (where the denominator nearly vanishes). Fig. 2.7 shows this condition plotted with the Langmuir dispersion relation, Eq. (2.43). For small values of $\breve{k}$,

$$\Re\alpha^{(1)} \overset{\breve{k}<<1}{\approx} \frac{\omega_p^2}{\omega^2}\cos^2\theta\left[1+3\left(\frac{k\bar{v}}{\omega_p}\right)^2\right] = 1$$

and Eq. (2.43) is recovered.

We will examine here the simple case where the guiding-center atom has zero bounce amplitude. This approximation is justified by the fact that the energy-loss rate drops exponentially at high oscillation frequencies. Because the bounce frequency $\omega_z >> \omega_\phi$ in guiding-center atoms, bounce motion is adiabatically decoupled from the plasma and we choose to neglect its exponentially small effect on the energy loss. The guiding-center atom of Fig. 1.1, without bounce motion, is described by the time dependent charge distribution

$$\psi(\vec{x},t) = e\left[-\delta\left(\vec{x}\right) + \delta\left(\vec{x} - r(\cos\omega_\phi t\hat{\vec{i}} + \sin\omega_\phi t\hat{\vec{j}})\right)\right].$$

Applying Eqs. (2.34) and (2.36) and shifting to normalized coordinates,

$$\tilde{\breve{\psi}}^{(m)}(\breve{\vec{k}}) = e\left[-\delta_{m,0} + e^{im\phi}i^m J_m(\breve{k}_\perp\breve{r})\right].$$

Above, the angle ϕ is the azimuthal angle with the magnetic field along z; J_m is the mth Bessel function of the first kind and $\breve{r} = r/\lambda_D$ is the normalized atom

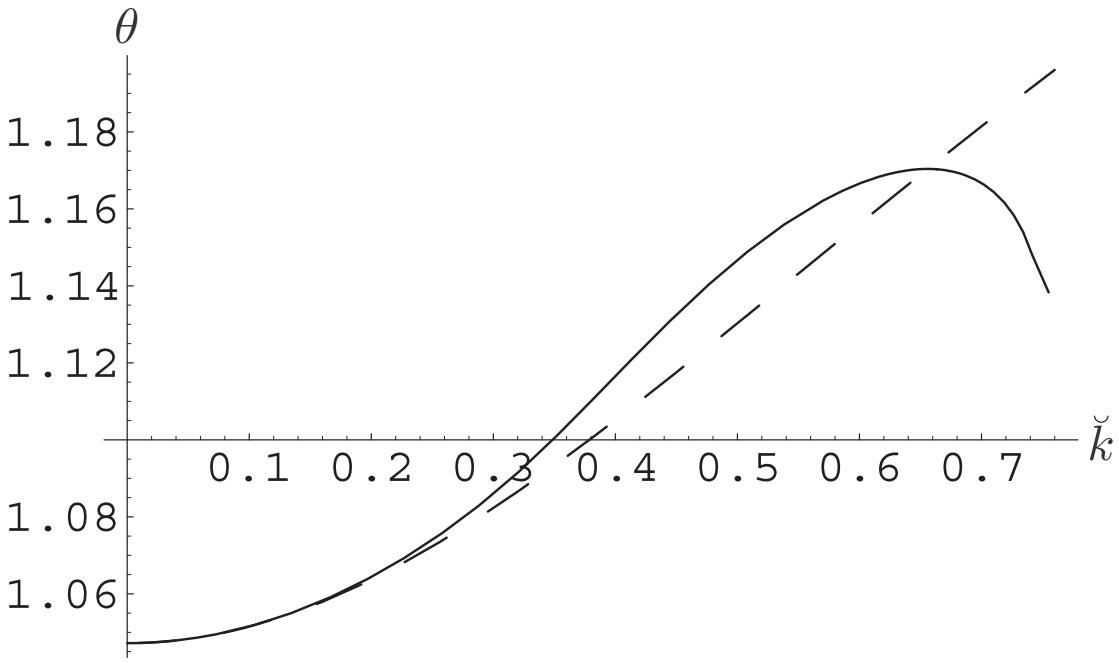

Figure 2.7: The predicted resonant angle θ at a value of $\breve{\omega} = 0.5$. The solid curve plots a solution to $\Re\alpha^{(1)} = 1$. The dashed curve gives the Langmuir wave dispersion relation Eq. (2.43). On the solid curve, the bottom part of the "thumb" diagram, giving the dispersion for the strongly-damped electron acoustic wave, is omitted.

radius (a small parameter). We can discard the zero frequency $m = 0$ case because it doesn't contribute to the damping process.

$$\tilde{\psi}^{(m)*}\tilde{\psi}^{(m)} = e^2 J_m^2(\breve{k}_\perp \breve{r}) \;\; ; \;\; m \neq 0. \tag{2.48}$$

With Eq. (2.42) (recast in normalized coordinates) combined with Eqs. (2.46), (2.47), and (2.48), we are equipped to numerically evaluate the energy loss rate. In practice, we must limit the scope of the integral in Eq. (2.42) to exclude close collisions. In the present plasma wake model, this is accomplished by restricting the wave number to the region $\breve{k} < 1/\breve{r}$. In spherical coordinates,

$$\left\langle \frac{\partial \epsilon}{\partial t} \right\rangle = -\frac{2e^2\omega_\phi}{(2\pi)^2 k_B T \lambda_D} \times \sum_{m=-\infty}^{\infty} m \int_0^{1/\breve{r}} \int_0^{\pi} \int_0^{2\pi} d\phi d\theta d\hat{k} \sin\theta \Im\eta^{(m)} J_n^2(\breve{k}\breve{r}\sin\theta). \tag{2.49}$$

Performing the ϕ integral,

$$\left\langle \frac{\partial \epsilon}{\partial t} \right\rangle = -\frac{b}{\lambda_D}\frac{\omega_\phi}{\pi} \sum_{m=-\infty}^{\infty} n \int_0^{1/\breve{r}} \int_0^{\pi} d\theta d\breve{k} \sin\theta \Im\eta^{(m)} J_m^2(\breve{k}\breve{r}\sin\theta). \tag{2.50}$$

Fig. 2.8 shows the integrand of Eq. (2.50) plotted against wave propagation angle θ at some values of $\breve{k}$. This figure suggests that the non-wavelike, large-wave-number perturbations are more significant for atom recombination than resonant, small-wave-number Langmuir waves are. The high-$\breve{k}$ perturbations propagate nearly perpendicular to the magnetic field, creating transverse electric fields that drag on the bound positron's drift motion. For an estimate of the relative contributions from the wavelike and non-wavelike responses, assume that the small-$\breve{k}$ resonance in $\Im\eta^{(1)}$ can be approximated with a δ-function in θ. Using the Plemelj

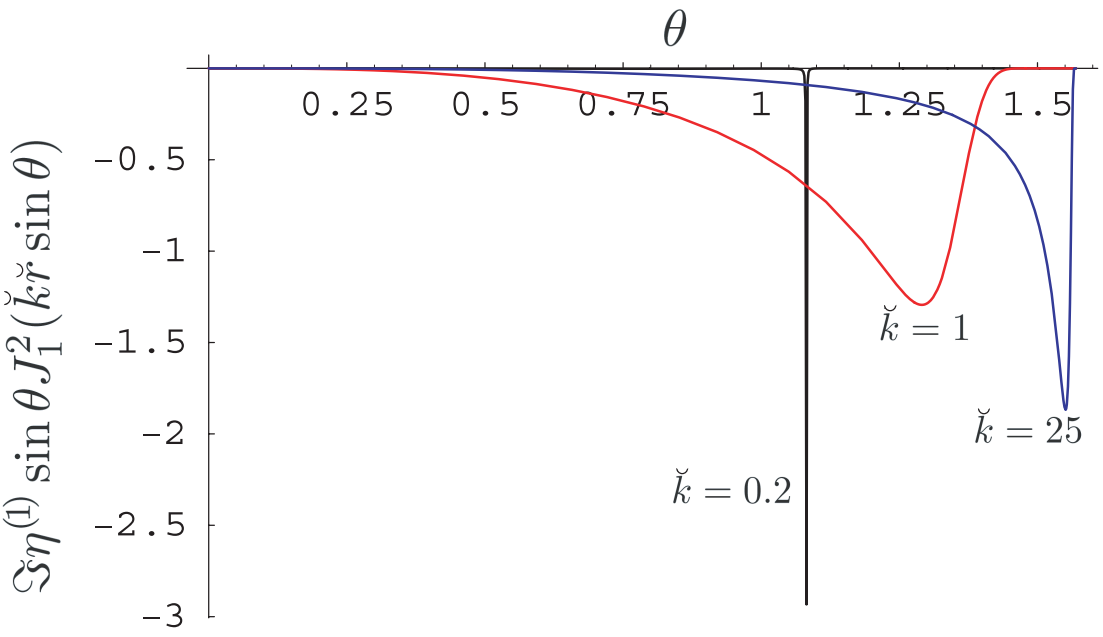

Figure 2.8: The $m = 1$ term of the integrand in Eq. (2.50) versus θ at several values of $\breve{k}$. Here, $\breve{\omega} = 0.5$ and the normalized atom radius $\breve{r} = r/\lambda_D = 1/100$. The area under the curve is small in the resonant wave regime (small $\breve{k}$). At larger wave numbers, most contribution to the integral comes from the region near $\theta = \pi/2$. Disturbances propagating nearly perpendicular to the magnetic field contribute most strongly to atomic relaxation.

formula, we approximate $\Im\eta^{(1)}$: [27]

$$\begin{aligned}\Im\eta^{(1)} &= \frac{\Im\alpha^{(1)}}{(\Re\alpha^{(1)}-1)^2+(\Im\alpha^{(1)})^2} \\ &\approx \pi\delta(\Re\alpha^{(1)}-1). \end{aligned} \tag{2.51}$$

We see that the area under the resonance (in θ space) is proportional to $(\partial\Re\alpha^{(1)}/\partial\theta)^{-1}$ evaluated on resonance. This factor is of order unity. When $\breve{k} << 1/\breve{r}$, we can write

$$J_1^2(\breve{k}\breve{r}\sin\theta) \overset{\breve{k}<\frac{1}{\breve{r}}}{\approx} \frac{1}{4}\breve{k}^2\breve{r}^2\sin^2\theta. \tag{2.52}$$

Thus the integrand for $m=1$ in the resonant wave region is proportional $\breve{k}^2$. Since the wave regime occupies a narrow range in $\breve{k}$ ($0<\breve{k}<\breve{k}_{min}\approx 1$), the contribution from this portion of the integral is small. Conversely, when $\breve{k} >> 1$, the response coefficient takes the form

$$\eta^{(m)} \overset{\breve{k}\geq 1}{\approx} -\sqrt{\frac{\pi}{2}}\frac{m\breve{\omega}}{\breve{k}^3\,|\cos\theta|}e^{-m^2\breve{\omega}^2/2\breve{k}^2\cos^2\theta}. \tag{2.53}$$

For sufficiently small $\breve{r}$, both Eqs. (2.52) and (2.53) are satisfied over a wide range of $\breve{k}$ ($\breve{k}_{min}<\breve{k}<1/\breve{r}$). This region dominates the integral in Eq. (2.50) and thus the recombination process. Fig. 2.9 shows the integrand in Eq. (2.50) numerically integrated over θ. The figure demonstrates how, for an atom much smaller than one Debeye length, the high-wave-number region overwhelmingly dominates the integral. The wavelength in this region is much smaller than the interparticle spacing, indicating that the process can only be accounted for by discreet positron interactions.

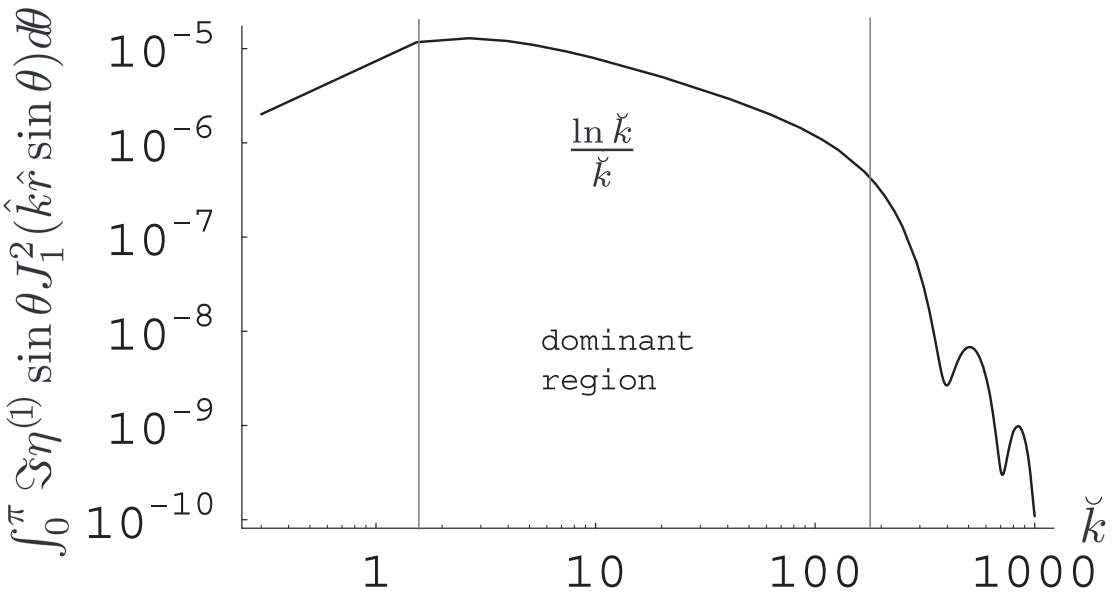

Figure 2.9: The $m = 1$ term of the integrand in Eq. (2.50) numerically integrated over θ ($\breve{\omega} = 0.5, \breve{r} = 1/100$). The integral of this function over $\breve{k}$ gives the atom's energy-loss rate due to large-impact-parameter collisions. The relative contribution from the weakly-damped, small-wave-number region becomes vanishingly small as $\breve{r}$ goes to zero. The recombination process is dominated by wave numbers above $\breve{k} = 1$, but below the cutoff $\breve{k} = 1/\breve{r}$. The upper cutoff appears naturally in the $m = 1$ case.

To find scaling, we apply Eq. (2.53) in the dominant region $\breve{k}_{min} < \breve{k} < 1/\breve{r}$:

$$\left\langle \frac{\partial \epsilon}{\partial t} \right\rangle = \frac{b}{\lambda_D \sqrt{2\pi}} \frac{\omega_\phi^2}{\omega_p} \int_{\breve{k}_{min}}^{1/\breve{r}} \int_0^\pi d\theta d\breve{k} \frac{\sin\theta}{\breve{k}^3 \left|\cos\theta\right|} \sum_{m=-\infty}^{\infty} m^2 e^{-m^2 \breve{\omega}^2 / 2\breve{k}^2 \cos^2\theta} J_n^2(\breve{k}\breve{r}\sin\theta).$$

In the finite range of integration, we can discard all but the $m = 1$ and $m = -1$ terms in the sum above. The higher order frequency harmonics represented by $|m| > 1$ are only important at wave numbers higher than $1/\breve{r}$. For the two remaining terms we can use Eq. (2.52) and $J_{-1}(x) = -J_1(x)$ to get

$$\left\langle \frac{\partial \epsilon}{\partial t} \right\rangle = \frac{1}{2\sqrt{2\pi}} \frac{\omega_\phi^2 \breve{r}^2}{\omega_p} \int_{\breve{k}_{min}}^{1/\breve{r}} \int_0^\pi d\theta d\breve{k} \frac{\sin^3\theta}{\breve{k}\left|\cos\theta\right|} e^{-\breve{\omega}^2/2\breve{k}^2\cos^2\theta}.$$

Let us shift to time $\tau = tn\bar{v}b^2$ normalized by one collision time. After the θ integral is performed analytically with $u = \breve{k}/\breve{\omega}$, we get

$$\frac{\partial \epsilon}{\partial \tau} = \sqrt{2\pi}\xi^2 \mathcal{G}(\xi), \tag{2.54}$$

where $\xi = \omega_\phi r/\bar{v}$ and

$$\mathcal{G}(\xi) = \int_{u_{\min}}^{1/\xi} \frac{du}{u} \left[-e^{-1/2u^2} + \left(1 + \frac{1}{2u^2}\right) \right] \Gamma_0 \left(\frac{1}{2u^2}\right). \tag{2.55}$$

We can ignore the lower integration limit $u_{\min} = \omega_p/\omega_\phi$ because its contribution is far outweighed by that of the upper bound (Fig. 2.9). The approximation $u_{\min} << 1/\xi$ is equivalent to $r << \lambda_D$, which is a prerequisite for binding to occur in the first place. Taking the limit of small drift frequency ($\xi << 1$), we get

$$\frac{\partial \epsilon}{\partial \tau} \approx \sqrt{2\pi}\xi^2 \log^2(\beta\xi). \tag{2.56}$$

When $\xi >> 1$, Eq. (2.54) takes the form

$$\frac{\partial \epsilon}{\partial \tau} \approx 4\sqrt{2\pi} \frac{e^{-\xi^2/2}}{\xi^2}. \tag{2.57}$$

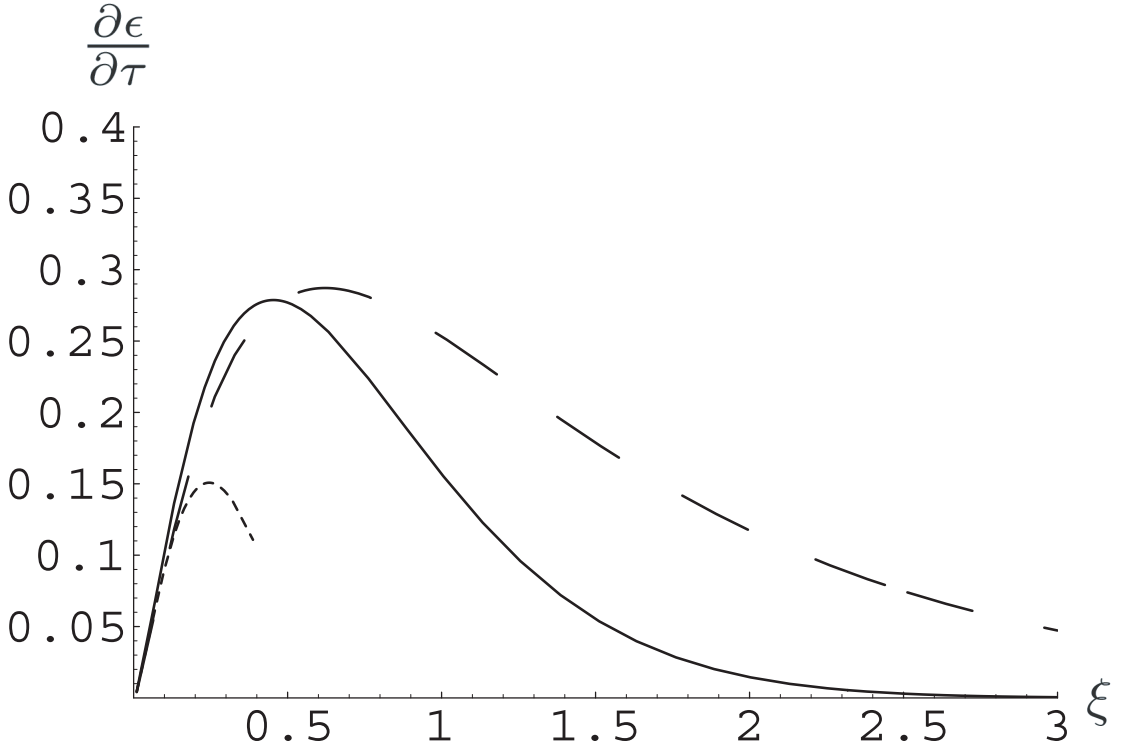

Figure 2.10: The normalized energy-loss rate plotted against the adiabaticity parameter $\xi = r\omega_\phi/\bar{v}$. The solid line comes from the present plasma wake calculation (Eq. (2.54)). The long-dashed line comes from the mobility calculation with a cut-off radius of $r_{min} = \beta r$ (chosen to bring the mobility result and Eq. (2.56) into agreement, see Section 2.4.1). At small ξ, both results take the limiting form of Eq. (2.56) (short-dashed curve).

The drift action becomes a good adiabatic invariant at high frequency and the energy-loss rate drops exponentially. The sensitivity of the high-adiabaticity result on the impact parameter cutoff suggests that, in this regime, close collisions become inseparable from collisional drag. Thus collisional drag is described well by the logarithmic approximation Eq. (2.56) for small adiabaticity, but when ξ exceeds unity the picture is more complicated. Medium-range collisions, which cannot be treated with the model presented here, become too important to neglect.

In Eq. (2.56), the small drift speed scaling of the energy-loss rate matches the simplified diffusive mobility result (Ref. [11]) except for the factor $\beta = e^{(1+\gamma)/2}/\sqrt{2} \approx 1.56$, where γ is Euler's constant, within the logarithm. This difference is unsurprising, because it depends on the choice of cutoff wavelength in the integral in Eq. (2.50). In the present calculation, the integral is over wave space. In the diffusive mobility calculation, the integral was over real space. The choice of $k_{\max} = 1/r$ is not precisely equivalent to placing a real space integral minimum at $r_{\min} = r$. Since both cutoff choices are arbitrary, one can shift either one by a factor of β to bring the two approaches into agreement (see Fig.2.10).

2.5 Transition Probability Rate Density from Distant Collisions

In addition to determining moments $\mathcal{D}_\epsilon$ and $\partial\epsilon/\partial\tau$ of the transition probability rate density $w(\epsilon, \epsilon')$ due to large-impact-parameter collisions, we can construct $w(\epsilon, \epsilon')$ directly. The energy step due to a large-impact-parameter collision

is, as above:

$$\Delta\epsilon = -2\hat{\omega}_\phi \sin(\phi) \left| \frac{\hat{\rho}_{\rm atm}\omega_\phi}{\hat{v}_z^2} \right| K_1\left(\left| \frac{\hat{\omega}_\phi \hat{\rho}_p}{\hat{v}_z} \right| \right). \tag{2.58}$$

The transition probability rate density $w(\epsilon, \epsilon')$ for these collisions is equal to the volume of phase space with atom energy ϵ before a collision and ϵ' after, appropriately weighted by the phase-space-local collision frequency. As is evident from Eq. (2.58), the initial conditions of the atom enter only through the atom cylindrical radius $\hat{\rho}_{\rm atm}$ and drift frequency ω_ϕ. All other variables, ($\hat{v}_z$, $\hat{\rho}_p$, and ϕ) describe the free particle's initial conditions. The rate $w(\epsilon, \epsilon')$ is obtained by an integral over both atom and free particle initial conditions, but let us first consider $\omega(\Delta\epsilon, \hat{\omega}_\phi, \hat{\rho}_{\rm atm})$, defined:

$$\omega(\Delta\epsilon_0, \hat{\omega}_\phi, \hat{\rho}_{\rm atm}) \equiv \frac{n\bar{v}b^2}{\sqrt{2\pi}} \int \delta(\Delta\epsilon - \Delta\epsilon_0) \, |\hat{v}| \, e^{-\hat{v}^2/2} \hat{\rho}_p d\hat{v} d\hat{\rho}_p d\phi. \tag{2.59}$$

An average of Eq. (2.59) over atom initial conditions at binding energy ϵ gives the transition probability rate density $w(\epsilon, \epsilon')$.

Integrating Eq. (2.59) over ϕ introduces a factor of $|\partial\Delta\epsilon/\partial\phi|$ into the denominator.

$$\omega(\Delta\epsilon_0, \hat{\omega}_\phi, \hat{\rho}_{\rm atm}) = \sqrt{\frac{2}{\pi}} n\bar{v}b^2 \int \frac{|\hat{v}| \, e^{-\hat{v}^2/2} \hat{\rho}_p d\hat{v} d\hat{\rho}_p}{\sqrt{4\hat{\omega}_\phi^2 \left| \frac{\hat{\rho}_{\rm atm}\hat{\omega}_\phi}{\hat{v}^2} \right| K_1^2\left(\left| \frac{\hat{\omega}_\phi \hat{\rho}_p}{\hat{v}} \right| \right) - \Delta\epsilon_0^2}}$$

We have picked up a factor of two because, for any allowed $\Delta\epsilon_0$, there are two values of ϕ satisfying $\Delta\epsilon = \Delta\epsilon_0$. A change of variables

$$x \;=\; \frac{\hat{\omega}_\phi \hat{\rho}_p}{\hat{v}} \quad , \quad y \;=\; \frac{\hat{v}^2 \Delta\epsilon_0}{2\hat{\omega}_\phi^2 \hat{\rho}_{\rm atm}}$$

gives the form below.

$$\omega(\Delta\epsilon_0, \hat{\omega}_\phi, \hat{\rho}_{\rm atm}) = 4\sqrt{\frac{2}{\pi}}\frac{\alpha^2}{\hat{\omega}_\phi^2}\int_{x_{\rm min}}^{x_{\rm max}}\int_{\beta/x^2}^{K_1(x)}\frac{xy^2e^{-\alpha x}dydx}{\sqrt{K_1^2(|x|)-y^2}} \tag{2.60}$$

Above,

$$\alpha \;=\; \tfrac{\hat{\omega}_\phi^2\hat{\rho}_{\rm atm}}{\Delta\epsilon_0} \quad \text{and} \quad \beta \;=\; \tfrac{1}{2}\tfrac{\hat{\rho}_{\rm min}^2}{\hat{\rho}_{\rm atm}}\Delta\epsilon_0.$$

The lower limit of integration in y reflects the minimum impact parameter considered ($\hat{\rho}_{\rm min}$). The upper limit, required to keep the denominator in Eq. (2.60) real, reflects the maximum free particle velocity that will yield a step of $\Delta\epsilon_0$ in energy. The x limits $x_{\rm min}$ and $x_{\rm max}$ occur at the points where the y limits are equal. Another factor of two appears because the y integral has been limited to the positive domain. For a minimum impact parameter of $\hat{\rho}_{\rm min} = m/\epsilon$, as chosen in the simulation, the integration region in Eq. (2.60) vanishes for energy steps larger than

$$\Delta\epsilon_{\rm max} = 1.25965\frac{\epsilon}{m^2}. \tag{2.61}$$

Beyond this value, $\omega(\Delta\epsilon_0, \hat{\omega}_\phi, \hat{\rho}_{\rm atm})$ is zero. Note that $\omega(\Delta\epsilon_0, \hat{\omega}_\phi, \hat{\rho}_{\rm atm})$ is even in $\Delta\epsilon_0$, implying a first moment $(\partial\epsilon/\partial\tau)$ equal to zero. The theory does not directly predict asymmetry between forward and backward energy transitions. It is this feature that necessitates use of the Einstein relation Eq. (2.13) in deriving $\partial\epsilon/\partial\tau$ due to long-range collisions.

To obtain the transition rate $w(\epsilon, \epsilon')$, we must average $\omega(\Delta\epsilon_0, \hat{\omega}_\phi, \hat{\rho}_{\rm atm})$ over the ϵ energy surface. Recall that the drift frequency $\hat{\omega}_\phi$ can be expressed as a function of the binding energy ϵ and the cylindrical separation in orbital units

$\check{\rho} = \epsilon\hat{\rho}_{\rm atm}$ in the following way:

$$\hat{\omega}_\phi = \chi\epsilon^3\mathcal{Q}(\check{\rho})\,.$$

The full form is given in Eq. (1.16). Only $\check{\rho}$ remains to average over.

$$w(\epsilon, \epsilon+\Delta\epsilon) = \int_0^1 P_\rho(\check{\rho})\,\omega\Big(\Delta\epsilon, \chi\epsilon^3\mathcal{Q}(\check{\rho})\,, \frac{\check{\rho}}{\epsilon}\Big)\,d\check{\rho} \tag{2.62}$$

Above, $P_\rho(\check{\rho})$ is the probability of finding a guiding-center atom chosen from an ergodic distribution in guiding-center phase space ($v_\perp = 0$) at cylindrical radius $\check{\rho}$ given by:

$$\begin{aligned} P_\rho(\check{\rho}) &= \check{\Omega}_c\check{\rho}\,P_{p_\phi}(\check{p}_\phi)\Big|_{\check{p}_\phi=\frac{1}{2}\check{\Omega}_c\check{\rho}^2} \\ &= \tfrac{16}{5\pi}\check{\rho}\int_0^{\check{z}_{\rm max}}\frac{(\check{\rho}^2+\check{z}^2)^{1/4}}{\sqrt{1-(\check{\rho}^2+\check{z}^2)^{1/2}}}d\check{z}. \end{aligned} \tag{2.63}$$

The probability $P_{p_\phi}(\check{p}_\phi)$ is given by Eq. (1.24).

Fig. 2.11 shows $w(\epsilon, \epsilon+\Delta\epsilon)$ obtained from the simulation and from the average above for $\epsilon = 10$. For the finite range of impact parameters in the simulation, $w(\epsilon, \epsilon')$ does not diverge at $\epsilon = \epsilon'$. Eq. (2.4) shows that the integral under $w(\epsilon, \epsilon')$ would diverge if the maximum considered impact parameter $\hat{\rho}_{\rm max}$ were placed at infinity. This divergence comes from the region near $\epsilon = \epsilon'$, where all collisions of very large impact parameter fall. The upper limit $x_{\rm max}$ in the integral in Eq. (2.60), arising from the simulation's finite impact area, cuts out this divergence and removes the sharp peak around $\Delta\epsilon = 0$. For collisions with impact parameter outside the region considered in the simulation ($\hat{\rho}_{\rm max} = 10/\epsilon$), Eq. (2.61) predicts a maximum energy step of 0.0126ϵ. Then the removed peak in Fig. 2.11, where $\epsilon = 10$, extends to $\Delta\epsilon \approx 0.13$. Note that the divergence seen in Figs. 2.1 and 2.2 comes

from the phenomenological fit function chosen and does not reflect the actual form of the large-impact-parameter divergence in $w(\epsilon, \epsilon')$.

Some material in this chapter is in preparation for publication. The dissertation author is the primary investigator and author of this material.

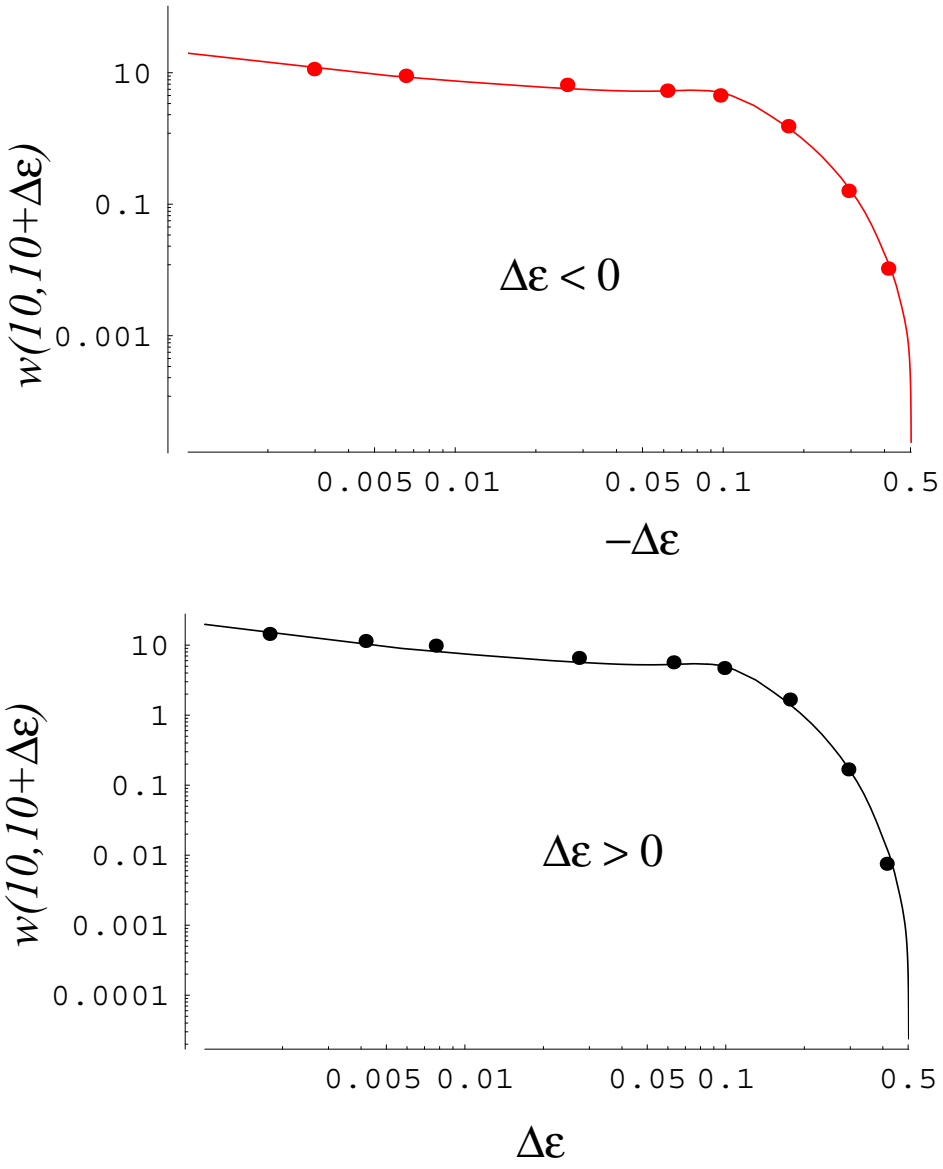

Figure 2.11: The transition probability rate density $w(10, \epsilon')$ for collisions with impact parameter larger than $\hat{\rho}_{\min} = 5/\epsilon$ at $\chi = 0.001$. The curves are theory from Eq. (2.60) averaged over all atom states at binding energy ϵ (with varying drift frequencies $\hat{\omega}_\phi$ and atom radii $\hat{\rho}_{\text{atm}}$). The points are derived from the simulation as in Fig. 2.1, except that only collisions with impact parameter greater than $\hat{\rho}_{\min} = 5/\epsilon$ are considered.

Chapter 3

Formation of Antihydrogen in a Thermal Plasma

In the previous chapter we developed the transition probability rate density $w(\epsilon, \epsilon')$ of an atom making a collisional transition from energy ϵ to energy ϵ'. We chose to track only atomic binding energy, anticipating that all other phase-space variables are populated ergodically. The orbital averages in Fig. 1.3 show that atoms fill an ergodic distribution appropriate for their binding energy to the extent allowed by angular momentum conservation. As they evolve into the chaotic regime, the distribution in observable variables shifts to the chaotic form, even though atoms are initially populated according to the guiding-center distribution. We are therefore justified in considering only evolution of the energy distribution $f(\epsilon)$.

Recall that the evolution of $f(\epsilon)$ is given by the master equation Eq. (2.3). This chapter develops a code for numerically solving this equation using the transition probability rate densities calculated previously. Once $w(\epsilon, \epsilon')$ has been established, this method allows us to rapidly predict the evolution of an arbitrary

distribution of atomic energies. By restricting ourselves to evolution in energy only, we may risk discarding important dynamics. However, good agreement is found between predictions made with our method and a much more time-consuming method which simply follows many atoms through collisional evolution. We use the code to calculate the rate of antihydrogen formation from antiprotons introduced into a thermal plasma.

3.1 Numerical Solution of the Master Equation

In solving the master equation Eq. (2.3), we use a discrete grid with a spacing of 0.1 in ϵ, with values in ϵ ranging from 0.1 to 100. The time integration is performed using an adaptive-time-step, fourth-order, explicit Runge-Kutta algorithm. The master equation integral was replaced by a sum over discrete grid points by way of the following procedure. The distribution function $f(\epsilon)$, defined on the grid points, was linearly interpolated between the points. The positive term in the master equation integral between two grid points becomes.

$$\begin{aligned}\int_{\epsilon'_i}^{\epsilon'_{i+1}} f(\epsilon')\, w(\epsilon', \epsilon_j)\, d\epsilon' &= f(\epsilon'_i) \int_{\epsilon'_i}^{\epsilon'_{i+1}} w(\epsilon', \epsilon_j)\, d\epsilon' \\ &\quad + \frac{f\left(\epsilon'_{i+1}\right) - f(\epsilon'_i)}{0.1} \int_{\epsilon'_i}^{\epsilon'_{i+1}} (\epsilon' - \epsilon'_i) w(\epsilon', \epsilon_j)\, d\epsilon'\end{aligned}$$

We calculate the two integral moments of $w(\epsilon', \epsilon)$ above for each (i, j) interval. The rate $w(\epsilon', \epsilon)$ itself is a third order interpolation between the discrete, smoothed values found in the last chapter by way of Eq. (2.8). The full integral for each value of j, excluding the two intervals around the singularity at $\epsilon = \epsilon'$, can then be

replaced by a sum over discrete grid points i, each point contributing two terms as above. The contribution from the central region is determined from Fokker-Planck theory by way of the transport coefficients $D_{\delta\epsilon}$ and $M_{\delta\epsilon}$, related by the Einstein relation Eq. (2.13) and found previously. The negative term in the master equation integral need only be determined for each ϵ_j value. The final equation to be solved by the Runge-Kutta code contains only sums (rather than integrals) with small discretization error.

To check the accuracy of this procedure, we followed an ensemble of $14,358$ atoms through 100 collision times, preserving atom variables between collisions, and compared the final result to the prediction of the master equation. Fig. 3.1 shows good agreement between the results for an initial Gaussian distribution. The master equation solution code was replicated for different values of $\Delta\epsilon_{\min}$ and $\Delta\epsilon_{\max}$ where the transition probability rate density was truncated. The best agreement is found in the case where the cutoffs in $w(\epsilon, \epsilon')$ are placed between the first empty bin and the largest observed transition (solid lines in Fig. 3.1). We therefore use these values in the final solution when determining the rate of antihydrogen formation. Expressions for the $\Delta\epsilon_{\min}$ and $\Delta\epsilon_{\max}$ used for different values of the magnetization parameter χ are found in the captions to Tables 2.1— 2.3.

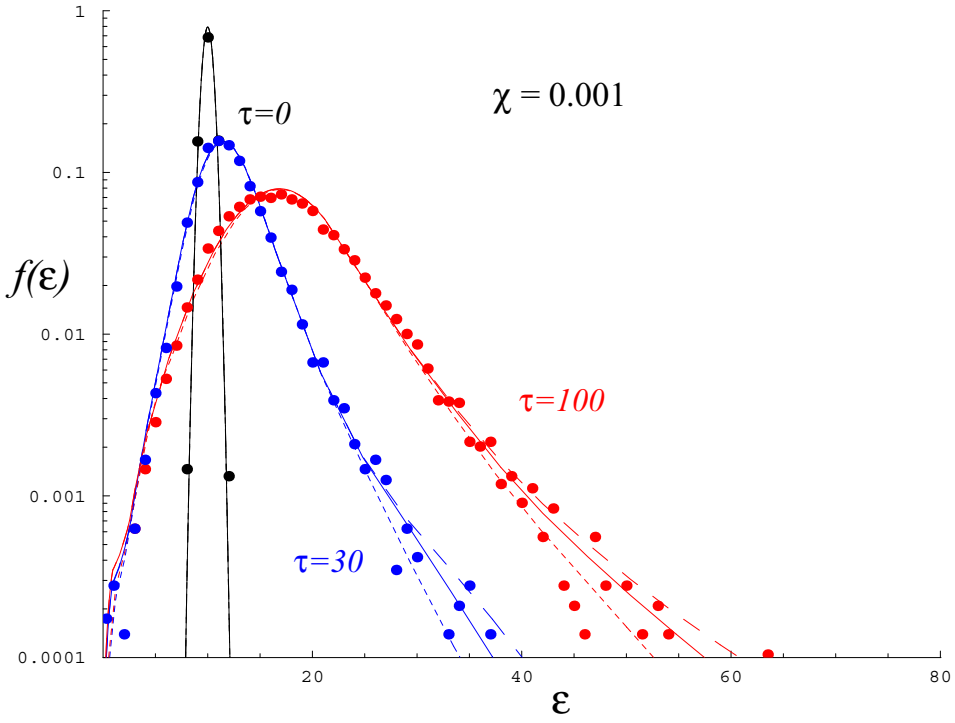

Figure 3.1: The evolution of a sample Gaussian distribution centered at $\epsilon = 10$ for $\chi = 0.001$. The black curve shows the initial distribution, blue is after 30 collision times, and red is after 100 collision times. The three curves show the solution for different choices of the cutoff $\Delta\epsilon$ in $w(\epsilon, \epsilon')$. It was chosen either at the largest observed transition (dashed), the first empty bin (dotted), or an average of the two (solid). The circles show the evolution of an ensemble of atoms that were chosen from the same initial distribution and followed through multiple collisions for the same amount of time. Best agreement is found for the solid line, so the the middle value of $\Delta\epsilon$ is used in the simulation.

3.2 Antihydrogen Formation from a Thermal Plasma

The frequency of close atom-positron collisions is proportional to the atomic cross sectional area

$$\nu_{\text{close}} = \frac{n\bar{v}b^2}{\epsilon^2}.$$

At shallow binding, the evolution time is very short and a thermal distribution is rapidly established. Like Glinsky and O'Neil [8], we assume a thermal distribution of atoms at small binding energies ϵ at the outset. Unlike previous work, however, we use the master equation Eq. (2.3) directly, with the transition probability rate density $w(\epsilon, \epsilon')$ derived from simulation. We set the initial distribution $f(\epsilon) = f_{\text{th}}(\epsilon)$ (from Eq. (2.6)) for $\epsilon < 1$ and hold it fixed in this region. Maximum atom size and available states diverge at $\epsilon = 0$. We truncate $f(\epsilon)$ at small ϵ by omitting the $\epsilon = 0$ grid point. For $\epsilon > 1$, $f(\epsilon)$ is initially zero and evolves according to the master equation. Above the maximum value of $\epsilon = 100$, the value of $f(\epsilon) = 0$, providing a sink at deep binding. Deeper binding states become populated as atoms "trickle in" from the fixed thermal region.

In this model, the antiproton is represented by a fixed electrostatic well into which positrons fall. The approximation is valid as long as the number of positrons predicted to fall into the well is much less than one. For sufficiently small nb^3, this criterion is always met. For finite nb^3, however, our code predicts that more than one positron will reach deep binding after a sufficiently long time. The model used

in deriving the thermal distribution of Eq. (2.6) is no longer valid at this point because the antiproton charge is shielded by a nearby positron. For experimentally relevant parameters, the number of recombined atoms per antiproton is small. The model only breaks down when very long times are considered. After such long times, the thermal bath at low ϵ from which new positrons trickle in no longer has the form of $f_{\rm th}(\epsilon)$. The charge neutralization of the atom depletes the reservoir outside the shielding cloud, cutting off the number of bound atoms that can form. We discard as non-physical any result that predicts a recombination fraction greater than unity.

Fig. 3.2 shows the distribution $f(\epsilon)$ around each antiproton for various numbers of collision times with the magnetic parameters $\chi = 0$ (infinite magnetic field), $\chi = 0.001$, and $\chi = 0.005$. In a typical recombination experiment, the antiproton transit time is approximately 1–10 collision times. As time passes, a steady-state (not thermal equilibrium) value of $f(\epsilon)$ is reached at progressively higher values of ϵ. In the steady-state region, the flux to deeper binding is independent of binding energy (divergence free). In thermal equilibrium, detailed balance means the net particle flux vanishes. Our steady-state exists indefinitely only because the $f(\epsilon) = 0$ boundary condition at $\epsilon = 100$ provides an infinite sink of particle flux. In a physical system, the steady state becomes established from small energies down to the ground state, then the thermal distribution is populated from the ground state upward. Inclusion of radiation changes the steady-state distribution at deep binding (see Chapter 4), but the thermal distribution still populates from

the ground state upward.

We can compare the simulated distribution $f(\epsilon)$ to the ionization energy spectrum observed by ATRAP as discussed in the Introduction. The observed ionization spectrum is equivalent to a roughly ϵ^{-5} dependence in $f(\epsilon)$ [14]. In the $\chi = 0.005$ case, where the magnetic field is weakest, a similar scaling is observed in the tail region, at binding energies deeper than that for which a steady-state distribution has been established. For smaller χ values, the cascade to deeper binding is more strongly suppressed and the tail drops off more steeply (see Fig. 3.2).

The steady-state flux to deeper binding caused by collisions must scale as the product of the collision frequency $\nu = n\bar{v}b^2$ and the number of thermal atoms available (Eq. (2.6)). The later is proportional to the small parameter nb^3. As previously predicted [7, 8, 9], this constant flux must be proportional to

$$(n\bar{v}b^2)(nb^3) \propto T^{-9/2}.$$

However, at deep binding the steady state takes many collision times to become established. Flux at binding energies ϵ above the maximum for which steady state has been established (for a given τ) does not have this simple temperature scaling. Fig. 3.3 shows the number of atoms that have reached binding energy ϵ, or lower, after 1, 10, 100, and 1000 collision times.

We now compare our simulation results to the observed antihydrogen formation rate in experiments. Unfortunately, a direct comparison requires knowledge of the antiproton transit time across the positron plasma, as well as the number

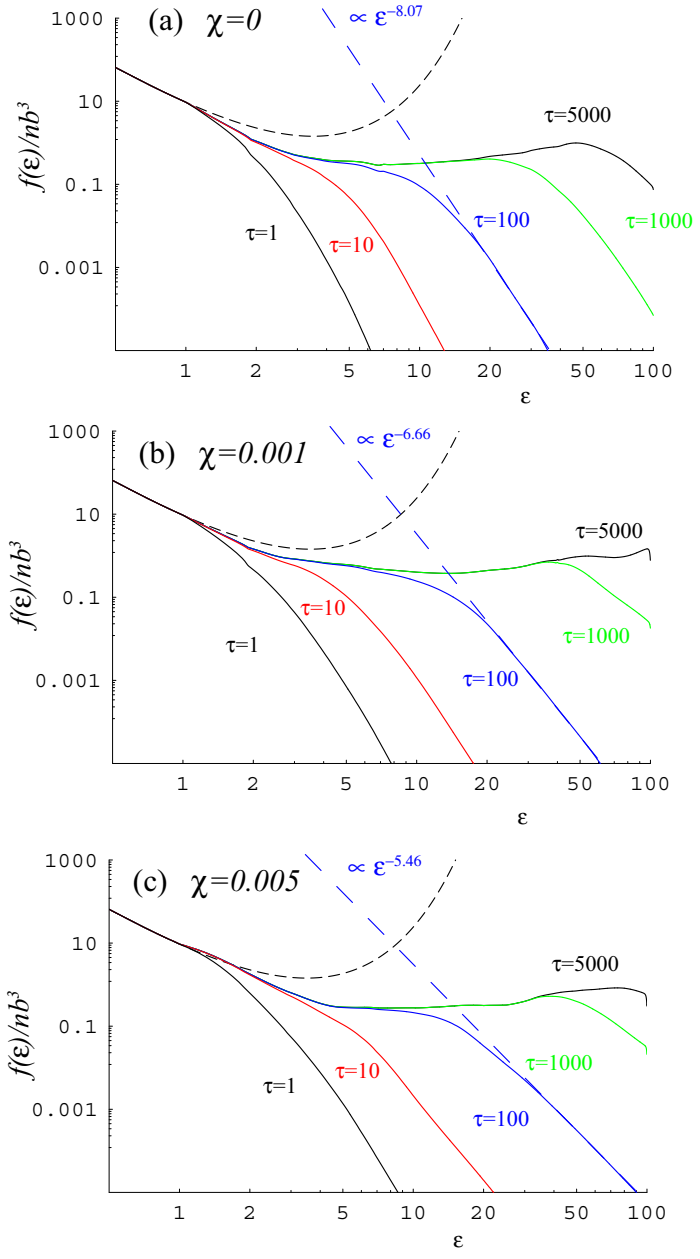

Figure 3.2: The distribution of positrons $f(\epsilon)$ around each antiproton for (a) $\chi = 0$, (b) $\chi = 0.001$, and (c) $\chi = 0.005$ at $\tau = tn\bar{v}b^2 = 1$, 10, 100, 1000, and 5000. At deeper binding, the steady-state distribution takes longer to establish. The chaotic cutoff energies $\epsilon_c = \infty$, 100, and 34.2 for $\chi = 0$, 0.001, and 0.005 respectively. The dashed curve indicates a thermal equilibrium distribution. The dashed, blue lines are power-law fits to the tail region at $\tau = 100$.

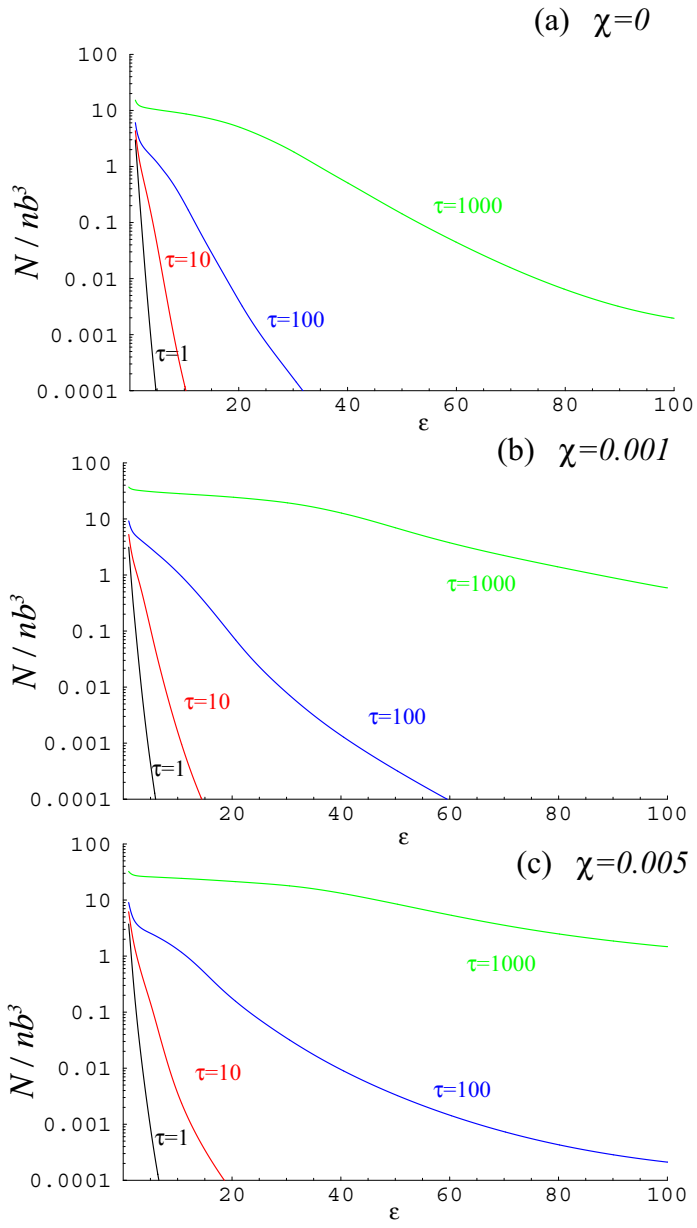

Figure 3.3: The fraction of atoms N, per antiproton, that have passed binding energy ϵ for (a) $\chi = 0$, (b) $\chi = 0.001$, and (c) $\chi = 0.005$ for different numbers of collision times $\tau = tn\bar{v}b^2$. Note that N is scaled to nb^3, with $nb^3 << 1$ assumed.

of transits each antiproton makes as the antiprotons are transferred many times between opposite sidewells. To our knowledge, this information is not provided in experimental papers, so we make estimates.

To survive a typical trap electric field of 25 V/cm, an atom must be bound by at least 1.9 meV. At a temperature of 4.2 K, as in the ATRAP apparatus [1], this threshold corresponds to $\epsilon = 5.3$. Fig. 3.3 shows that, assuming a transit time of 10 collision times, a single antiproton transit through the positron plasma has a chance of about $0.1nb^3$ of yielding an antihydrogen atom with a binding energy deeper than this level. For ATRAP, $nb^3 \approx 10^{-3}$. The observed formation rate of one antihydrogen per 75 antiprotons is consistent with these assumptions if antiprotons make 140 passes through the positron plasma during the experiment.

Similarly, for ATHENA parameters ($n = 2.5 \times 10^8$, $T = 15$ K) [3] $nb^3 \approx 3.5 \times 10{-}4$. The same binding energy threshold of 1.9 meV corresponds to $\epsilon = 1.5$. Each antiproton transit through the positron plasma is predicted to yield about $3nb^3 \approx 10^{-3}$ antihydrogen atoms deeply bound enough to be detected, again assuming a transit time of 10 collision times. The rough estimate of one anithydrogen formation event per 30 antiprotons in ATHENA is consistent with this result if each antiproton transits the plasma about 30 times during the experiment.

As seen in Fig. 3.3, these estimates change dramatically if we assume a different transit time. For instance, if the transit takes only one collision time, both estimates of the antihydrogen formation rate per transit are reduced by a factor of 10^{-2}. This would then require 100 times as many antiproton transits

through the positron cloud to explain the same rate of antihydrogen formation.

The number of atoms at or beyond the chaotic cutoff (much deeper than the ionization threshold discussed above) per antiproton transit for some experimentally relevant parameters is given in Table 3.1. We will see in the next chapter that radiation causes a small but significant fraction of atoms above the chaotic cutoff energy to relax to deep binding, giving an increase in the number of deeply bound atoms over the values shown in Table 3.1.

Fig. 3.4 shows the number of atoms below a fixed threshold energy $U = 6.89$ meV (near the chaotic cutoff for a 1 T field) for a constant relaxation time t and varying temperature. Neither the number of collision times τ nor the rescaled binding energy ϵ are constant in this case. The $T^{-9/2}$ temperature scaling is only seen for long relaxation times, when the steady state has had time to become established. In actual experiments, particles are trapped for much less than the time required for the steady state to reach deep binding. Note that for long-relaxation times and low temperature, the number of positrons deeper than the energy threshold is predicted to be greater than one. As discussed above, this prediction is non-physical.

At high temperatures, the fixed binding energy can indicate a more weakly bound atom than the kinetic bottleneck:

$$U < 4kT.$$

When atoms less deeply bound than this kinetic bottleneck are considered, the

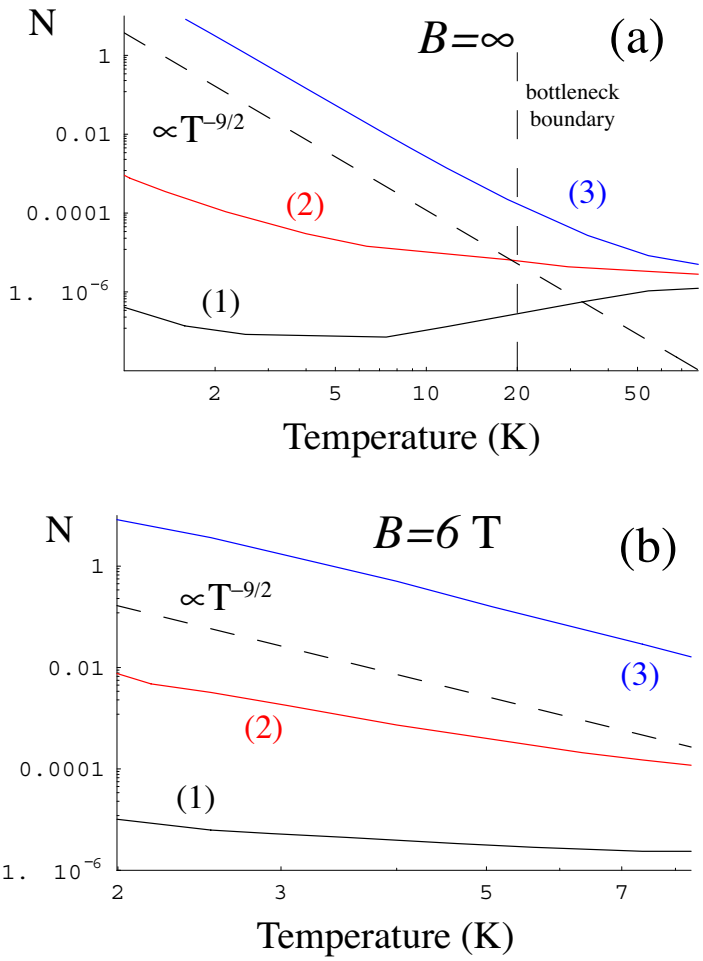

Figure 3.4: The fraction of atoms N, per antiproton, that have passed binding energy $U = 6.89$ meV ($\epsilon = 20$ at 4 K), given 1.84 μs (black curves, (1)), 7.36 μs (red curves, (2)), and 184. μs (blue curves, (3)). Density is fixed at 10^8 cm^{-3}. The times correspond to 25, 100, and 2500 collision times respectively, given this density and a plasma temperature of 4 K. In (a), the magnetic field is infinite, so $\chi = 0$ at all temperatures. In (b), $B = 6$T and χ ranges up to 0.005. The N shown is calculated from a linear interpolation between the discrete values of χ treated in the simulation. The result is non-physical when $N > 1$ (see text).

fraction of combined atoms depends much less strongly on the amount of time the antiproton spends in the trap. The convergence of the three curves in Fig. 3.4(a) means that, for small relaxation times, recombination fraction actually scales favorably with increasing temperature.

Below the chaotic cutoff energy ϵ_c, we will show that radiation becomes more significant, dominating the cascade process. Once an atom is in the chaotic orbit regime, we will see that it relaxes to deep binding on its own through radiation much more rapidly than in the guiding-center drift regime. Consequently, we consider an atom recombined once it has reached the chaotic regime.

Some material in this chapter is in preparation for publication. The dissertation author is the primary investigator and author of this material.

Table 3.1: The fraction of antiprotons yielding a chaotic atom in one transit time due to collisional recombination for some possible parameters and for three different transit times. The density is assumed to be 10^8 cm^{-3} in all cases.

magnetic field	temperature	χ	transit time	chaotic fraction
6 T	4 K	0.00177	1 μs	1.7×10^{-10}
			5 μs	4.5×10^{-7}
			10 μs	6.1×10^{-6}
	8 K	0.00500	1 μs	9.3×10^{-11}
			5 μs	7.8×10^{-8}
			10 μs	1.0×10^{-6}
4 T	6 K	0.00487	1 μs	1.8×10^{-9}
			5 μs	7.9×10^{-7}
			10 μs	1.9×10^{-5}

Chapter 4

Radiation

In this chapter we estimate the rate of atomic energy loss due to radiation. As in previous chapters, all calculations are done in the classical limit. Because the cyclotron action is fixed in the internal dynamics of guiding-center atoms, and the other time scales are slow, we anticipate that such atoms will have a slow radiation rate. With this in mind, radiation calculations in this chapter will assume atoms are ergodically populated according to the full Hamiltonian, not the restricted guiding-center Hamiltonian. While this distribution may be inappropriate for guiding-center drift atoms, significant radiation is expected to occur only at deeper binding, where chaotic dynamics begin to take over. As we saw in Chapter 1, an ergodic distribution over all phase space variables is most appropriate in this case.

We begin by calculating the Larmour power emitted by an atom at fixed energy U and angular momentum p_ϕ. The atomic orbit is assumed ergodic on the surface defined by these two fixed parameters. A phase-space average over this surface then stands in for a time average of the radiated power. We calculate the

torque from the radiative reaction force in the same way. The latter is shown to be insignificant compared to energy loss, meaning atoms drop to deeper binding until circular orbits are reached, then radiate slowly. If the initial angular momentum is sufficiently small, the circular orbit phase coincides with a rapid descent to deep binding and is unobservable.

From the energy-loss and torque rates we find the time to relax to the ground state as a function of initial energy and angular momentum p_ϕ, as well as magnetic field. We estimate the fraction of atoms, distributed in angular momentum ergodically, that will relax to the ground state after a fixed time. Suppression of radiative recombination in the guiding-center drift regime is demonstrated.

Finally, we combine our results with the numerically calculated distribution in binding energy $f(\epsilon, t)$ from Chapter 3 to estimate the number of atoms that will relax to the ground state by collisions and radiation for different antiproton transit times. This estimate assumes that the fraction of atoms decaying to the ground state via radiation is small. Collisional spreading of angular momentum (Stark Mixing) may elevate the fraction of atoms that reach the ground state by populating atoms in rapidly-radiating, low-angular-momentum orbits. A crude estimate of this effect predicts such an enhancement to be most significant when antiproton transit times are small.

4.1 Energy loss

To evaluate the rate of energy loss $\partial U/\partial t$ due to electromagnetic radiation, we use the classical Larmour formula [25].

$$\frac{\partial U}{\partial t} = \frac{2}{3}\frac{e^2}{c^3}\ddot{\vec{x}} \cdot \ddot{\vec{x}} \tag{4.1}$$

Here U is the unscaled binding energy with a minus sign introduced as in ϵ.

$$U = \frac{e^2}{(\rho^2 + z^2)^{1/2}} - \frac{1}{2m_e}\left(p_\rho^2 + p_z^2 + \left(\frac{p_\phi}{\rho} - \frac{1}{2}m_e\rho\Omega_c\right)^2\right) \tag{4.2}$$

We have switched to cylindrical coordinates, with ρ as the cylindrical radius and ϕ the azimuthal angle, so that we may express radiation rate in terms of the conserved p_ϕ as well as U. If the positron orbit is chaotic, the only constants of its motion are binding energy U and angular momentum p_ϕ. For an ergodic orbit, the time-average rate of change of ϵ is equivalent to a phase-space average of $\partial U/\partial t$ at fixed U and p_ϕ provided the radiation rate is sufficiently slow.

$$\frac{\dot{U}}{U}, \frac{\dot{p}_\phi}{p_\phi} << \frac{\dot{\alpha}}{\alpha} \tag{4.3}$$

Here, α is any phase space variable except for the conserved $p_{\phi 0}$. Even without the restriction in Eq. (4.3), the phase-space average of $\partial U/\partial t$ can be interpreted as the average energy-loss rate from a stochastic ensemble of atoms at a fixed energy and angular momentum.

The average Larmour power at angular momentum $p_{\phi 0}$ and binding energy U_0 is

$$\left\langle \frac{\partial U}{\partial t} \right\rangle = \frac{2}{3}\frac{e^2}{c^3}\frac{\int \delta(p_\phi - p_{\phi 0})\,\delta(U - U_0)\,\ddot{\vec{x}} \cdot \ddot{\vec{x}} d^3x d^3p}{\int \delta(p_\phi - p_{\phi 0})\,\delta(U - U_0)\,d^3x d^3p}. \tag{4.4}$$

The integral in ϕ is trivial. The integral in p_ϕ sets $p_\phi = p_{\phi 0}$. We will hereafter omit the subscript 0 in $p_{\phi 0}$ with this understanding. Let us switch to orbital (check) units defined in Eqs. (1.20). Recall that $\check{\Omega}_c$ in these units is related to χ and ϵ by

$$\check{\Omega}_c = (\chi \epsilon^{3/2})^{-1}.$$

The chaotic orbit condition of Eq. (1.18) becomes $\check{\Omega}_c \approx 1$. When $\check{\Omega}_c >> 1$, the atom is in the guiding-center drift orbit regime. When $\check{\Omega}_c << 1$, the orbit is Keplerian to first order.

In orbital units, Eq. (4.2) becomes

$$1 = \frac{1}{(\check{\rho}^2+\check{z}^2)^{1/2}} - \frac{1}{2}\left(\check{p}_\rho^2 + \check{p}_z^2 + \left(\frac{\check{p}_\phi}{\check{\rho}} - \frac{1}{2}\check{\rho}\check{\Omega}_c\right)^2\right) \equiv \check{U}. \tag{4.5}$$

Now we can re-write Eq. (4.4):

$$\left\langle \frac{\partial U}{\partial t} \right\rangle = \frac{2}{3}\left(\frac{U}{mc^2}\right)^3 \frac{U}{\mathcal{T}} \frac{\int \delta\left(\check{U}-1\right) \dddot{\check{\vec{x}}} \cdot \dddot{\check{\vec{x}}} d\check{\rho} d\check{p}_\rho d\check{z} d\check{p}_z}{\int \delta\left(\check{U}-1\right) d\check{\rho} d\check{p}_\rho d\check{z} d\check{p}_z}. \tag{4.6}$$

Above, $\mathcal{T}$ is the characteristic radiation time:

$$\mathcal{T} \equiv \frac{e^2}{mc^3}.$$

The Hamiltonian equations of motion provide $\ddot{\vec{x}}$. In dimensionless units

$$\begin{aligned} \dddot{\check{\vec{x}}} &= \left(-\tfrac{\check{\rho}}{(\check{\rho}^2+\check{z}^2)^{3/2}} + \check{\Omega}_c\left(\tfrac{\check{p}_\phi}{\check{\rho}} - \tfrac{1}{2}\check{\rho}\check{\Omega}_c\right)\right)\vec{a}_r \\ &\quad + \check{\Omega}_c \check{p}_\rho \vec{a}_\phi - \tfrac{\check{z}}{(\check{\rho}^2+\check{z}^2)^{3/2}}\vec{a}_z, \end{aligned} \tag{4.7}$$

where $\vec{a}_\alpha$ is the unit vector in the direction of coordinate α. Its dot product with itself is

$$\begin{aligned} \dddot{\check{\vec{x}}} \cdot \dddot{\check{\vec{x}}} &= \tfrac{1}{(\check{\rho}^2+\check{z}^2)^2} - \tfrac{2\check{\Omega}_c}{(\check{\rho}^2+\check{z}^2)^{3/2}}\left(\check{p}_\phi - \tfrac{1}{2}\check{\rho}^2\check{\Omega}_c\right) \\ &\quad + \check{\Omega}_c^2\left(\check{p}_\rho^2 + \left(\tfrac{\check{p}_\phi}{\check{\rho}} - \tfrac{1}{2}\check{\rho}\check{\Omega}_c\right)^2\right). \end{aligned} \tag{4.8}$$

Substituting Eq. (4.8) in Eq. (4.6), we can carry out the integral analytically in all but the cylindrical radius:

$$\begin{aligned}\left\langle \frac{\partial U}{\partial t} \right\rangle &= \frac{2}{3}\left(\frac{U}{mc^2}\right)^3 \frac{U}{\mathcal{T}} \frac{1}{\int_{\check{\rho}_{\min}}^{\check{\rho}_{\max}} \check{z}_{\max} d\check{\rho}} \int_{\check{\rho}_{\min}}^{\check{\rho}_{\max}} \left(\frac{\check{z}_{\max}}{2\check{\rho}^2(\check{\rho}^2+\check{z}_{\max}^2)} + \frac{\arctan(\check{z}_{\max}/\check{\rho})}{2\check{\rho}^3} - \right. \\ & 2\check{\Omega}_c \check{z}_{\max} \frac{\check{p}_\phi - \frac{1}{2}\check{\rho}^2\check{\Omega}_c}{\check{\rho}^2(\check{\rho}^2+\check{z}_{\max}^2)^{1/2}} + \check{z}_{\max}\check{\Omega}_c^2 \left(\frac{\check{p}_\phi}{\check{\rho}} - \frac{1}{2}\check{\rho}\check{\Omega}_c\right)^2 - \\ & \frac{\check{\Omega}_c^2}{2}\check{z}_{\max}\left(2 + \left(\frac{\check{p}_\phi}{\check{\rho}} - \frac{1}{2}\check{\rho}\check{\Omega}_c\right)^2\right) + \\ & \left.\frac{\check{\Omega}_c^2}{2}\left(\ln\left(\sqrt{\check{\rho}^2+\check{z}_{\max}^2}+\check{z}_{\max}\right) - \ln\left(\sqrt{\check{\rho}^2+\check{z}_{\max}^2}-\check{z}_{\max}\right)\right) d\check{\rho}.\right.\end{aligned} \tag{4.9}$$

Above,

$$\check{z}_{\max} = \sqrt{4\left(2 + \left(\frac{\check{p}_\phi}{\check{\rho}} - \frac{1}{2}\check{\rho}\check{\Omega}_c\right)^2\right)^{-2} - \check{\rho}^2}$$

is the maximum accessible value of $\check{z}$ at the given value of $\check{\rho}$. $\check{\rho}_{\min}$ and $\check{\rho}_{\max}$ occur where $\check{z}_{\max}$ vanishes, with $0 < \check{\rho}_{\min} < \check{\rho}_{\max} < 1$. The maximum and minimum possible angular momentum values $\check{p}_{\phi\max}$ and $\check{p}_{\phi\min}$ correspond to oppositely-oriented circular orbits in the $z = 0$ plane. For $\check{\Omega}_c = 0$, $\check{p}_{\phi\max} = -\check{p}_{\phi\min} = \frac{\sqrt{2}}{2}$.

In general, we must perform the integral in Eq. (4.9) numerically. However, a simplified expression is obtainable in the unmagnetized limit $\check{\Omega}_c = 0$. As rapid radiation comes from close passes to the origin, the magnetic field should have no significant impact on the energy-loss rate in the most strongly radiating regime. For the moment, let us leave the normalization factor $\int_{\check{\rho}_{\min}}^{\check{\rho}_{\max}} \check{z}_{\max} d\check{\rho}$ in its magnetic-field-dependent form but take the zero-field limit of the more complicated numerator. In the limit of small $\check{p}_\phi$, where orbits near the origin are allowed, the integral is dominated by small $\check{\rho}$. The above expression simplifies greatly to

$$\left\langle \frac{\partial U}{\partial t} \right\rangle \approx \frac{2}{3}\left(\frac{U}{mc^2}\right)^3 \frac{U}{\mathcal{T}} \frac{1}{\int_{\check{\rho}_{\min}}^{\check{\rho}_{\max}} \check{z}_{\max} d\check{\rho}} \frac{3\pi}{8} \check{p}_\phi^{-4}. \tag{4.10}$$

Taking the zero-field, small $\check{p}_\phi$ limit of the normalization factor

$$\int_{\check{\rho}_{\min}}^{\check{\rho}_{\max}} \check{z}_{\max} d\check{\rho}\Big|_{\check{\Omega}_c=0,\check{p}_\phi=0} = \int_0^1 \sqrt{1-\check{\rho}^2}\, d\check{\rho} = \frac{\pi}{4},$$

simplifies the expression for the energy-loss rate.

$$\left\langle \frac{\partial U}{\partial t} \right\rangle \approx \left(\frac{U}{mc^2}\right)^3 \frac{U}{\mathcal{T}} p_\phi^{-4} \tag{4.11}$$

At finite field, however, no simple analytic expression exists for the normalization factor. While the numerator is well approximated in the small $\check{p}_\phi$ region by the $\check{\Omega}_c = 0$ case, the normalizing denominator exhibits $\check{\Omega}_c$ dependence. This dependence is a reflection of available phase space. At small $\check{p}_\phi$ and $\check{\Omega}_c >> 1$, invariance of $\check{p}_\phi$ restricts orbits to small $\check{\rho}$. Zero-field ($\check{\Omega}_c = 0$) orbits are not similarly restricted. We must use the more general Eq. (4.10) to approximate the strong radiation region (small $\check{p}_\phi$) for finite magnetic field.

Fig. 4.1 shows the radiation rate of Eq. (4.9) plotted against $\check{p}_\phi$ at three values of $\check{\Omega}_c$ in a 1 Tesla magnetic field. Because orbits passing arbitrarily close to the origin are allowed for $p_\phi = 0$, the energy-loss rate diverges as p_ϕ^{-4} there. Low-angular-momentum states thus radiate to deeper binding more rapidly. In the guiding-center atom regime (high-$\check{\Omega}_c$), slowly-radiating, high-$\check{p}_\phi$ states constitute much more of available phase space than in the chaotic regime.

4.2 Torque

In addition to transporting energy away from the atom, radiation also carries away angular momentum. We will use an ergodic average identical to that

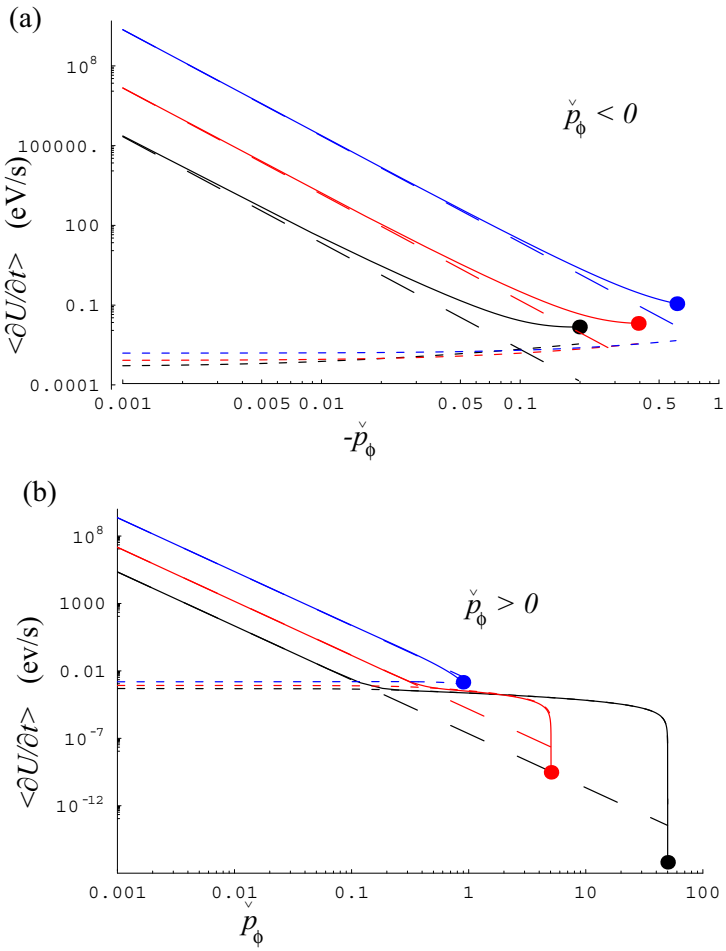

Figure 4.1: The radiation rate $\langle \partial U/\partial t \rangle$ from Eq. (4.9) (solid curves) plotted against $\check{p}_\phi$ for a magnetic field of 1 Tesla at three binding energies: $U = 0.332$ meV (black), 1.54 meV (red), 7.14 meV (blue), corresponding to $\check{\Omega}_c = 100, 10$, and 1 respectively. Separate log-log plots are shown for (a) $\check{p}_\phi < 0$ and (b) $\check{p}_\phi > 0$. The dashed lines, proportional to p_ϕ^{-4}, estimate the rate in the region of strong radiation from Eq. (4.10). The dotted lines plot the rate omitting the electric force from Eq. (4.7) and represent cyclotron radiation. For large $\check{\Omega}_c$, cyclotron radiation dominates for all but the lowest angular momenta. At the chaotic cutoff ($\check{\Omega}_c$=1), all available states radiate more rapidly than the cyclotron level. The dots at the end of the solid curves are for circular orbits in the $z = 0$ plane.

used in deriving the energy-loss rate of Eq. (4.9) to obtain an expression for the time rate of change of p_ϕ due to radiation. The instantaneous torque is given by

$$\frac{\partial p_\phi}{\partial t} = \vec{r} \times \vec{F}_{\rm rad} \cdot \vec{a}_z,$$

where $\vec{F}_{\rm rad}$ is the radiative reaction force.

$$\vec{F}_{\rm rad} = \frac{2}{3}\frac{e^2}{mc^3} m \dddot{\vec{x}}$$

Deriving Eq. (4.7) once in time and switching to dimensionless variables, the instantaneous radiative torque is

$$\frac{\partial p_\phi}{\partial t} = \frac{2}{3}\left(\frac{U}{mc^2}\right)^{3/2} U\check{\rho}\left(-\frac{\check{\rho}}{\left(\check{\rho}^2+\check{z}^2\right)^{3/2}}\dot{\check{\phi}} + \check{\Omega}_c\check{\rho}\dot{\check{\phi}}^2 - \check{\Omega}_c\dot{\check{p}}_\rho\right). \tag{4.12}$$

To express Eq. (4.12) in terms of coordinates and momenta only, we use the canonical definition of p_ϕ (Eq. (1.2)) along with the Hamiltonian relation

$$\dot{\check{p}}_\rho = \frac{\partial \check{U}}{\partial \check{\rho}}.$$

This gives the instantaneous torque in terms of phase variables $(\check{\rho}, \phi, \check{z}, \check{p}_\rho, \check{p}_\phi, \check{p}_z)$:

$$\frac{\partial p_\phi}{\partial t} = \frac{2}{3}\left(\frac{U}{mc^2}\right)^{3/2} U\left(\frac{\left(\frac{3}{2}\check{\rho}^2\check{\Omega}_c - \check{p}_\phi\right)}{\left(\check{\rho}^2+\check{z}^2\right)^{3/2}} + \check{\Omega}_c^2\left(\frac{1}{2}\check{\rho}^2\check{\Omega}_c - \check{p}_\phi\right)\right). \tag{4.13}$$

Once again presuming a stochastic orbit, we take a phase-space average over the distribution $\delta(U-U_0)\,\delta(p_\phi - p_{\phi 0})$ as in Eq. (4.4) to get the average rate of change of p_ϕ.

$$\begin{aligned}\left\langle\frac{\partial p_\phi}{\partial t}\right\rangle &= \frac{2}{3}\left(\frac{U}{mc^2}\right)^{3/2}\frac{U}{\int \check{z}_{\rm max} d\check{\rho}} \times \\ &\int\left(\left(\frac{3}{2}\check{\Omega}_c - \frac{\check{p}_\phi}{\check{\rho}^2}\right)\left(\frac{\check{z}_{\rm max}}{\sqrt{\check{\rho}^2+\check{z}_{\rm max}^2}}\right) + \check{z}_{\rm max}\check{\Omega}_c^2\left(\frac{1}{2}\check{\rho}^2\check{\Omega}_c - \check{p}_\phi\right)\right)d\check{\rho}\end{aligned} \tag{4.14}$$

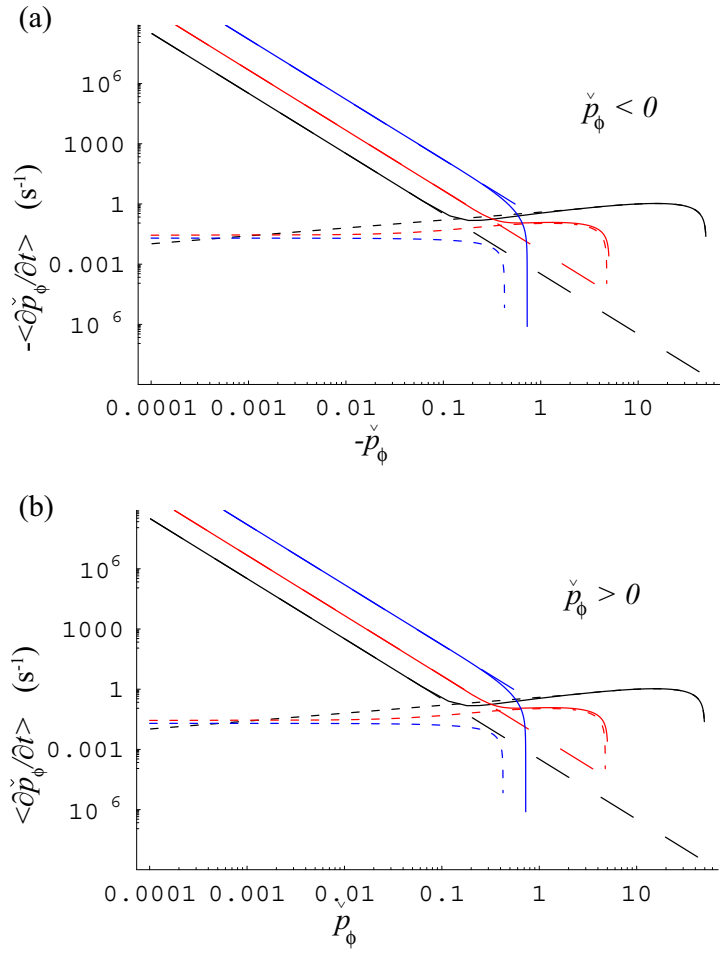

Figure 4.2: The average change in $\check{p}_\phi$ due to radiation $\langle\partial\check{p}_\phi/\partial t\rangle$ (from Eq. (4.14), solid curves) plotted against $\check{p}_\phi$ for a magnetic field of 1 Tesla at binding energies $U = 0.332$ meV (black), 1.54 meV (red), 7.14 meV (blue), corresponding to $\check{\Omega}_c = 100, 10$, and 1 respectively. To accommodate log-log plots, (a) $\check{p}_\phi < 0$, and (b) $\check{p}_\phi > 0$ appear on seperate plots, with the sign of the vertical axis switched in the first case. Because $\check{p}_\phi$ includes energy in its definition, its rate of change includes an energy change contribution as well as physical torque. The dashed lines, proportional to p_ϕ^{-3}, estimate the torque in the region of strong radiation ($|\check{p}_\phi| << 0$), given by the second term in Eq. (4.15) and dominated by energy change. The dotted lines plot the torque due only to accelerations produced by the magnetic force (i.e., due to cyclotron radiation). Near the extreme values of $\check{p}_\phi$, the plotted quantity becomes negative (not shown).

While Eq. (4.14) gives the physical torque, we need to consider energy-loss as well to find the rate of change of the rescaled $\check{p}_\phi$.

$$\left\langle \frac{\partial \check{p}_\phi}{\partial t} \right\rangle = \left\langle \frac{\partial}{\partial t} \frac{p_\phi}{e^2\sqrt{m_e/U}} \right\rangle = \frac{\langle \partial p_\phi/\partial t \rangle}{e^2\sqrt{m_e/U}} + \frac{1}{2}\check{p}_\phi \frac{\langle \partial U/\partial t \rangle}{U} \tag{4.15}$$

This quantity, plotted in Fig 4.2, has the same sign as $\check{p}_\phi$ for nearly the full range of $\check{p}_\phi$. Atoms thus evolve toward circular orbits in the $z = 0$ plane, where $|\check{p}_\phi|$ is maximal. At small values of $\check{p}_\phi$, the first term, proportional to $\check{p}_\phi^{-1}$, is dominated by the second term, proportional to $\check{p}_\phi^{-3}$ (from Eq. (4.10)). In this strong-radiation regime torque is negligible, but orbits evolve toward circles in the $z = 0$ plane as energy is radiated away.

4.3 Relaxation to the ground state

Fig. 4.3 shows two evolutions in U and $\check{p}_\phi$ predicted by Eqs. (4.9) and (4.14). For both low and high angular momentum states, the rate of radiative relaxation accelerates near the chaotic regime. At small $\check{\Omega}_c$, the magnetic field no longer restricts the positron to an $\vec{E} \times \vec{B}$ drift orbit and the energy-loss rate of Eq. (4.9) approaches its unmagnetized value, Eq. (4.11). This rate is proportional to U^4, evolving U to infinite energy in finite time. We will take the time at which this classical solution becomes singular as the relaxation time. Concurrently, the radiative torque of Eq. (4.14) pushes the atom toward a circular orbit. When the initial angular momentum is small in absolute value (indicating an eccentric orbit), the atom reaches deep binding before a circular orbit is established

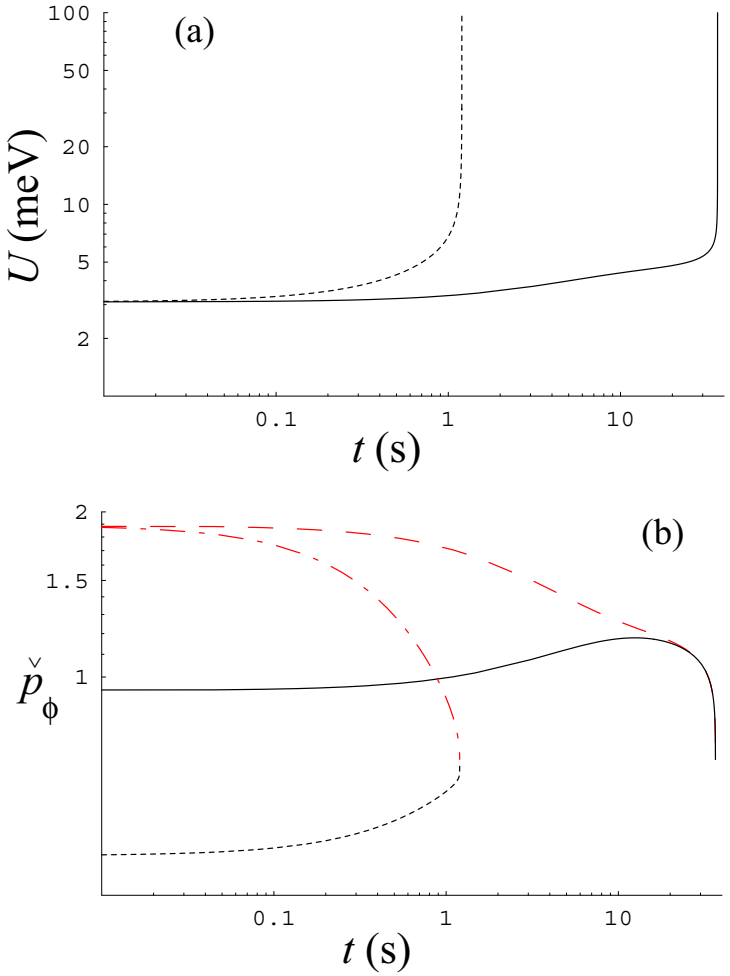

Figure 4.3: Evolution in (a) binding energy U and (b) rescaled angular momentum $\check{p}_\phi$ due to radiation for two atom initial conditions. The magnetic field is 1 Tesla, and both atoms begin at $U = 3.43$ meV ($\check{\Omega}_c = 3.5$). The atoms are begun with $\check{p}_\phi = 0.945$ (solid curves) and $\check{p}_\phi = 0.472$ (dotted curves). In (b), the red dash and dot-dash curves show the $\check{p}_\phi$ that give (positively oriented) circular orbits $\check{p}_{\phi\max}$ for the higher and lower initial p_ϕ atoms, respectively. The higher-p_ϕ atom radiates to a slowly-evolving, circular orbit before it reaches the chaotic cutoff energy (7.14 meV for a 1 Tesla magnetic field). The lower-p_ϕ atom stays in an eccentric orbit through its evolution past the chaotic cutoff.

Note that the zero-field, small-angular-momentum energy-loss rate of Eq. (4.11), combined with $\langle \partial \check{p}_\phi / \partial t \rangle$ in the same limit,

$$\langle \partial \check{p}_\phi / \partial t \rangle \approx \frac{1}{2} \left(\frac{U}{mc^2} \right)^3 \frac{1}{\mathcal{T}} \check{p}_\phi^{-3} \tag{4.16}$$

creates a system of differential equations in time with an analytic solution:

$$\begin{aligned} U(t) &= \frac{U_0 \check{p}_{\phi 0}^4}{\check{p}_{\phi 0}^4 - (U_0/mc^2)^3 (t/\mathcal{T})} \\ \check{p}_\phi(t) &= \check{p}_{\phi 0} \sqrt{\frac{U(t)}{U_0}} \end{aligned} . \tag{4.17}$$

Scaled angular momentum $\check{p}_\phi$ grows without bound in this simple approximation, but the relaxation time is still accurate for small initial $\check{p}_\phi$.

$$t_\mathrm{c} = \mathcal{T} \left(\frac{mc^2}{U_0} \right)^3 \check{p}_{\phi 0}^4 \tag{4.18}$$

By neglecting the magnetic field, we obtain a result that is even in $\check{p}_\phi$. While the estimate is most applicable to orbits with an initially small angular momentum, Eq. (4.18) provides useful scaling for the recombination time with initial energy and angular momentum even near the extreme values of $\check{p}_\phi$ (circular orbits). Fig. 4.4 shows the true recombination time found by simultaneously solving Eqs. 4.9 and 4.15 compared against the estimated t_c for two initial binding energies. For small $\check{p}_\phi$, the analytic approximation t_c works well. At larger angular momenta, the expression Eq. (4.10) underestimates the loss rate and the relaxation time is overestimated by t_c.

For a given relaxation time t_0 and binding energy U, there exist is a minimum $\check{p}_{\phi\mathrm{low}}$ and maximum $\check{p}_{\phi\mathrm{high}}$ value of $\check{p}_\phi$, between which atoms will have fallen

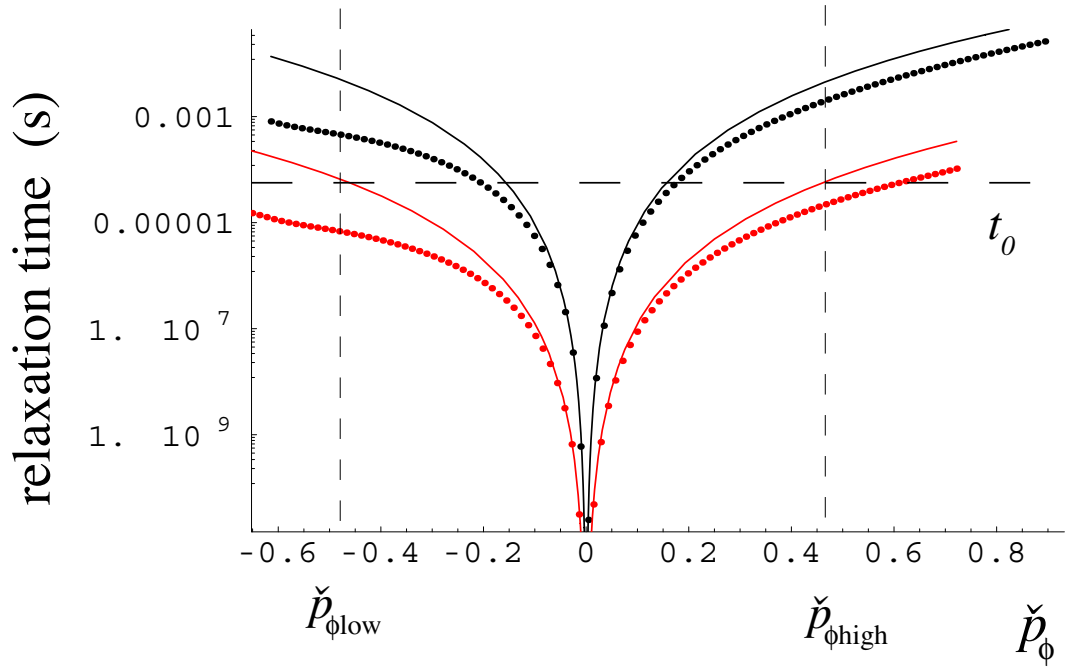

Figure 4.4: The time to radiatively relax to the ground state based on ergodic average expressions Eqs. (4.9) and (4.15) for the mutual evolution of energy U and rescaled angular momentum in the z direction $\check{p}_\phi$. The dots show when the solution becomes singular given the true evolution, while the lines show the small-$\check{p}_\phi$ approximation given by Eq. (4.18). Any given time t_0 defines a minimum and maximum $\check{p}_\phi$, defined for both the true and estimated evolutions, between which states will have relaxed to the ground state within t_0. A magnetic field of 6T is assumed. The initial energies shown are $U_0 = 0.0236$ eV (the chaotic cutoff; black) and $U_0 = 0.1$ eV (red). The estimate maximum and minimum $\check{p}_\phi$ (determined from t_c) are illustrated for the $U = 0.1$ eV case (see Eq. (4.19)).

to the ground state. The estimated recombination time given in Eq. (4.18) is even in $\check{p}_\phi$, so the minimum and maximum values of $\check{p}_\phi$ have the same absolute magnitude.

$$\check{p}_{\phi\text{high}} = -\check{p}_{\phi\text{low}} = \left(\frac{t_0}{\mathcal{T}}\left(\frac{U_0}{mc^2}\right)^3\right)^{1/4} \tag{4.19}$$

By integrating an ergodic distribution in $\check{p}_\phi$ from $\check{p}_{\phi\text{low}}$ to $\check{p}_{\phi\text{high}}$, we estimate the fraction of atoms that will radiatively relax after a given time. Fig. 4.5 shows the fraction combined after one collision time as a function of binding energy, given a 6 T magnetic field and a number density of 10^8 cm^{-3}. The theory curves illustrate that a magnetic field suppresses radiation below the unmagnetized rate at energies smaller than the chaotic cutoff.

For small binding energies, the combined fraction estimated in Fig. 4.5 is larger than the physical value. We have used the fully-ergodic distribution, appropriate for energies near and above the chaotic energy U_{chaotic}, at all energies. At small binding energy, the guiding-center distribution is more appropriate. The former is peaked at $p_\phi = 0$, while the latter is nearly uniform in p_ϕ (Fig. 1.4(a)). The fraction of weakly-bound atoms at very low p_ϕ is overestimated (by a factor of roughly 3) when the fully-ergodic distribution is used. Energy scaling is unaffected by the choice of distribution.

Now let us estimate the fraction of atoms that will relax to the ground state (due to radiation) from the collisional energy distributions previously determined. We will assume that the radiating fraction is small, so that the distribution function $f(\epsilon)$ is not perturbed from the collisional one calculated earlier.

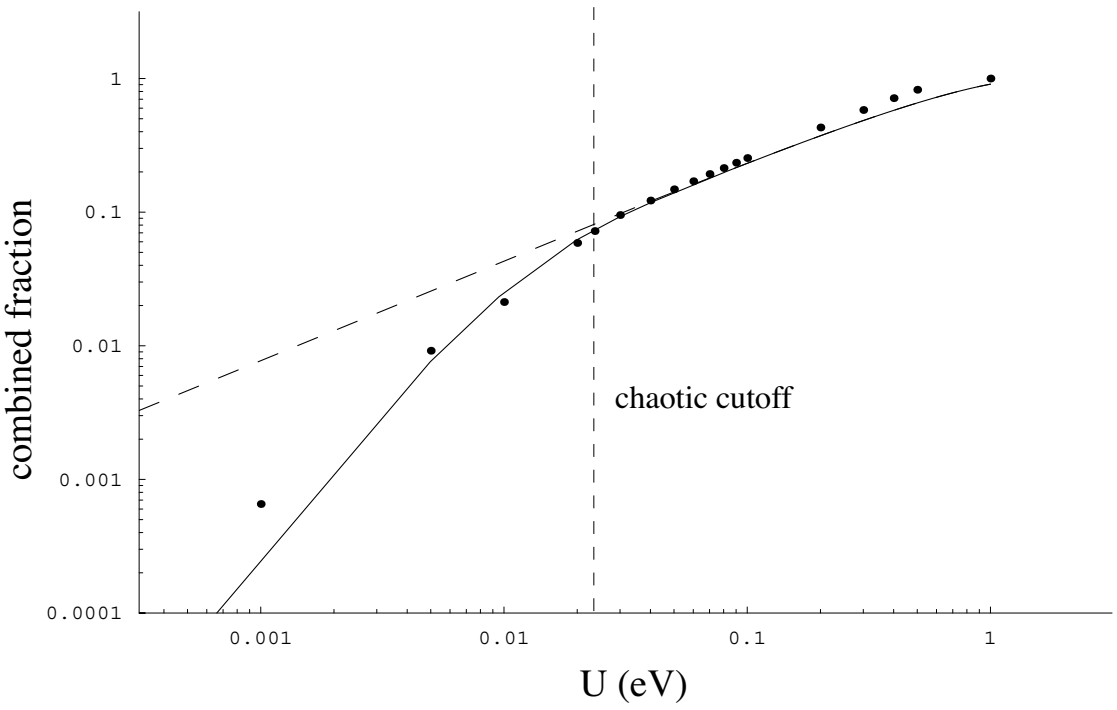

Figure 4.5: The fraction of particles that would relax to the ground state after one collision time (at 10^8 cm^{-3} and 4 K) as a function of energy. The dots come from simultaneous solutions of Eqs. (4.9) and (4.15), while the lines use the estimated relaxation time t_c from Eq. (4.18). The dots and solid line are for a magnetic field of 6 T. The dashed line is for the magnetic-field-free case. At energies smaller than the chaotic cutoff, the magnetic field reduces the recombined fraction below that for the unmagnetized case.

As radiation causes atoms with the lowest values of angular momentum $\check{p}_\phi$ to relax to the ground state, the ergodic distribution in angular momentum becomes depleted near $\check{p}_\phi = 0$. At any particular energy, this "hole" in phase space widens as more time passes and the maximum angular momentum $\check{p}_{\phi\max}$ for which atoms will have relaxed increases. The number of atoms in the depleted region constitutes an estimate of the fraction of atoms in the ground state.

Consider the collisionally-evolved distribution $f(\epsilon)$, calculated in the previous chapter, after some number of collision times τ. If this distribution is allowed to radiatively relax, as above, for a period of time Δt, some atoms at small angular momenta will fall to the ground state. We may ignore the simultaneous collisional evolution provided that we only consider short radiative relaxation times Δt compared to the total collisional evolution time $\tau/n\bar{v}b^2$. In this case, the number of atoms $N_{\rm GS}(t)$ radiatively relaxed to the ground state from a fixed distribution $f(\epsilon, t)$ after time Δt is

$$\begin{aligned} N(t) &= nb^3 \left(\int f(\epsilon,t) \int_{\check{p}_{\phi\min}(\epsilon,\Delta t)}^{\check{p}_{\phi\max}(\epsilon,\Delta t)} P_{p_\phi}(\epsilon,\check{p}_\phi)\, d\check{p}_\phi d\epsilon \right. \\ &\quad \left. + N_{100}(t) \int_{\check{p}_{\phi\min}(100,\Delta t)}^{\check{p}_{\phi\max}(100,\Delta t)} P_{p_\phi}(100,\check{p}_\phi)\, d\check{p}_\phi \right). \end{aligned} \tag{4.20}$$

The second term in the integral above accounts for atoms that have passed $\epsilon = 100$, the left boundary of the numerical solution of $f(\epsilon)$. N_{100} is the number of such atoms, all of which are assumed to lie at $\epsilon = 100$ for purposes of radiation rate. Since $\check{p}_{\phi\max}$ is proportional to $t^{1/4}$ (Eq. (4.19)), and the ergodic probability $P_{p_\phi}(\check{p}_\phi)$ of finding an atom with angular momentum $\check{p}_\phi$ is peaked around $\check{p}_\phi = 0$, a moderate change in relaxation time Δt has very little effect on the estimated number of atoms

N in the ground state. The black curves in Fig. 4.6 show this estimate for two different choices of the radiative relaxation time Δt. The density is 10^{-8} cm^{-3} for all curves. As expected, the choice of Δt has little effect on the predicted number of ground state atoms formed. A 1 meV antiproton takes 0.75 μs to traverse a 1 cm plasma. After this amount of time, approximately one in 200,000 antiproton transits would yield a ground state antihydrogen atom. If the antiproton remains exposed to the plasma for 10 μs, this fraction increases dramatically, to about one in 2000.

Above, we assumed that the collisionally-evolved distribution was perturbed very little by radiative depletion, so at each time t phase space was ergodically populated. In practice, the region around $p_\phi = 0$ becomes depleted and this small hole in the distribution persists until it is repopulated by collisional Stark mixing. A significant enhancement of the recombination rate may occur as the rapidly radiating hole is filled in by collisional processes. To estimate this effect, we consider the evolution of $f(\epsilon, t)$ as a series of successive, two-step periods of short time Δt. First, radiation depletes the region around $\check{p}_\phi = 0$ with a width given by Eq. (4.19). Then, the ergodic distribution is reestablished by collisions and the process repeats. In this case, the number of atoms $\mathcal{N}_{\rm GS}(\epsilon, t)$ that reach the ground state from energy ϵ after time t is

$$\mathcal{N}_{\rm GS}(\epsilon, t) = \sum_n \int_{\check{p}_{\phi\min}(\epsilon,\Delta t)}^{\check{p}_{\phi\max}(\epsilon,\Delta t)} P_{p_\phi}(\epsilon, \check{p}_\phi)\, d\check{p}_\phi n b^3 f(\epsilon, t_n) \quad ; \quad t = n\Delta t.$$

The time step Δt is the time required for angular momenta to mix collisionally,

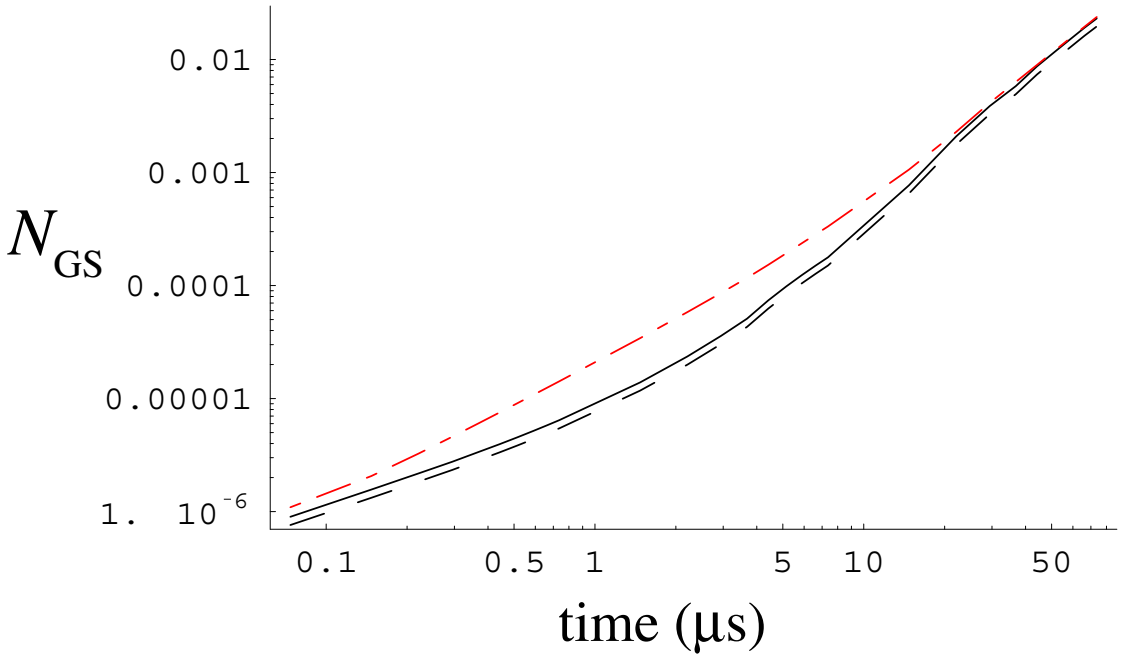

Figure 4.6: The number of atoms $N_{\rm GS}$ that are estimated to reach the ground state per antiproton transit through the plasma as a function of the transit time (Eq. (4.20)). The estimate in the black curves is made by allowing the collisionally-evolved distribution after time t given by $f(\epsilon, t)$ to relax radiatively for a time $\Delta t << t$. The magnetic field is 6 T, the temperature is 4 K, and the density is 10^8 cm^{-3} for all curves. The solid curve is for $\Delta t = 0.1t$ and the dashed curve is for $\Delta t = 0.05t$. The red curve shows an estimate if the low-angular-momentum region is continually repopulated by collisional Stark mixing. This effect produces an enhancement for small times, but not at large times, when most radiative relaxation is happening in deeply bound atoms with long Stark mixing times.

reestablishing the ergodic distribution. The estimate depends sensitively on the choice of Δt. A reasonable choice for this Stark mixing time is the inverse of the frequency of small-impact-parameter collisions at energy ϵ.

$$\Delta t = \frac{\epsilon^2}{n\bar{v}b^2} \tag{4.21}$$

This time is much longer for small atoms at deep binding than it is for weakly bound, larger atoms. If Δt is small compared to the evolutionary time scale for $f(\epsilon, t)$, we may rewrite $\mathcal{N}_{\rm GS}$ in the following way:

$$\mathcal{N}_{\rm GS}(\epsilon, t) = \frac{nb^3}{\Delta t} \int_{\check{p}_{\phi\min}(\epsilon,\Delta t)}^{\check{p}_{\phi\max}(\epsilon,\Delta t)} P_{p_\phi}(\epsilon, \check{p}_\phi)\, d\check{p}_\phi \int_0^t f(\epsilon, t')\, dt'.$$

For deep binding, Δt grows large and can exceed the total evolution time t. To account for this, we must take the smaller of t or Δt in the denominator of the prefactor above. With this consideration, the total number of atoms in the ground state is given by the integral over ϵ. Switching the time integration variable from t' to $\tau = t' n\bar{v}b^2$ and using the estimate for Δt from Eq. (4.21), the number $N_{\rm GS}(t)$ is

$$\begin{aligned} N_{\rm GS}(t) \;=\; & nb^3 \left(\int \frac{1}{\mathrm{Min}(\epsilon^2, tn\bar{v}b^2)} \int_{\check{p}_{\phi\min}(\epsilon,\Delta t)}^{\check{p}_{\phi\max}(\epsilon,\Delta t)} P_{p_\phi}(\epsilon, \check{p}_\phi)\, d\check{p}_\phi \int_0^{tn\bar{v}b^2} f(\epsilon, \tau)\, d\tau d\epsilon \right. \\ & \left. + \frac{1}{tn\bar{v}b^2} \int_{\check{p}_{\phi\min}(100,\Delta t)}^{\check{p}_{\phi\max}(100,\Delta t)} P_{p_\phi}(100, \check{p}_\phi)\, d\check{p}_\phi \int_0^{tn\bar{v}b^2} N_{100}(\tau)\, d\tau \right). \end{aligned} \tag{4.22}$$

As before, all atoms that have cascaded deeper than $\epsilon = 100$ are considered to be at this energy.

The Stark mixing estimate is the dot-dashed, red curve in Fig. 4.6. The effect enhances the fraction of atoms that reach the ground state when antiproton

transit time is small. For long transit times, deep binding is reached through collisional de-excitation and radiation overtakes collisional phase-space spreading as the fastest time scale. For deeply bound atoms, the radiatively depopulated hole around $\check{p}_\phi = 0$ now encompasses a large fraction of available phase space. Most such atoms relax quickly to the ground state, so the hole is only filled in when atoms cascade from more shallow binding. At this point, the two estimates of N_{GS} converge.

At early times, most atoms are in the guiding-enter energy range. The small fraction of such atoms that rapidly radiate dominates the estimate shown in Fig. 4.6. As atom-positron collisions populate energies near the chaotic cutoff (around 5 μs in the figure), the rate of formation of ground-state atoms increases. As discussed in the previous chapter, the results cannot be trusted once the recombined fraction nears one. In this case, the thermal reservoir at shallow binding is depleted by charge shielding and the antihydrogen formation rate must taper off.

Our radiation estimate has negligible impact on the observed rate of antihydrogen formation in either ATRAP or ATHENA. A transit time of 10 collision times for the optimistic parameters given in Fig. 4.6 corresponds to 0.7 ms. For this transit time, the predicted number of observed atoms (i.e., those surviving the electric fields of the trap) is about 100 times greater than the number predicted to be in the ground state. Nevertheless, this estimate suggests that ground state atoms have been made in the two experiments.

Some material in this chapter is in preparation for publication. The disser-

tation author is the primary investigator and author of this material.

Bibliography

[1] Gerry Gabrielse. Atoms made entirely of antimatter: Two methods to produce slow antihydrogen. *Advances in Atomic, Molecular, and Optical Physics*, 50:155, 2005.

[2] Clifford M. Surko. Positron plasma in the laboratory. *Physical Review Letters*, 62(8):901–904, 1988.

[3] M. Amoretti et al. Production and detection of cold antihydrogen atoms. *Nature*, 419:456–459, 2002.

[4] Gerry Gabrielse et al. Background-free observation of cold antihydrogen with field-ionization analysis of its states. *Physical Review Letters*, 89(21):213401, 2002.

[5] Francis Robicheaux. Simulations of antihydrogen formation. *Physical Review A*, 70:022510, 2004.

[6] D. Vrinceanu. A theoretical survey of formation of antihydrogen atoms in a penning trap. In *Atomic Processes in Plasmas — 15th International Conference on Atomic Processes in Plasmas*, 2007.

[7] Peter Mansbach and James Keck. Monte carlo trajectory calculations of atomic excitation and ionization by thermal electrons. *Physical Review*, 181(1):275–289, 1969.

[8] Michael E. Glinsky and Thomas M. O'Neil. Guiding center atoms: Three-body recombination in a strongly magnetized plasma. *Physics of Fluids B*, 3(5):1279–1293, 1991.

[9] Francis Robicheaux and James D. Hanson. Three-body recombination for protons moving in a strong magnetic field. *Physical Review A*, 69(1):010701, 2004.

[10] Yukap Hahn. Plasma density effects on the three-body recombination rate coefficients. *Physics Letters A*, 231:82–88, 1997.

[11] Eric M. Bass and Daniel H. E. Dubin. Energy loss rate for guiding-center anithydrogen atoms. *Physics of Plasmas*, 11(3):1240–1243, 2004.

[12] Stanislov G. Kuzmin, Thomas M. O'Neil, and Michael E. Glinsky. Guiding center drift atoms. *Physics of Plasmas*, 11(5):2382–2393, 2004.

[13] Hirohiko Kono, Takayuki Tazaki, Isao Kawata, and Yuichi Fujimura. Magnetic field effects on the dynamics of a Ryberg electron: The residence time near the core. *Journal of Chemical Physics*, 111(24):10895–10902, 1999.

[14] T. Pohl, H. R. Sadeghpour, and Gerry Gabrielse. New interpretations of measured antihydrogen velocities and field ionization spectra. *Physical Review Letters*, 97(14):143401, 2006.

[15] Francis Robicheaux. Three-body recombination for electrons in a strong magentic field: Magnetic moment. *Physical Review A*, 73(3):033401, 2006.

[16] G. Andresen et al. Antimatter plasmas in a multipole trap for antihydrogen. *Physical Review Letters*, 98(2):023402, 2007.

[17] C. Fred Driscoll. Comment on "Driven production of cold antihydrogen and the first measured distribution of antihydrogen states". *Physical Review Letters*, 92(14):149303, 2004.

[18] R. S. Fletcher, X. L. Zhang, and S. L. Rolston. Using three-body recombination to extract electron temperatures of ultracold plasmas. *Physical Review Letters*, 99(14):145001, 2007.

[19] T. C. Killian, M. J. Lim, S. Kulin, R. Dumke, S. D. Bergeson, and S. L. Rolston. Formation of rydberg atoms in an expanding ultracold neutral plasma. *Physical Review Letters*, 86(17):3759–3762, 2001.

[20] S. X. Hu. Three-body recombination of atomic ions with slow electrons. *Physical Review Letters*, 98(13):133201, 2007.

[21] Türker Topçu and Francis Robicheaux. Radiative cascade of highly excited hydrogen atoms in strong magnetic fields. *Physical Review A*, 73(4):043405, 2006.

[22] Herbert Goldstein. *Classical Mechanics*. Addison-Wesley Publishing Company, 1980.

[23] A. Osterwalder, R. Seiler, and F. Merkt. Measurement of the hyperfine structure in low-l, high-n Rydberg states of ortho H_2 by millimeter wave spectroscopy. *Journal of Chemical Physics*, 113(18):7939–7944, 2000.

[24] Klaus Siglow and Hans J urgen Neusser. Photo- versus pulsed field-ionization of individual high n ($n \lesssim 57$) Rydberg states: Resolved d, g series of benzene. *Journal of Chemical Physics*, 112(2):647–653, 2000.

[25] John David Jackson. *Classical Electrodynamics*. John Wiley & Sons, Inc., 1999.

[26] Michael E. Glinsky, Thomas M. O'Neil, and Marshall N. Rosenbluth. Collisional equipartition rate for a magnetized pure electron plasma. *Physics of Fluids B*, 4(5):1156–1166, 1992.

[27] George B. Arfken and Hans J. Weber. *Mathematical Methods for Physicists*. Academic Press, 1995.

[28] D. R. Bates, A. E. Kingston, and R. W. P. McWhirter. Recombination between electrons and atomic ions i. optically thin plasmas. *Proceedings of the Royal Society of London. Series A, Mathematical and Physical Sciences*, 267:297–312, 1962.

[29] William H. Press, Brian P. Flannery, Saul A. Teukolsky, and William T. Vetterling. *Numerical Recipes: The art of Scientific Computing*. Cambridge University Press, 1986.

[30] Eric M. Bass and Daniel H. E. Dubin. Relaxation of antihydrogen from rydberg to ground state. In *Non-Neutral Plasma Physics VI, Workshop on Non-Neutral Plasmas*, pages 147–152, 2006.